IMMUNE AND MOLECULAR CORRELATES OF RESPONSE TO IMMUNOTHERAPY REVEALED BY BRAIN-METASTATIC MELANOMA MODELS.

Amélie Daugherty-Lopès[1], Eva Pérez-Guijarro[2,7,8], Vishaka Gopalan[3,8], Jessica Rappaport[1], Quanyi Chen[1,5], April Huang[1,5], Khiem C. Lam[1], Sung Chin[4], Jessica Ebersole[4], Emily Wu[2], Gabriel A. Needle[2], Isabella Church[2], George Kyriakopoulos[1,2], Shaojun Xie[6], Yongmei Zhao[6], Charli Gruen[2], Antonella Sassano[2], Romina E. Araya[1], Andres Thorkelsson[2], Cari Smith[4], Maxwell P. Lee[2], Sridhar Hannenhalli[3], Chi-Ping Day[2,3], Glenn Merlino[2], and Romina S. Goldszmid[1,9*]

[1]Inflammatory Cell Dynamics Section, Laboratory of Integrative Cancer Immunology, Center for Cancer Research, National Cancer Institute, NIH, Bethesda, MD 20892, USA

[2]Laboratory of Cancer Biology and Genetics, Center for Cancer Research, National Cancer Institute, NIH, Bethesda, MD 20892, USA

[3]Cancer Data Science Laboratory, Center for Cancer Research, National Cancer Institute, NIH, Bethesda, MD 20892, USA

[4]Leidos Biomedical Research Inc., Frederick National Laboratory for Cancer Research, National Cancer Institute, Frederick, MD 21701, USA

[5]Kelly Government Solutions, Bethesda, MD, USA

[6]CCR-SF Bioinformatics Team, Bioinformatics and Computational Science Directorate, Frederick National Laboratory for Cancer Research, NIH, Frederick, MD 21701, USA

[7]Present address: Institute for Biomedical Research Sols-Morreale (IIBM), Spanish National Research Council-Universidad Autónoma de Madrid (IIBM, CSIC-UAM), Madrid, Spain.

[8]These authors contributed equally

[9]Lead contact

[*]Correspondence: rgoldszmid@mail.nih.gov

SUMMARY

Despite the promising results of immune checkpoint blockade (ICB) therapy, outcomes for patients with brain metastasis (BrM) remain poor. Identifying resistance mechanisms has been hindered by limited access to patient samples and relevant preclinical models. Here, we developed two mouse melanoma BrM models that recapitulate the disparate responses to ICB seen in patients. We demonstrate that these models capture the cellular and molecular complexity of human disease and reveal key factors shaping the tumor microenvironment and influencing ICB response. BR1-responsive tumor cells express inflammatory programs that polarize microglia into reactive states, eliciting robust T cell recruitment. In contrast, BR3-resistant melanoma cells are enriched in

neurological programs and exploit tolerance mechanisms to maintain microglia homeostasis and limit T cell infiltration. In humans, BR1 and BR3 expression signatures correlate positively or negatively with T cell infiltration and BrM patient outcomes, respectively. Our study provides clinically relevant models and uncovers mechanistic insights into BrM ICB responses, offering potential biomarkers and therapeutic targets to improve therapy efficacy.

INTRODUCTION

Cancer treatment has seen substantial improvement in the last decade. However, therapeutic options for patients with brain metastasis (BrM) are still limited and frequently ineffective, leading to a dismal prognosis[1,2]. Immune checkpoint blockade (ICB) has shown promising results in clinical trials, however, only a limited subset of patients respond to this approach[3–7]. While ICB combination or in association with radiotherapy, in particular stereotactic radiation therapy, can enhance efficacy, the use of steroids – often prescribed to BrM patients to reduced inflammation – has proven to be detrimental for ICB response[6]. Therefore, there is an urgent need to identify optimal combinations and regimens to improve patient outcomes. Moreover, we still lack a clear understanding of the specific tumor microenvironment (TME) responses in BrMs that could lead to the identification of biomarkers strongly correlating with the clinical benefit of ICB.

The brain tumor microenvironment (BrTME) is unique, containing highly specialized resident cell types including microglia that constitute the main immune population, and non-immune cells, such as neurons, astrocytes, and oligodendrocytes[8–10]. These are combined with specific extracellular matrix (ECM) networks and neurotransmitters[8–10], all of which are essential for maintaining brain homeostasis. The BrTME is also controlled in part by the blood-brain barrier (BBB), which regulates the access and distribution of infiltrating immune cells, tumor cells, and drugs, to the brain[8–12]. Previous reports have shown clear differences in immune composition and tumor molecular profiles between BrMs, extracranial metastases, and primary tumors in patients[13–16]. This raises the question of whether determinants and mechanisms of ICB responses at extracranial sites also apply to BrM. Recent studies have expanded our knowledge regarding the diversity of the BrTME, demonstrating that heterogeneity in immune composition within the BrTME among patients is mainly driven by tumor cells themselves, rather than the uniqueness of the brain environment[17–22]. These studies showed that the largest discrepancies among BrM subtypes were in the T cell and myeloid compartments[17–22]. Nevertheless, how tumor cells regulate the BrTME and its impact on ICB responses remain to be elucidated.

Important limitations of these retrospective studies include the relatively small cohorts, the diverse treatments patients received, and the rare availability of biopsies from ICB responder patients. Additionally, the constraints of sample collection result in heterogeneous representation of the stroma in BrM biopsies, including an under-representation of microglia. Modeling BrM in mice is challenging. Some models rely on intracranial injection of tumor cells, bypassing extravasation and disrupting the BBB, thereby inducing local inflammation[23,24]. A few orthotopic BrM models, including autochthonous ones, recapitulate the full metastatic cascade[23–26], though they are not without

limitations such as low penetrance and/or long latencies[23,24]. Other models utilize systemic inoculation of tumor cells (e.g., intracarotid or intracardiac), recreating the cascade steps needed for brain colonization while maintaining BBB integrity[23,24]. However, these approaches also have drawbacks, including the need for invasive surgery (intracarotid inoculation) and the earlier development of extracranial lesions. The latter can hinder the comparative analyses of BrM-specific ICB-responders and non-responders, thus preventing the identification of predictive biomarkers of response and the discovery of new therapeutic targets.

The aim of this study was to address this unmet need and interrogate the immune and molecular determinants of ICB response in melanoma BrMs. To achieve this, we developed two syngeneic brain-metastatic models M4-BR1 (hereafter BR1) and M4-BR3 (BR3) derived from our previously established M4-B2905 (M4) melanoma mouse cell line[27]; both models exhibit the highest incidence of metastases and larger lesions in the brain, with BR1 being virtually brain-specific. We demonstrate that these models represent the molecular and cellular complexity and diversity of ICB responses observed in patients. Through comparative studies, we identify specific tumor molecular signatures associated with immune BrTME composition, ICB responses, and patient outcomes. Therefore, this study provides a robust framework for the necessary mechanistic studies to optimize BrM therapy.

RESULTS

Development of metastatic melanoma models with high brain penetrance.

To study BrM therapeutic response to ICB, we generated a panel of syngeneic immunocompetent preclinical models preserving BBB integrity by intracardiac (i.c.) injection of the M4 melanoma mouse cell line[27] into syngeneic C57BL/6 mice. We have previously demonstrated that M4, generated by neonatal UV-irradiation of hepatocyte growth factor transgenic mice (Hgf^{Tg}), faithfully recapitulates the etiology, histopathology, and molecular features of human cutaneous melanoma[27]. After recovering metastatic cells from the brain, we cycled them *in vivo* to enhance their brain-metastatic potential (see Methods) (Figure S1A). We obtained two polyclonal sublines, BR1 and BR3, that exhibit high penetrance to the brain and form numerous pigmented macroscopic metastases in up to 100% of injected animals on average per experiment (Figure 1A-B). We confirmed the presence of melanoma cells in the brains of mice from both models by dopachrome tautomerase (DCT)[28,29] immunostaining at day 18-20 post-implantation (model endpoint) (Figure S1B). To assess metastatic burden while preserving tissue integrity, we developed a machine learning approach that semi-automatically detects, counts, and measures the area of metastatic foci on whole-brain stereomicroscope images[30]. Following optimization (see Methods), we achieved a comparable number of BrMs per mouse between BR1 and

BR3 (Figure 1C). However, BR3 formed more extracranial metastases and displayed a lower BrM/extracranial metastases ratio compared to BR1, indicating different metastatic tropism between the two models (Figures 1C, S1C-D). Nevertheless, in both BR1 and BR3, the highest incidence of metastases and larger lesions were observed in the brain, allowing for sufficient time to study BrMs without overwhelming extracranial disease (Figures S1C-D). Thus, we successfully developed two immunocompetent BrM models with high brain penetrance while maintaining a physiological BBB, providing a valuable platform for comparative and mechanistic studies of BrM therapeutic responses.

BR1 and BR3 models exhibit mutational landscapes representative of human BrM melanomas.

To confirm that our models are translationally relevant, we interrogated their molecular resemblance with human disease. We characterized the mutational landscape of cultured BR1 and BR3 cell lines in comparison to the M4 parental line using whole exome sequencing analysis. We found more mutated genes in the brain-metastatic lines compared with the parental M4 cells (432, 403, and 327 genes in BR1, BR3 and M4 parental, respectively; Figure S1E). Not surprisingly, 90% and 86% of the genes mutated in the M4 parental line were also detected in BR1 and BR3, respectively. However, each of the brain-metastatic models contained approximately 30% unique mutated genes (Figure S1E; Table S1), potentially contributing to their distinct metastatic behavior *in vivo*. Mutations related to PTEN or PI3K/AKT pathways were present across the M4 parental line, BR1, and BR3, although the specific mutated genes varied between these models (Table S1). We next explored the mutational landscape in metastatic patients using the publicly available MSK-MET-SKCM cohort[31] and the cBioportal platform[32–34]. We found that most of the mutated genes identified in our models that are related with these pathways were also frequently mutated in melanoma patients with BrMs (Figure S1F). In line with our observation, while no specific mutations unique to melanoma BrM have been identified so far, $AKT1^{E17K}$ increases BrM incidence in mice, and patients with mutations in the PI3K/AKT pathway (e.g., PTEN) have a higher risk of developing central nervous system (CNS) metastases[26,35,36]. Overall, these results show that our models display molecular alterations associated with BrM development in human melanoma.

BR1 and BR3 BrMs recapitulate the diversity of responses to ICB observed in the clinic.

To evaluate the ICB therapeutic response of the models, we treated syngeneic mice that were i.c.-injected with either BR1 or BR3 using anti-CTLA-4 or anti-PD-L1 monotherapies, or combination therapy (combo, anti-CTLA-4 + anti-PD-L1), dual isotype or vehicle controls. We started dosing at day 3 or 4 with each antibody, after verifying metastatic brain seeding on day 4 through microscopy and *ex vivo* culture of cells from the implanted brains (Figures S1G-H). When control groups reached

the endpoint, we assessed BrM burden using our machine-learning algorithm[30]. We observed striking response differences between the two models (Figures 1D-G). We found a significant reduction in total metastatic foci count and area in BR1 following treatment with both mono- and combo-therapies (Figures 1D-E). Combo therapy was the most effective regimen, also reducing the size of individual metastases (Figures 1D-E). In addition, we observed significantly fewer extracranial metastases in this model, which disappeared in half of the monotherapy-treated and >90% of the combo-treated animals (Figure S1I). In marked contrast, BR3 BrMs were resistant to ICB, showing no changes in the total BrM foci count, metastatic area, or individual lesion size in any therapeutic group (Figures 1F-G). We observed a modest decrease in total extracranial metastasis counts in BR3-bearing animals treated with ICB monotherapies, and a significant response with combo therapy (Figure S1J). These results align with clinical studies indicating that extracranial and BrM responses to ICB do not always correlate with each other[3].

Even at a more advanced metastatic stage (7 days after i.c. injection), the BR1 model remained significantly responsive to combo therapy and displayed a modest response to monotherapies (Figures S1K-L). Overall, our models recapitulate the diversity of clinical responses observed in melanoma BrM patients[3–5].

ICB-sensitive and resistant models display distinct BrTME and remodeling upon treatment.

To identify potential immune correlates of BrM ICB responses, we performed multiparametric spectral flow cytometry on brain leukocytes from both combo-treated, which yielded the strongest response, and untreated BR1 and BR3 models. Consistent with their ICB responsiveness, we observed a significantly higher number of total leukocytes in BR1 compared to BR3, independent of their treatment status (Figure 2A). To gain more granularity, we performed unsupervised clustering of immune cells followed by supervised cell annotation (Figures 2B, S2A-B; Table S2). Uniform Manifold Approximation and Projection (UMAP) visualization and Principal Component Analysis (PCA) using the frequency of the identified leukocyte populations revealed different BrTME compositions between the two models in both treated and untreated groups (Figures 2C-E).

To determine the specific immune populations driving the differences between untreated BR1 and BR3, we analyzed the PC1 loadings, which segregate these two groups (Figures 2D and S2C-D). These loadings revealed that BR1 samples had a higher frequency of various infiltrating cells, including T cells, DCs, natural killer (NK) cells, and inflammatory monocytes (Ly6C^{hi}), which are known to favor ICB responses[37–39] (Figures 2E and S2D-F). The absolute number of these cells was also higher in BR1 compared to BR3 (Figures 2F-H and S2G). This indicates a stronger immune cell recruitment in

untreated BR1 BrMs compared to untreated BR3. In contrast, BR3 samples had a higher frequency of neutrophils, microglia, and Ly6C^{lo} monocytes (Figures 2E and S2D). Both the proportion of microglia (>90% of total leukocytes) and the infiltrating cell populations in the BR3 ICB-resistant BrTME resembled that of non-tumor-bearing brains (PBS) (Figures 2E and S2H).

We observed a significant therapy-induced increase of total leukocytes along with an enrichment of T cells in BR1 and a trend toward an increase of infiltrating T cells in BR3 (Figures 2A, 2E-H, S2E-F). This aligns with recently published clinical studies showing ICB-driven increase T cell infiltration[21,40,41]. Nevertheless, TME dissimilarities between BR1 and BR3 were still observed after combo therapy, as evidenced by their segregation along PC2 (Figures 2D, S2D and S2I). BR1 continued to display higher frequency and number of infiltrating cells compared to BR3, which after combo therapy was specifically due to a surge in CD8$^+$ T cells (Figures 2E-H, S2F-G). Additionally, a higher number of microglia was observed in treated BR1 compared to treated BR3 (Figure 2F). Altogether, these observations indicate BrTME immune compositional differences between ICB-sensitive and -resistant BrMs, with some differences, such as those in T cells and microglia, persisting after therapy.

A distinct T cell landscape is associated with ICB response.

The quantity and characteristics of infiltrating T cells play an important role in the response to ICB[42–45]. Therefore, we studied the specific T cell characteristics associated with ICB-responses in our BrM models by performing single-cell RNA sequencing (scRNAseq) of whole brains from PBS and untreated BR1 and BR3 samples (Figures S3A-B). Differential gene expression analysis of total CD8$^+$ T cells between ICB-sensitive BR1 and resistant BR3 revealed higher expression of activation/effector function-associated genes (*Nkg7*, *Pdcd1*, *Ifng*, *Gzmb*) in BR1, whereas the BR3 CD8$^+$ T cell pool displayed a naïve signature (*Sell*, *Lef1*, *Tcf7*, *Foxp1*) (Figure 3A; Table S3). UMAP projection and unsupervised clustering of the T cells revealed six CD8$^+$ T cell clusters (CD8.sc1-6) and six CD4$^+$ T cell clusters (CD4.sc1-6) with different abundance between the two models (Figures 3B-C, S3C). Clusters CD8.sc1 and CD4.sc1, defined by a naïve gene signature, were enriched in PBS and BR3 samples, accounting for over 60% of their total CD8$^+$ and CD4$^+$ T cell populations, whereas they made up only 5-20% of T cells in BR1 (Figures 3B-D, S3C-E; Tables S3-S4). Projection of our T cell clusters onto a single-cell reference atlas for T cell states[42] confirmed that CD8.sc1 and CD4.sc1 correspond to the naïve compartments (Figures 3E, S3F). BR3 also presented a higher proportion of cluster CD8.sc3, which mapped mostly onto CD8$^+$ effector memory T cells on the reference atlas (Figures 3B-E, S3D; Table S3).

In contrast, BR1 was characterized by a higher diversity of T cells, including various $CD8^+$ and $CD4^+$ T cell subsets expressing different levels of genes encoding T cell degranulation/lysosomal activity (*Lamp1*, *Ctsl, Cd63;* CD8.sc2), activation/dysfunction (*Cd81*, *Ckb*, *Nr3c1;* CD8.sc2)[46,47], regulatory function (*Foxp3, Il2ra, Ikzf2;* CD4.sc5-6), and immune checkpoint receptors previously described as activation and/or exhaustion markers (*Lag3*, *Pdcd1*, *Havcr2;* CD8.sc4-6 and CD4.sc3-4)[42,45,46] (Figures 3B-E, S3C-E; Tables S3-S4). Among the latter, CD8.sc5, the most enriched cluster in BR1, displayed the highest level of genes encoding cytotoxic molecules (e.g., *Ifng*, *Prf1*, *Gzmb*) (Figures 3B-D, S3D; Table S3). Similarly, the BR1-enriched CD4-sc3 exhibited the highest expression of *Ifng* and *Tbx21* (T-bet), consistent with a Th1-like signature (Figures S3C, S3E; Table S4). Notably, CD8.sc4, exclusively found in the BR1 BrTME, expressed the transcription factor TCF-1 (*Tcf-7*), the nuclear protein TOX (Tox), and low levels of genes encoding cytotoxic cytokines and immune checkpoint receptors (except *Havcr2*) (Figures 3B-E; Table S3). This expression profile resembles that of the so-called "exhausted stem cell-like CD8 T cells", previously identified as essential for ICB response and associated with better clinical outcomes in melanoma patients[43,45]. Finally, the BR1 enriched clusters CD8.sc6 and CD4.sc6 displayed a proliferative profile (*Mki67*, *Cdk1*, *Ccnb2*), suggesting that local expansion contributes to the higher T cell number observed in this model (Figures 3B-D, S3C-E; Tables S3-S4). We confirmed these T cell compositional differences between untreated BR1 and BR3 BrTME by spectral flow cytometry and showed higher number of activated T cells in BR1 (Figures 3F-J, S3G-I).

To determine if the T cell compositional differences between the two models are sustained after treatment, we analyzed the BrTME of combo-treated BR1 and BR3 (Figures 3F-J, S3G-I). BR1 showed a specific 20-fold increase in CD8.F5 and a 10-fold increase in CD8.F4, both subsets marked by activation (Figures 3H-J). Interestingly, CD8.F5 resembles tissue-resident memory T cells (T_{RM}), which have been associated with better ICB efficacy and improved patient outcomes for non-brain tumors[48–50] (Figure 3I). In addition, combo therapy in BR1 led to a significant increase in the $CD4^+$ T cell subset CD4.F5 displaying activation/exhaustion markers (Figures S3H-I). On the other hand, most $CD8^+$ and $CD4^+$ T cell subsets slightly increased in BR3 after therapy (Figures 3J, S3I). Together, these results demonstrate that the quantity and the quality of the T cells differed between the ICB-responder and resistant BrM models, highlighting the importance of the intrinsic BrTME T cell landscape in ICB response and aligning with immune correlates of response described for tumors at extracranial sites[43–45].

Unique reactive microglia signatures are found in ICB-responder BrMs.

Microglia, the predominant immune cell type in the CNS, are crucial in regulating brain homeostasis, response to tissue injury, and pathogens[51–53]. While different studies have suggested their dual role in BrM development[10,54–56], their contribution to ICB response is unclear. As expected, microglia represented 80-95% of the immune BrTME in both of our models (Figures 2E, S2E). We then inquired whether different microglia transcriptional states might be associated with BrM response to ICB. To do so, we extracted microglia from our whole-brain scRNA-seq dataset (Figure S3B) and performed differential gene expression and Gene Set Enrichment Analysis (GSEA). Compared to BR3, BR1 microglia upregulated genes and pathways associated with MHC class I and II antigen presentation (MHC-I/-II) (*H2-Aa*, *Cd74*, *B2m*), response to type I and II interferons (IFN-I/ -II) (*Ifitm3*, *Ifi27l2a*, *Cxcl10*), and inflammatory proteins including T cell-attracting chemokines (*Cxcl10*, *Cxcl16*, *Cxcl9*) (Figures 4A-B), indicating a reactive microglia transcriptional signature. Similar pathways were enriched in BR1 compared to PBS (Figure S4A). Conversely, BR3 microglia showed enrichment of homeostatic genes and pathways such as neuronal development and synaptic remodeling[51–53], displaying a transcriptional profile similar to PBS (Figures 4A-B, S4B). TNFα signaling via NF-κB was enriched in BR3, but not BR1, microglia compared to PBS (Figure S4A).

Microglia are heterogeneous, particularly in disease conditions[51–53]. To investigate microglia heterogeneity in our BrM models, we performed unsupervised clustering and identified thirteen different microglia clusters (Figures 4C-D). Clusters Mg1-4 and Mg8, characterized by the highest level of homeostatic microglia genes and pathways (e.g., phagocytosis, regulation of cellular response to TGFβ, and neuronal function), represented the predominant microglia states in BR3 and PBS (Figures 4C-E, S4C). Clusters Mg5-6, also highly abundant in these groups, were enriched in pathways related to ribosomal and mitochondrial function, indicating a transcriptionally active state (Figures 4C-E). In contrast, the overall reactive signature of BR1 microglia was driven by the combination of five different clusters, Mg9-Mg13, defined by reduced expression of homeostatic genes and pathways (Mg9-11 and Mg13), upregulation of IFN response genes (Mg12-13), antigen presentation (Mg9, Mg12-13), and pathways involved in T cell recruitment and regulation of adaptive immune responses (Mg12-13) (Figures 4C-E, S4C). These clusters constituted 70-80% of the total BR1 microglia, while representing less than 15% of BR3 and minimally present in PBS (Figure 4D). Clusters Mg11 and Mg13, nearly absent in BR3 and PBS, expressed mitotic and proliferative genes (Figures 4C-E, S4C), possibly explaining the higher number of microglia found in BR1 (Figure 2F). Using high-parametric spectral flow cytometry, we confirmed the higher proportion and total number of microglia with various reactive states in BR1 (Mg.D-E) as compared to BR3 (Figures 4F-J, S4D). Taken together, our

data suggest that reactive microglia, characterized by high expression of MHC-I/II and T cell-attracting chemokines, are associated with response to ICB, while resistant BrMs maintain homeostatic microglia states.

Systemic ICB alters microglia functional state.

It is unclear whether systemic ICB treatment can impact microglia states. To address this question, we assessed the combo-treated BR1 and BR3 microglia phenotype using spectral flow cytometry. Surprisingly, therapy led to the disappearance of almost all homeostatic microglia states in both models (Mg.A-Mg.C; Figures 4F-J, S4D). Instead, they were replaced by various non-homeostatic states characterized by the absence of P2RY12 expression (Mg.F-Mg.J; Figures 4F-J, S4D), the loss of which has been previously linked with neuroinflammation[52,57]. While the decrease of P2RY12 was a common therapy-induced feature, some phenotypic differences were still observed between BR1 and BR3 (Figures 4G-I, S4D). BR1 microglia maintained the expression of MHC-II, while reducing markers associated with macrophage pro-tumorigenic function such as ARG1, SIRPα[58–61] and the T cell inhibitory receptors PD-L1, TIM3 and LAG3[62–64] (clusters Mg.F-G; Figures 4G). In contrast, the microglia state increased in BR3, but not in BR1, after therapy (Mg.J) expressed the highest levels of TIM3, LAG3, and SIRPα (Figures 4G, 4I-J, S4D). We cannot rule out that the low levels of PD-L1 detected after combo treatment stem from a masking effect of anti-PD-L1 antibody. Combined, these results indicate that systemic ICB therapy alters microglia functional states. The key differences between microglia in ICB-responder and non-responder BrMs, regardless of treatment status, lie in the expression of genes, pathways, and proteins that can modulate T cell activities.

BR1 and BR3 exhibit distinct tumor cell-intrinsic molecular programs that correlate with those present in human BrMs.

We next sought to identify tumor cell-intrinsic molecular features that may be driving the distinct BrTME observed in our models. To do so, we compared BR1 and BR3 melanoma cell transcriptomes from our whole brain scRNA-seq data set. Model-based analysis of single-cell transcriptomics (MAST)[65,66] followed by GSEA revealed that overall BR1 cells were enriched in MHC-I/II antigen presentation (e.g., *H2-K1/D1, B2m, Tap1, H2-Aa/Ab1/Eb1, Cd74,*), immune response and IFN signaling (e.g., *Ifng, Irf1, Stat1, Ifi203, Cxcl9*), cell cycle, and DNA replication and repair (e.g., *Mki67, Aurka/b, Plk1, Top2a, Pdgfa, Chek1*) (Figures 5A, S5A). On the other hand, BR3 cells expressed higher levels of genes and pathways related to melanin biosynthesis (e.g., *Tyr, Dct, Slc45a2*), neuronal function (e.g., *Sema3a, Unc5c, Slc6a11, Pde1c/3a/4b, Cacna1d, Selenop*), and metabolic pathways

such as glutathione transferase activity (e.g., *Gsta4, Gstm1*), oxidative phosphorylation (OXPHOS, e.g., *Atp6v0d2, Cox7a1*), and lipid metabolism (e.g., *Apoe*) (Figures 5A, S5A).

To determine the key molecular programs (referred to as metaprograms [MPs]) that characterize our models and compare them with available clinical data, we applied a Non-negative Matrix Factorization (NMF)[67] approach (Figure S5B; see Methods). NMF-based methods are able to identify gene expression patterns that highlight differences within tumors, as well as variation between different tumors[68–70]. A similar approach has been successfully used in BrM patients to discover tumor MPs[13]. We identified seven different MPs (MP1-MP7) and characterized them using Metascape pathway analysis[71] (Figure 5B; Table S5). Melanoma cells within BR1 tumors were enriched in MPs associated with cell cycle and DNA damage response pathways (MP1), tissue development and morphogenesis (MP3), immune response and antigen presentation (MP4), and translation and mitochondrial metabolism (MP5) (Figure 5C). Melanoma cells in BR3 tumors displayed higher activity of MPs related to melanin biosynthesis (MP2 and MP7) and neuron development and axon guidance (MP6) (Figure 5C). To validate that our mouse BrM MPs are representative of human disease, we computed correlations between these mouse MPs and human MPs from three melanoma patient cohorts[13,40,72] (Figure 5D-E; see Methods). Each mouse MP identified in our study correlated with one or more patient BrM MPs involved in similar functions from at least one cohort (Figure 5D). We verified that the correlations found between pairs of human- and mouse-MPs were consistent across all melanoma BrM human datasets[13,40,72] (Figure 5E). We did not observe significant correlations between mouse MPs and human MPs exclusively expressed in extracranial metastases (i.e., human-MP4)[13] (Figure 5D).

Given that the BR1 and BR3 cell lines are polyclonal, we investigated whether the transcriptional signatures distinguishing these two models were broadly expressed across all cells within each model or specific to certain cell subpopulations. We performed unsupervised clustering of tumor cells based on their expression of MPs, identifying 5 clusters (T1-T5) with distinct MP activity that were differentially distributed between the two models (Figures 5F-I, S5C). The main differences between BR1 and BR3 were the higher proportion of T2 in BR1, which displayed the highest activity for MP1, MP4 and, MP5, whereas BR3 had higher frequency of T3, T4, and T5, expressing MP2, MP3, MP6, and MP7 (Figures 5G-I). Analysis of MP activity on a per-cell basis revealed that in some cases, MP expression varied between groups even within the same cluster, for example, MP6 was expressed at a higher level in BR3 cells in clusters 3, 4, and 5 (Figure 5I). These results suggest that the difference between BR1 and BR3 tumor cells and their overall MP expression can be attributed to variation in cluster abundance, the specific MP activity within these clusters, and their activity at the per-cell level.

In summary, we identified molecular programs distinguishing ICB-responder and ICB-resistant BrM models that may contribute to their distinct BrTME and therapy responses. Furthermore, we demonstrated that these MPs are also present in human melanoma BrMs, highlighting the translational relevance of our models.

BR1 and BR3 tumor cell-intrinsic features shape the microglia functional states that drive T cell phenotypes.

Cell-cell interactions are essential to shape the TME and drive antitumor immunity. Based on the distinct BR1 and BR3 BrTME and cell-intrinsic programs, we hypothesized that tumor cells skew microglia functional state and downstream interaction with T cells. To test this, we performed pairwise interactome analysis of tumor cell – microglia – T cells in our scRNAseq dataset to infer ligand-receptor (L-R) pairs implicated in their crosstalk (Figures 6A-C; S6A-B). We observed the highest predicted interaction number and strength coming from tumor cells to microglia in both models, with no significant differences in the number of interactions between BR1 and BR3 (Figures 6A, S6A). This crosstalk occurred among distinct microglia and tumor states and involved different types of interactions in BR1 compared to BR3 (Figures 6B-C). Key differences involved enhanced communication in BR1 from the tumor cell cluster enriched in immune and cell-cycle-MPs (T2) to reactive microglia states (Mg9, Mg12-13), including upregulation of the microglia-activating MIF_CD74_CD44 axis[73–75] (Figures 6B-C). In BR1, we also observed enrichment of the LGALS9 axis, known to induce MHC-II expression on macrophages and DCs and strong anti-tumor responses in murine melanoma models[76,77]. BR3, on the other hand, showed stronger interactions than BR1 between tumor clusters displaying melanin-, development-, and neuro-MP activities (T3-T5) and homeostatic microglia (Mg1-2, Mg4, and Mg8; Figure 6B). Among the most upregulated interactions in BR3 were L-R pairs previously associated with microglia anti-inflammatory pathways (e.g., CD200_CD200R1, GAS6_MERTK), amyloid precursor response (e.g., APP_SORL1/TREM2), as well as those involved in maintenance of microglia homeostatic function, including phagocytosis (e.g., APOE_TREM2_TYROBP) and neuro-function (e.g., PTPRM-PTPRM) (Figure 6C). The predominant predicted tumor-to-microglia interactions in this model were driven by tumor junctional adhesion molecule (JAM) and extracellular matrix (ECM) ligands, such as collagens (e.g., COL4A2, COL6A3) and laminins (e.g., LAMA3, LAMC1; Figure 6C).

We then investigated the downstream microglia – T cell crosstalk. We found significantly stronger interactions from microglia to T cells, specifically $CD8^+$ T cells, in BR1 compared to BR3 (Figures 6A, S6A). The reactive microglia states, which receive signals from BR1 tumor cells, were the ones predicted to preferentially interact with T cells in BR1 (Figure 6B). This crosstalk involved all the

necessary signals to efficiently activate T cell responses, such as adhesion molecules, antigen presentation, TCR and co-stimulatory signaling (Figures 6C, S6B), explaining the T cell landscape observed in BR1. The inferred communications from microglia to $CD8^+$ T cells were also characterized by T cell-attracting chemokines (Figure 6C)[78–80], further suggesting that BR1 microglia are responsible for $CD8^+$ T cell recruitment. We confirmed that these chemokine-encoding genes were predominantly expressed by BR1 microglia, with significantly higher protein levels found in BR1 compared to BR3 whole-brain lysates (Figures 6D-E, S6C). In marked contrast to BR1, the few microglia – T cell interactions predicted in BR3 involved only cell-cell adhesion processes between microglia homeostatic states (Mg1, Mg2, and Mg8) and naïve T cells (SELL) (Figures 6B-C, S6B).

To confirm these predicted interactions using an independent approach, we performed a correlation analysis of cell populations identified by flow cytometry. In agreement with the interactome analysis, we observed positive correlations between BR1-reactive microglia (Mg.D) and $CD8^+$ T cells expressing activation markers (CD8.F3-F5) (Figures 6F). No correlations were observed between the BR3-associated microglia (Mg.A-C) and $CD8^+$ T cell (Figures 6F). Altogether, these findings support our hypothesis that BR1 and BR3 tumor cell-intrinsic programs dictate microglia functional states, which in turn shape T cell phenotypes.

The molecular features identified in our preclinical models predict T cell infiltration and BrM patient survival.

To further validate the clinical relevance of our findings, we interrogated the potential associations of our ICB-responder and ICB-resistant signatures with BrTME composition and patient survival in publicly available datasets[13,21]. We first focused on the association between BR1 and BR3 MPs and $CD8^+$ T cell infiltration in untreated melanoma patients[13]. To do so, we extracted $CD8^+$ T cells from their scRNA-seq dataset and re-analyzed them using unsupervised clustering (Figure 7A). Consistent with our preclinical data, we found that the frequency of total $CD8^+$ T cells within the biopsies positively correlated with BR1 immune-MP4 activity and negatively correlated with BR3 neuro-MP6 (Figure 7B). Out of the nine $CD8^+$ T cell clusters identified in the BrM patients, eight shared similarities with the subsets found in our BrM models (clusters 0, 1, 3-8) (Figure 7A, S6D). All BR3 enriched MPs (MP2, MP6, MP7) showed a trend toward positive correlation with the $CD8^+$ T cluster 5 resembling BR3 $CD8^+$ T cells (Figures 7C, S6D). Conversely, $CD8^+$ T cell cluster 8 resembling BR1 proliferative/cytotoxic $CD8^+$ T cells showed a trend of positive correlation with BR1 MPs and negative with BR3 MPs (Figures 7C, S6D).

We corroborated our observations using pseudobulk RNA-seq analysis of data from a larger patient cohort of pan-cancer BrM, composed of individuals untreated or treated with various therapies,

including ICB[21]. Total CD8$^+$ T cell signature showed a significant positive correlation with BR1 immune-MP4 and a trend to negatively correlate with BR3 neuro-MP6 (Figures 7D, S6E; Table S6). Additionally, molecular signatures recently reported in patients as "potential tumor reactive T cell" (pTRT), both in BrM (BrM pTRT)[19] and extracranial tumors[81–85] showed a similar correlation pattern (Figures 7E, S6E; Table S6). These signatures were also expressed at a higher level in BR1 CD8$^+$ T cells compared to BR3 (Figure 7F, S6F). Furthermore, we found a trend toward better progression-free survival (PFS) with high expression of the BR1 MP4 signature, while the BR3 neuro-MP6 was significantly associated with worse outcomes (Figure 7G, Table S6). We generated three additional signatures based on interactome and DEGs between BR1 and BR3: "BR1 pro-inflammatory", "BR1 chemokines", and "BR3 Neuro" (Table S6; see Methods). These signatures were confirmed to be more highly expressed in the corresponding groups using pseudobulk RNAseq analysis of our mouse BrM data set (Figure S6G). We found that the "BR1-proinflammatory" and "BR1 chemokine" signatures significantly correlated with better patient outcomes, whereas the "BR3 Neuro" signature was significantly associated with poorer PFS (Figure 7G). Taken together, our data demonstrate that the molecular signatures characteristic of our preclinical mouse models are also expressed in patient BrMs, correlate with their BrTME composition, and can predict patient outcomes.

DISCUSSION

BrM remains a critical challenge in cancer treatment with most cases being resistant to ICB[3–5,7,86,87]. Unfortunately, the limited availability of patient biopsies and sparsity of immunocompetent preclinical models representing diverse ICB responses[23–25,88] has hampered efforts to identify biomarkers and determinants of efficacy. Here, we have developed two translationally relevant melanoma BrM mouse models that overcome these limitations, enabling us to identify tumor molecular signatures that influence the BrTME and therapy responses. We show that ICB-responder BrMs (BR1) express a molecular program of response to IFN, antigen presentation, and inflammatory pathways that polarizes microglia into reactive states. These microglia are characterized by high expression of MHC-I/II, co-stimulatory molecules, and T cell-recruiting chemokines, which enhance T cell recruitment and activation, favoring ICB efficacy. In contrast, resistant BrMs (BR3) express programs involved in neurological function and evade the immune response by preserving a homeostatic state within the BrTME. Importantly, we validated the translational relevance of our findings by demonstrating that BR1 signatures positively correlated with T cell infiltration in human BrMs, and were associated with improved patient outcomes, whereas BR3 signatures showed negative correlation with T cells and were associated with poorer patient outcomes.

We found striking differences between responder and resistant models in the BrTME T cell subsets. The presence of a proliferative T cell subset in the responder model suggests that local expansion may contribute to shaping T cell landscape in the brain. An interesting finding from our study is that therapy induces an increase in T cell infiltration in both responder and non-responder models; however, the phenotypic characteristics of these cells were markedly distinct. These observations can help explain contradictory results observed from studies showing a positive correlation between T cell infiltration and improved patient outcomes vs. others that did not[21,89–92], stressing the importance of studying other immune populations that may influence T cell function. Indeed, our findings reveal that not only T cells but also microglia distinguish responders from non-responders. We show that specific reactive microglia states are significantly enriched in ICB responders and positively correlate with $CD8^+$ T cell infiltration. Although the relationship between microglia – T cell crosstalk and therapy responses has not been explored in patients, recent studies have reported positive correlations between MHC-II expression in microglia and $CD8^+$ T cells in BrM patients[19,89]. Supporting our results, previous data have shown that microglia sharing some of the BR1 signatures can attract or activate T cells in other contexts, such as CNS infection[93,94], Alzheimer's disease[95], or glioblastoma (GBM) treated with ICB[96]. Of note, CXCL9 alone or MHC-II^+ reactive microglia were recently found to be required for GBM response to PD-1 or CTLA-4 blockade, respectively[96,97].

Recent studies using breast and lung BrM preclinical models have shown that microglia with some BR1-reactive characteristics could suppress T cell activity and support BrM development, while others have demonstrated that microglia can recruit T cells and impair BrM progression[54,56,98,99]. These dual microglia functions are not mutually exclusive and suggest a context-dependent role. We observed that BR1 microglia states express different T cell immune checkpoints, which can paradoxically both induce and limit T cell activation in the absence of treatment. When these inhibitor axes are targeted by ICB, they unleash the T cells' anti-tumor potential. Thus, our findings indicate that microglia can play context-dependent roles in BrM based on the brain tumor subtype and the therapy utilized. Moreover, our observations can help explain the inconsistent pro- and anti-tumor impact of microglia depletion observed across independent preclinical studies[10,54,56,98]. While depleting microglia has been suggested as a potential therapeutic approach for brain tumors, our data indicate that such a strategy could be more harmful than beneficial depending on the context. Instead, modulating the balance between pro- and anti-tumor microglia states might be a more effective alternative. Here we reveal four major types of interactions used preferentially by the ICB-resistant BR3 tumors to shape microglia states: (1) ligands known to inhibit microglia reactivity such as CD200 and Gas6[100–103], (2) response to amyloid precursor, (3) components of the extra-cellular matrix such as collagens and laminins, and

(4) ligands implicated in neurological processes. In the CNS, these axes mediate crosstalk involving microglia and other cells (e.g., neurons, astrocytes, and endothelial cells) and are crucial to maintaining brain homeostasis and resolve neuroinflammation[100,104–112]. Others have described the pro-tumoral effect of CD200-CD200R and Gas6-MertK axes in primary brain tumors[102], and amyloid beta in melanoma BrM[113]. A recent report implicated collagens in murine breast and lung BrM growth[98]. The latter study demonstrated that tumor-derived collagen polarizes pro-tumor microglia through TNFα-NF-κB signaling, suppressing T cell infiltration and activation[98]. We found this pathway differentially upregulated in BR3 microglia, suggesting that similar interactions might contribute to the BR3 BrTME profile and its ICB-resistance. Additionally, while no direct link has been established between neurotransmitters and BrM response to therapy, independent studies have shown that glutamate can support GBM growth[114,115] and decrease microglia reactive states[108]. Thus, our findings suggest that the ICB-resistant BR3 BrM model hijacks natural CNS tolerance systems to support homeostatic microglia, to inhibit reactive states, and to promote pro-tumoral polarization. The molecular axes that we identified not only deepen our understanding of how BrM tumors shape the BrTME but also provide potential targets for overcoming therapy resistance[114,115].

We further show that BrM tumor cells with proliferative and inflammatory signatures (BR1) benefit from ICB therapies, whereas BrM tumor cells enriched in neurological features, such as axon guidance (BR3), do not and may require alternative or additional strategies, such as targeting myeloid cells or tumor ligands. We extended our findings to a pan-cancer BrM cohort, confirming that BR1 and BR3 signatures correlate with $CD8^+$ T cell infiltration and patient outcomes. These observations provide potential predictive biomarkers and valuable insights for treatment decision-making.

An important hurdle to improving BrM therapy is the difficulty in accessing patient samples, underscoring the importance of relevant preclinical models to elucidate mechanisms of resistance. Through the generation of new models that recapitulate the complexity and clinical behavior of human BrMs, we identified key molecular features associated with ICB response. Therefore, the BR1 and BR3 models constitute a valuable resource to perform mechanistic studies. Our comparative and integrative analyses of mouse and human data have provided critical insights into the mechanisms governing treatment response, contributing toward the development of more effective therapeutic options for BrM patients.

Limitations of the study

Here we focused on the immune and the tumor cell compartments, but we cannot rule out the role of other important BrTME actors, such as astrocytes and endothelial cells. Further studies should

investigate how these cell types can influence ICB responses. An important limitation in the field, that persists in our study, is the dearth of available human BrM samples, which limits the possibility to directly associate ICB response status and different BrM features in patients. Although we demonstrated that BR1 and BR3 signatures are associated with the patients' BrTME and survival in cohorts that included ICB treatment, it will be important to test our findings when larger cohorts of treated patients become available. A remaining unmet need is the ability to identify valuable predictors of response employing less invasive approaches, such as monitoring blood or cerebrospinal fluid. Despite these constraints, our report significantly enhances our understanding of the mechanisms by which BrM tumor cells can impact BrTME and ICB responses. We anticipate that our findings will facilitate the development of new therapeutic approaches and help inform clinical trials for melanoma patients with brain metastases.

ACKNOWLEDGMENTS

We thank Patricia Steeg's laboratory, particularly Alex Wu, for their advice and help with the BrM model development. We are grateful to the following NCI facilities: CCR Single Cell Analysis Facility, SpiTR Nanoscale Protein Analysis Section, LGI Flow Cytometry Core, CCR Genomics Technology Laboratory, NIH Animal Facility Bethesda and Frederick, and NCI LASP Small Animal Imaging Program (SAIP). We also thank Jennifer Dwyer (LCBG) and Katerina Grafanaki (University of Patras, School of Medicine) for technical help, Christophe Cataisson (LCBG) and Grégoire Atlan-Bonnet (LICI) for access to equipment, and members of LICI and LCBG for their helpful discussion. This research was supported in full by the Intramural Research Program of the NIH (CCR-NCI), including CCR FLEX Synergy Award, and a CCR Excellence in Postdoctoral Research Transition Award (2020) to EP-G. GK was supported by a Fulbright Foundation Visiting Research Fellowship from Greece (2023–2024). EP-G was supported in part by the Spanish *Agencia Estatal de Investigación* (RYC2021-034893-I and PID2022-141113OA-I00) and a Young Investigator Award from Melanoma Research Alliance (Ref: #1037420). This work utilized the computational resources of the NIH HPC Biowulf cluster (https://hpc.nih.gov).

DECLARATION OF INTERESTS

The authors declare no competing interests.

INCLUSION AND DIVERSITY

One or more of the authors of this paper self-identifies as an underrepresented ethnic minority in science. One or more of the authors of this paper self-identifies as a member of the LGBTQ+ community

Daugherty-Lopès et al. Figure 1

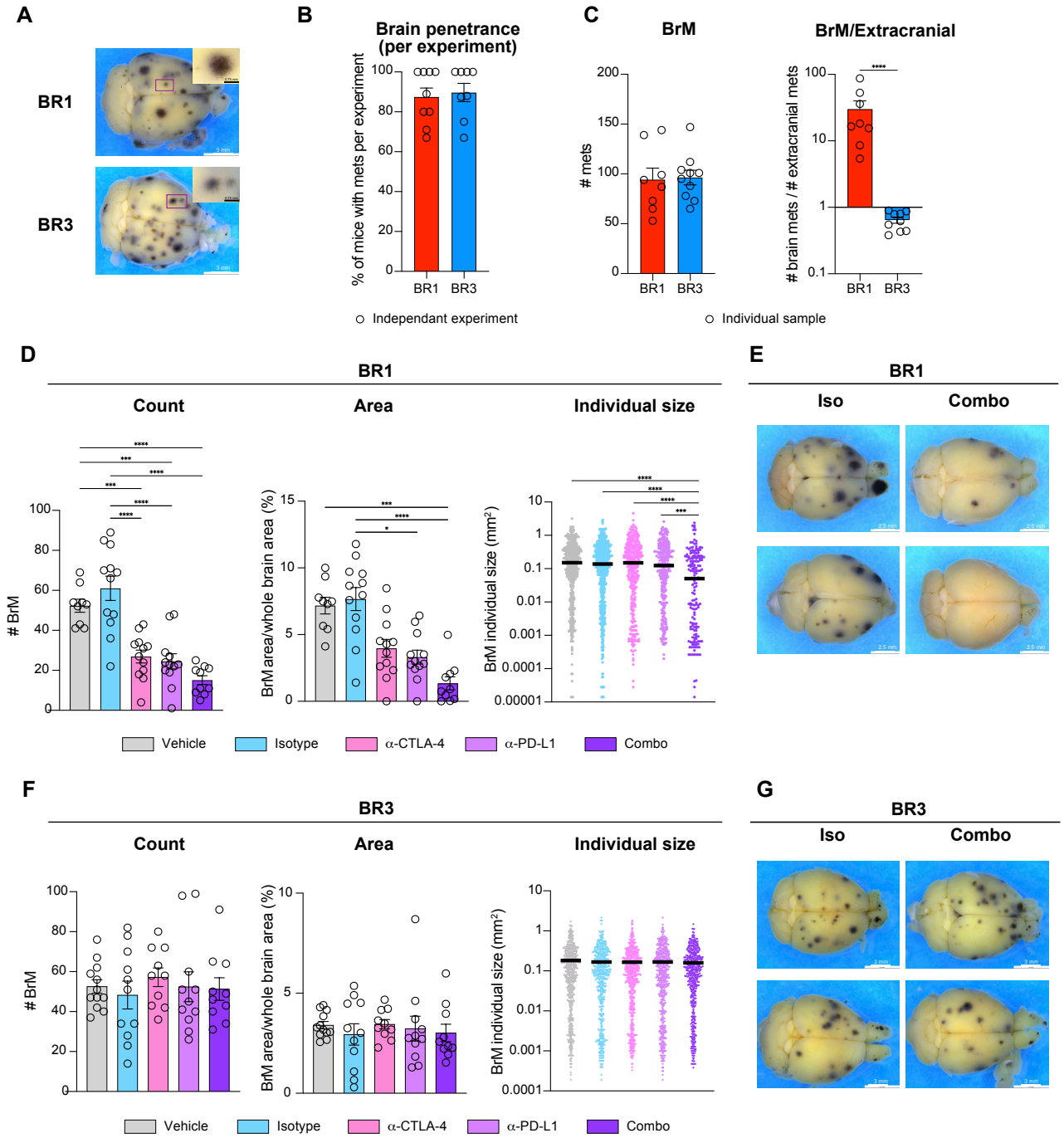

Figure 1. Generation of immunocompetent melanoma BrM models that exhibit ICB responses similar to brain metastases in patients.

(A) Representative stereomicroscope images of whole brains (left) and zoomed-in image of BrM (inset) from BR1 and BR3 bearing animals. (B) Percentage of mice with BrM per experiment; dots depict independent experiments. (C) BrM count (left) and BrM/extracranial metastases ratio (right) per mouse; dots depict individual animals within an experiment. (D-G) BR1 or BR3 bearing animals injected with PBS (vehicle) or treated with isotype control (Iso), anti-CTLA-4 (α-CTLA-4), anti-PD-L1 (α-PD-L1), or anti-PD-L1 + anti-CTLA-4 combination therapy (Combo). (D) BR1 BrM count per individual brain (left), total brain metastatic area per individual brain (middle), and size of individual BrM lesion (right). (E) Representative brain stereomicroscope images from Iso- and Combo-treated BR1 bearing animals. (F-G) Same as D-E but for BR3 bearing mice. B-C shown as mean ± SEM, data from 9 (B) or 3 (C) experiments combined, n=3-12 mouse/group/experiment. D-G representative of 2 independent experiments for each model, data shown as mean ± SEM, n=9-12/group/experiment. *$p < 0.05$, ***$p < 0.001$, ****$p < 0.0001$. See also Figure S1 and Table S1.

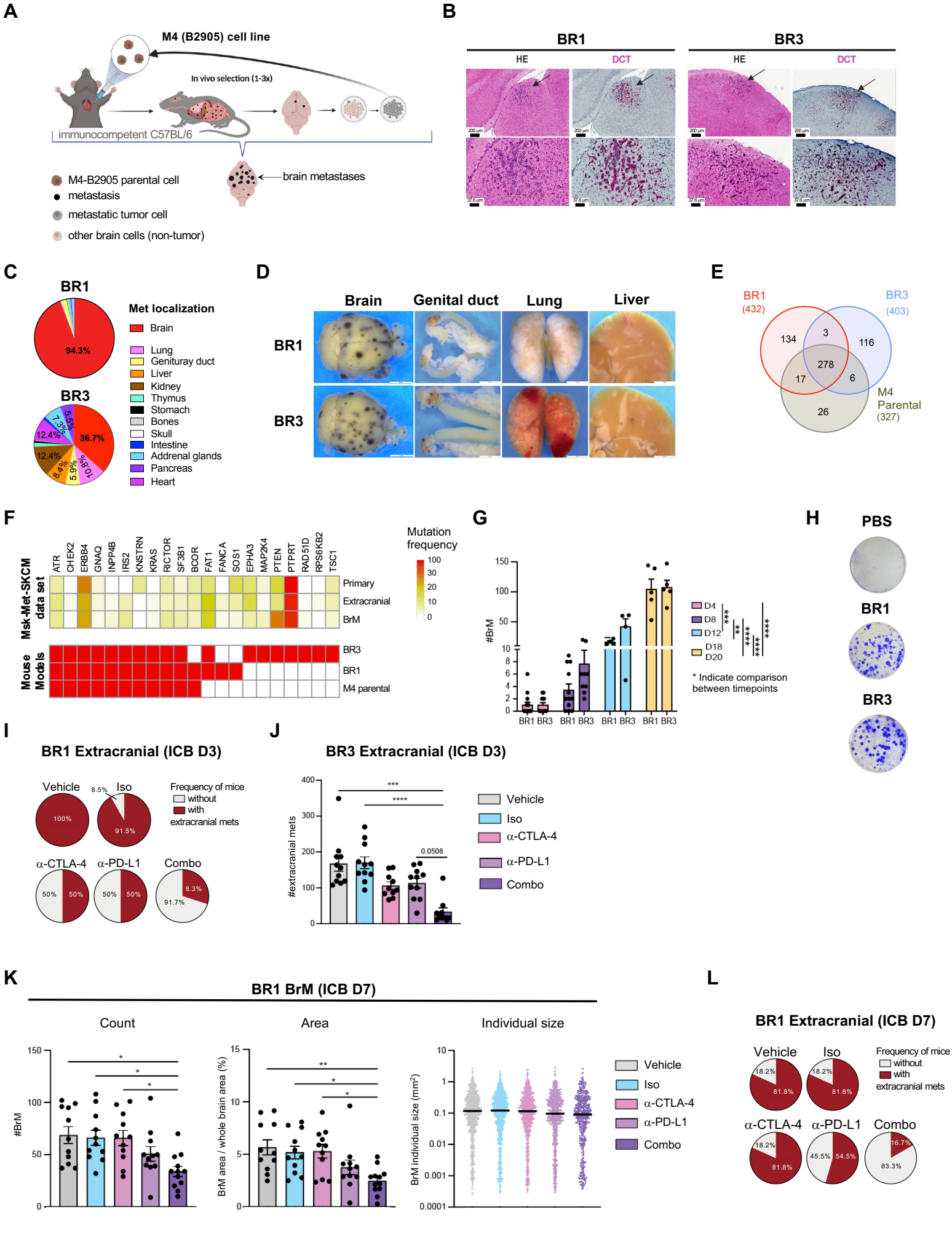
A
M4 (B2905) cell line
In vivo selection (1-3x)
immunocompetent C57BL/6
brain metastases
M4-B2905 parental cell
metastasis
metastatic tumor cell
other brain cells (non-tumor)
B
BR1
BR3
HE
DCT
C
BR1
94.3%
BR3
36.7%
10.8%
5.9%
8.4%
12.4%
12.4%
7.3%
5.5%
Met localization
Brain
Lung
Geniturary duct
Liver
Kidney
Thymus
Stomach
Bones
Skull
Intestine
Addrenal glands
Pancreas
Heart
D
Brain
Genital duct
Lung
Liver
BR1
BR3
E
BR1 (432)
BR3 (403)
M4 Parental (327)
134
3
116
278
17
6
26
F
ATR
CHEK2
ERBB4
GNAQ
INPP4B
IRS2
KNSTRN
KRAS
RICTOR
SF3B1
BCOR
FAT1
FANCA
SOS1
EPHA3
MAP2K4
PTEN
PTPRT
RAD51D
RPS6KB2
TSC1
Msk-Met-SKCM data set
Primary
Extracranial
BrM
Mouse Models
BR3
BR1
M4 parental
Mutation frequency
100
30
20
10
0
G
#BrM
BR1 BR3 BR1 BR3 BR1 BR3 BR1 BR3
D4
D8
D12
D18
D20
* Indicate comparison between timepoints
H
PBS
BR1
BR3
I
BR1 Extracranial (ICB D3)
Vehicle
Iso
8.5%
91.5%
100%
Frequency of mice
without
with extracranial mets
α-CTLA-4
α-PD-L1
Combo
50%
50%
8.3%
91.7%
J
BR3 Extracranial (ICB D3)
#extracranial mets
0.0508
Vehicle
Iso
α-CTLA-4
α-PD-L1
Combo
K
BR1 BrM (ICB D7)
Count
Area
Individual size
#BrM
BrM area / whole brain area (%)
BrM individual size (mm²)
Vehicle
Iso
α-CTLA-4
α-PD-L1
Combo
L
BR1 Extracranial (ICB D7)
Vehicle
Iso
18.2%
81.8%
Frequency of mice
without
with extracranial mets
α-CTLA-4
α-PD-L1
Combo
45.5%
54.5%
16.7%
83.3%

Figure S1. Characterization of the metastatic potential, mutational landscapes, and ICB responses of BR1 and BR3 models, related to Figure 1.

(A) Experimental design for the development of BrM melanoma models. (B) Hematoxylin / eosin (HE) and dopachrome tautomerase (DCT; pink) immunostaining images of brain sagittal sections showing BR1 (left panels) and BR3 (right panels) BrMs. Magnification 15x (top) and 40x (bottom). (C) Percentage of metastasis per organ in BR1 (top) and BR3 (bottom) models. (D) Representative stereomicroscope images of the indicated organs from BR1 and BR3 BrM-bearing animals. (E) Venn diagram showing the number of genes mutated and their overlap between the indicated cell lines. (F) Mutation frequency of indicated genes found in the brain-metastatic cell lines (marked in red in bottom heatmap), BrMs, extracranial metastases, and primary tumors from patients with BrMs from the MSK MetTropism cutaneous melanoma (SKCM) dataset. Color scale represents the mutation frequency in the indicated sample group. (G) BrM counts at the indicated time point after intracardiac injection (i.c.) in BR1 and BR3 bearing animals. D18/D20 indicate harvest at experimental endpoint. Asterix indicated difference between indicated timepoints. (H) Macroscopic pictures of cultured cell colonies recovered from mouse brains from BR1 and BR3 bearing animals or non-BrM control (PBS). (I) Proportion of mice with or without BR1 extracranial metastases after treatment on day 3 post tumor injection with PBS (vehicle), isotype control (Iso), anti-CTLA-4 (α-CTLA-4) or anti-PD-L1 (α-PD-L1) alone, or anti-PD-L1 + anti-CTLA-4 combination therapy (Combo). (J) BR3 extracranial metastatic count per mouse in animals treated as in I. (K) BR1 BrM count (left), total brain metastatic area per individual brain (middle), and size of individual BrM lesion (right) from animals treated as in I starting treatment on day 7 post tumor injection. (L) Proportion of animals from K with or without extracranial metastases. B one representative of 2 experiments, n=2-5 mouse/group/experiment. C data from 3 experiments combined, n=2-5 mouse/group/experiment. D one representative of 3 independent experiments, n=2-5 mouse/group/experiment. G data combined from 2 independent experiments, n = 2-5 mouse/group/experiment. I-L representative of 2 independent experiments per model, n = 9-12/group/experiment. G, J, K data shown as mean ± SEM *p <0.05, **p <0.01, ***p < 0.001, ****p < 0.0001. See also Table S1

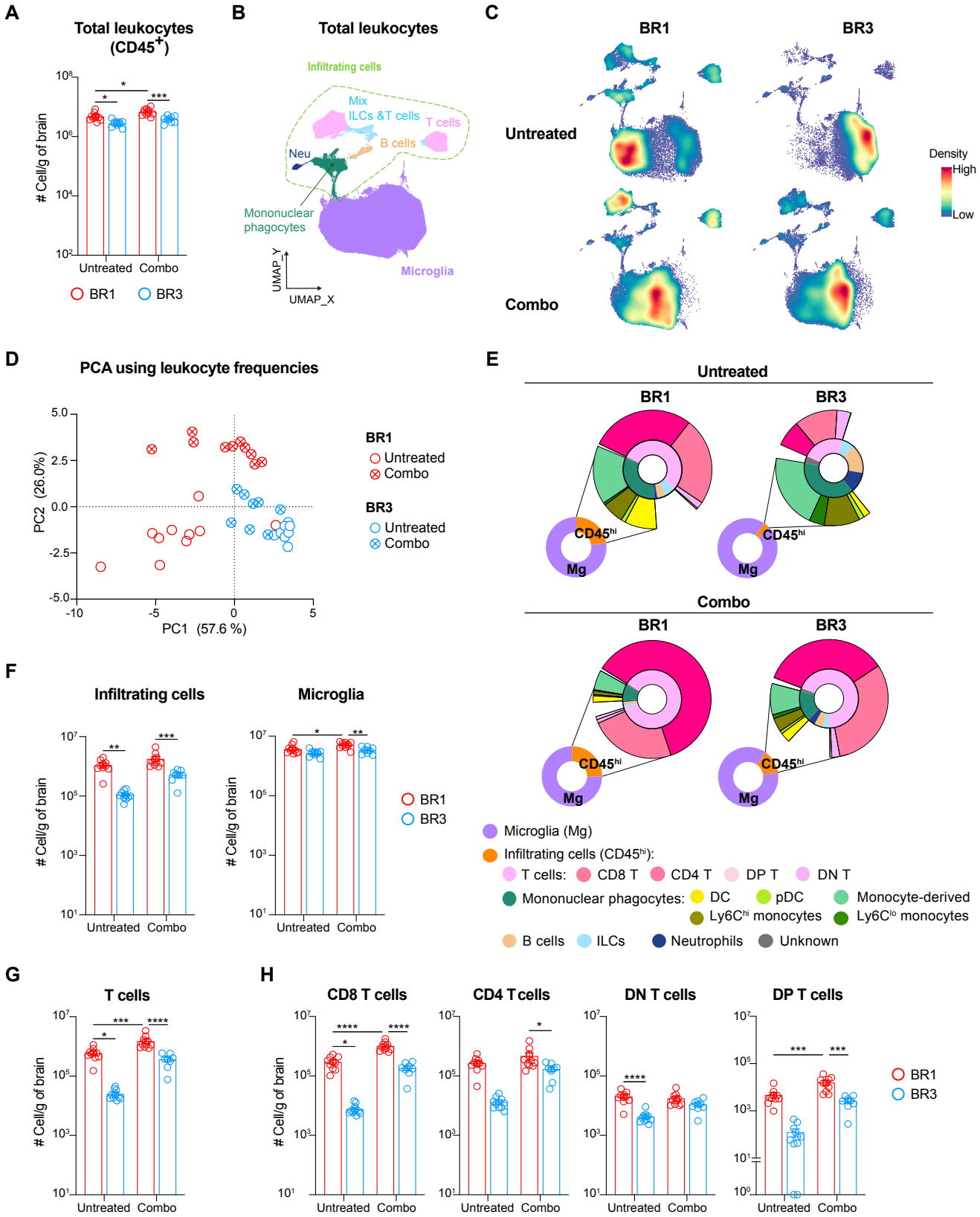
A
Total leukocytes (CD45+)
Cell/g of brain
Untreated
Combo
BR1
BR3
B
Total leukocytes
Infiltrating cells
Mix
ILCs &T cells
T cells
B cells
Neu
Mononuclear phagocytes
Microglia
UMAP_Y
UMAP_X
C
BR1
BR3
Untreated
Combo
Density
High
Low
D
PCA using leukocyte frequencies
PC2 (26.0%)
PC1 (57.6 %)
BR1
Untreated
Combo
BR3
Untreated
Combo
E
Untreated
BR1
BR3
CD45hi
Mg
Combo
F
Infiltrating cells
Microglia
Cell/g of brain
Untreated
Combo
BR1
BR3
Microglia (Mg)
Infiltrating cells (CD45hi):
T cells:
CD8 T
CD4 T
DP T
DN T
Mononuclear phagocytes:
DC
pDC
Monocyte-derived
Ly6Chi monocytes
Ly6Clo monocytes
B cells
ILCs
Neutrophils
Unknown
G
T cells
H
CD8 T cells
CD4 T cells
DN T cells
DP T cells

Figure 2. Distinct BrTME composition is associated with different responses to ICB.

High-parametric spectral flow cytometry analysis of brain leukocytes from BR1 and BR3 bearing animals untreated or combo treated. (A) Absolute number of leukocytes (live $CD45^{+}$) per gram of brain tissue. (B) UMAP projection of total BrM leukocytes. Main populations indicated: resident microglia, infiltrating mononuclear phagocytes, neutrophils (Neu), B cells, innate lymphoid cells (ILCs), and T cells. (C) Density plots showing cell distribution in untreated (top) and treated (bottom) mice from BR1 (left) and BR3 (right) models. (D) Principal Component Analysis (PCA) of main immune cell population frequencies in total leukocytes for each sample. (E) Proportion of microglia (Mg; purple) and infiltrating cells ($CD45^{hi}$; orange) in total leukocytes. Proportion of indicated populations within total infiltrating cells (inset). (F) Absolute number of infiltrating cells (left) and microglia (right) per gram of brain. (G) Absolute number of total T cells per gram of brain. (H) Absolute number of indicated T cell subsets per gram of brain. A, F, G, and H data shown as mean ± SEM, n = 8-10/group/experiment. *$p < 0.05$, **$p < 0.01$, ***$p < 0.001$, ****$p < 0.0001$. See also Figure S2 and Table S2.

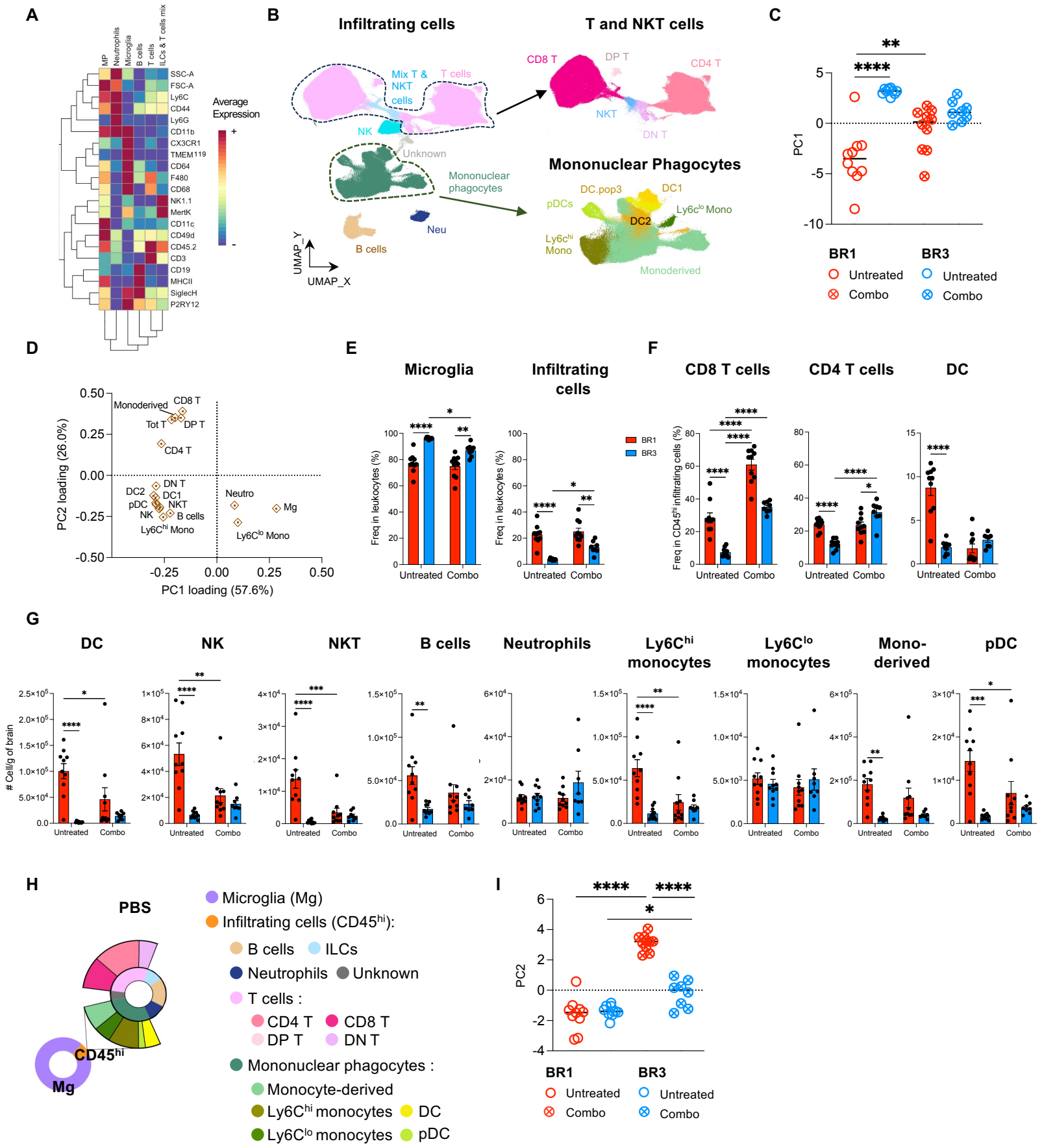
A
MP
Neutrophils
Microglia
B cells
T cells
ILCs & T cells mix
SSC-A
FSC-A
Ly6C
CD44
Ly6G
CD11b
CX3CR1
TMEM119
CD64
F480
CD68
NK1.1
MertK
CD11c
CD49d
CD45.2
CD3
CD19
MHCII
SiglecH
P2RY12
Average Expression
B
Infiltrating cells
Mix T & NKT cells
T cells
NK
Unknown
Mononuclear phagocytes
Neu
B cells
UMAP_Y
UMAP_X
T and NKT cells
CD8 T
DP T
CD4 T
NKT
DN T
Mononuclear Phagocytes
DC.pop3
DC1
pDCs
Ly6c^lo Mono
DC2
Ly6c^hi Mono
Monoderived
C
PC1
BR1
BR3
Untreated
Combo
D
PC2 loading (26.0%)
PC1 loading (57.6%)
Monoderived
CD8 T
Tot T
DP T
CD4 T
DN T
DC2
DC1
pDC
NKT
NK
B cells
Ly6C^hi Mono
Neutro
Mg
Ly6C^lo Mono
E
Microglia
Infiltrating cells
Freq in leukocytes (%)
Untreated
Combo
F
CD8 T cells
CD4 T cells
DC
Freq in CD45^hi infiltrating cells (%)
G
DC
NK
NKT
B cells
Neutrophils
Ly6C^hi monocytes
Ly6C^lo monocytes
Mono-derived
pDC
Cell/g of brain
H
PBS
CD45^hi
Mg
Microglia (Mg)
Infiltrating cells (CD45^hi):
B cells
ILCs
Neutrophils
Unknown
T cells :
CD4 T
CD8 T
DP T
DN T
Mononuclear phagocytes :
Monocyte-derived
Ly6C^hi monocytes
DC
Ly6C^lo monocytes
pDC
I
PC2
BR1
BR3
Untreated
Combo

Figure S2. Global immune BrTME characterization of untreated and treated BR1 and BR3 bearing brains, related to Figure 2.

(A) Heatmap representing expression level of indicated surface markers (scaled by marker) for each immune cluster with hierarchical clustering indicated on left and markers on top. (B) UMAP projection of indicated immune cells. NKT: natural killer T; T cell subsets: $CD8^{+}CD4^{-}$ (CD8 T), $CD8^{-}CD4^{+}$ (CD4 T), $CD8^{-}CD4^{-}$ (DN T), $CD8^{+}CD4^{+}$ (DP T); mononuclear phagocytes including dendritic cells [DC1, DC2, DC.pop3, plasmacytoid DC (pDCs)] and monocytes subsets [$Ly6C^{hi}$ mono and $Ly6C^{lo}$ mono]. (C) Quantification of principal component 1 (PC1) from Figure 2D. (D) PC1 and PC2 loadings from Figure 2D. (E-F) Proportion of indicated immune cells. (G) Absolute number of indicated immune cells per gram of brain. (H) Proportion of microglia (Mg; purple) and infiltrating cells ($CD45^{hi}$; orange) within total leukocytes in control (PBS) brains. Proportion of indicated populations in total infiltrating cells (inset). (I) PC2 quantification from Figure 2D. C, E-G, and I data shown as mean, n = 8-10/group/experiment. *$p < 0.05$, **$p < 0.01$, ****$p < 0.0001$. See also Table S2.

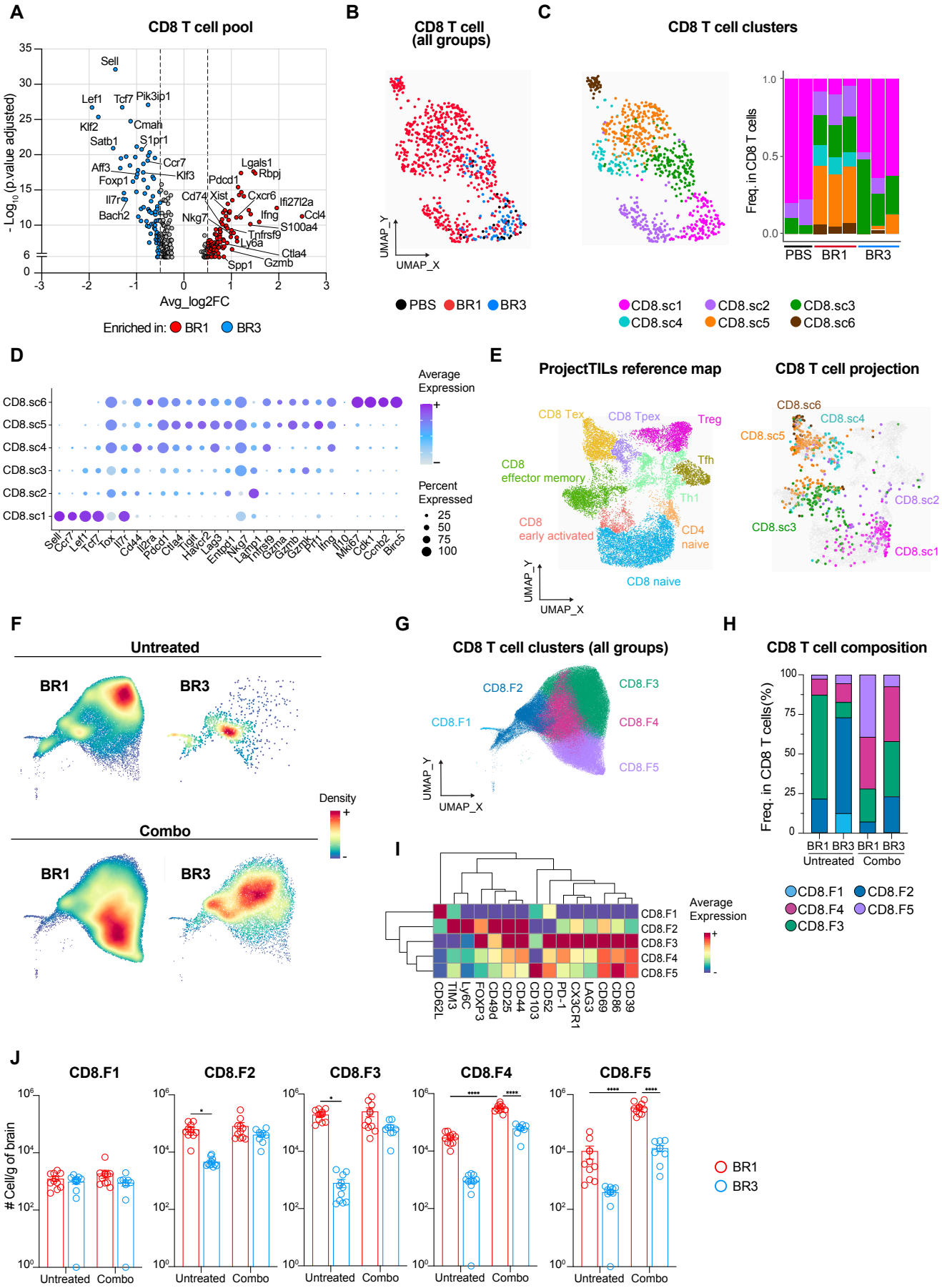
A
CD8 T cell pool
- Log10 (p.value adjusted)
Avg_log2FC
Sell
Lef1
Tcf7
Pik3ip1
Klf2
Cmah
Satb1
S1pr1
Aff3
Ccr7
Foxp1
Klf3
Il7r
Bach2
Pdcd1
Lgals1
Rbpj
Cd74
Xist
Cxcr6
Ifi27l2a
Nkg7
Ifng
Ccl4
S100a4
Tnfrsf9
Lyg6a
Ctla4
Spp1
Gzmb
Enriched in: BR1 BR3
B
CD8 T cell (all groups)
UMAP_Y
UMAP_X
PBS BR1 BR3
C
CD8 T cell clusters
Freq. in CD8 T cells
PBS BR1 BR3
CD8.sc1 CD8.sc2 CD8.sc3
CD8.sc4 CD8.sc5 CD8.sc6
D
Average Expression
Percent Expressed
CD8.sc6
CD8.sc5
CD8.sc4
CD8.sc3
CD8.sc2
CD8.sc1
Sell Ccr7 Lef1 Tcf7 Tox Il7r Cd44 Il2ra Pdcd1 Ctla4 Tigit Havcr2 Lag3 Entpd1 Nkg7 Lamp1 Tnfrsf9 Gzma Gzmb Gzmk Prf1 Ifng Il10 Mki67 Cdk1 Ccnb2 Birc5
E
ProjectTILs reference map
CD8 Tex
CD8 Tpex
Treg
Tfh
CD8 effector memory
Th1
CD8 early activated
CD4 naive
CD8 naive
UMAP_Y
UMAP_X
CD8 T cell projection
CD8.sc6
CD8.sc4
CD8.sc5
CD8.sc2
CD8.sc3
CD8.sc1
F
Untreated
BR1
BR3
Combo
BR1
BR3
Density
G
CD8 T cell clusters (all groups)
CD8.F2
CD8.F3
CD8.F1
CD8.F4
CD8.F5
UMAP_Y
UMAP_X
H
CD8 T cell composition
Freq. in CD8 T cells(%)
BR1 BR3 BR1 BR3
Untreated Combo
CD8.F1 CD8.F2
CD8.F4 CD8.F5
CD8.F3
I
Average Expression
CD8.F1
CD8.F2
CD8.F3
CD8.F4
CD8.F5
CD62L TIM3 Ly6C FOXP3 CD49d CD25 CD44 CD103 CD52 PD-1 CX3CR1 LAG3 CD69 CD86 CD39
J
CD8.F1
CD8.F2
CD8.F3
CD8.F4
CD8.F5
Cell/g of brain
Untreated Combo
BR1
BR3

Figure 3. Distinct CD8$^+$ T cell subsets infiltrate ICB-responder compared to ICB-resistant BrMs.

(A-E) scRNA-seq analysis of CD8$^+$ T cells from untreated BR1, BR3, and PBS brains. (A) Volcano plot of BR1 versus BR3 differentially expressed genes (DEGs). Significant DEGs are indicated (BR1: red, BR3: blue) (B) UMAP projection showing cell distribution in each group. (C) CD8$^+$ T cell clustering. UMAP projection (left) and proportion of each cluster per sample (right). (D) Dot plot showing the expression of selected genes among clusters. (E) Projection of CD8$^+$ T cell clusters (right) onto the single-cell reference atlas (left) for T cell states ProjecTILs. (F-J) High-parametric spectral flow cytometry analysis of CD8$^+$ T cells from indicated samples. (F) Density plots showing cell distribution in untreated (top) and treated (bottom) BR1 (left) and BR3 (right) models. (G) UMAP projection and clustering of indicated CD8$^+$ T cell clusters among total CD8$^+$ T cells. (H) Proportion of indicated CD8$^+$ T cell clusters in total CD8$^+$ T cells. (I) Heatmap depicting expression level of indicated surface markers (scaled by marker) in each CD8$^+$ T cell cluster. (J) Absolute number of indicated T cell clusters per gram of brain. A-E n = 2-3/group. F-J n = 8-10/group/experiment. J data shown as mean ± SEM, *$p < 0.05$, ****$p < 0.0001$. See also Figure S3 and Tables S3-S4.

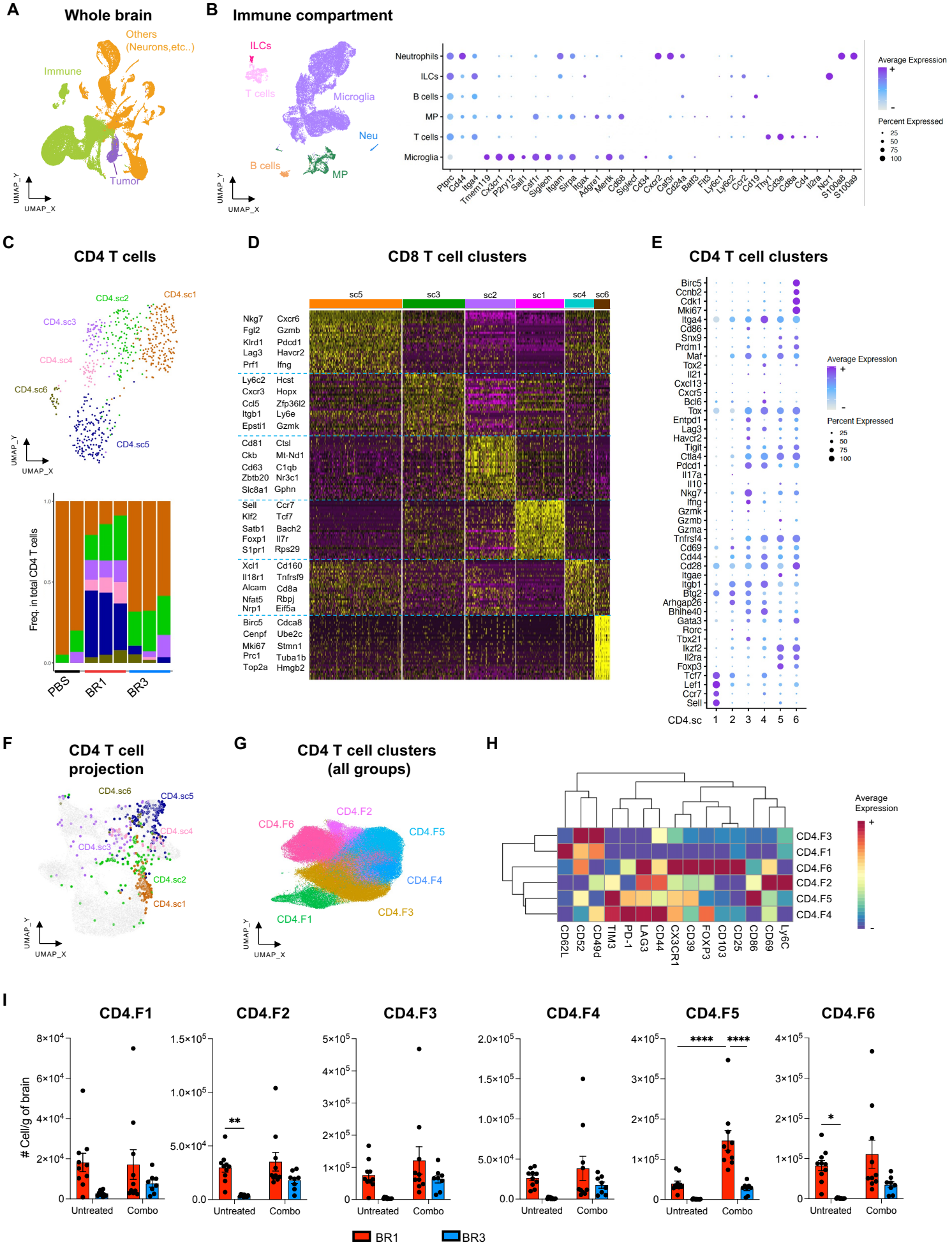
A
Whole brain
Others (Neurons,etc..)
Immune
Tumor
UMAP_Y
UMAP_X
B
Immune compartment
ILCs
T cells
Microglia
Neu
B cells
MP
Neutrophils
ILCs
B cells
MP
T cells
Microglia
Average Expression
Percent Expressed
C
CD4 T cells
CD4.sc1
CD4.sc2
CD4.sc3
CD4.sc4
CD4.sc5
CD4.sc6
Freq. in total CD4 T cells
PBS
BR1
BR3
D
CD8 T cell clusters
sc5
sc3
sc2
sc1
sc4
sc6
E
CD4 T cell clusters
Average Expression
Percent Expressed
CD4.sc
F
CD4 T cell projection
G
CD4 T cell clusters (all groups)
CD4.F1
CD4.F2
CD4.F3
CD4.F4
CD4.F5
CD4.F6
H
Average Expression
I
CD4.F1
CD4.F2
CD4.F3
CD4.F4
CD4.F5
CD4.F6
Cell/g of brain
Untreated
Combo
BR1
BR3

Figure S3. Distinct T cell characteristics found in the ICB-responder model, related to Figure 3.

(A-B) ScRNA-seq analysis of untreated BR1, BR3, and PBS whole brains. (A) UMAP projection of all cells. (B) UMAP projection of immune cells (left). Dot plot showing the expression of selected genes among clusters (right). (C-F) scRNA-seq analysis of indicated brain T cell populations. (C) UMAP projection of indicated $CD4^+$ T cell clusters among total $CD4^+$ T cells (top). Proportion of indicated $CD4^+$ T cell clusters in total $CD4^+$ T cells per sample (bottom). (D) Heatmap representing expression level of the top 30 $CD8^+$ T cell cluster-specific genes. (E) Dot plot showing the expression of selected genes among $CD4^+$ T cell clusters. (F) Projection of our $CD4^+$ T cell clusters onto the single-cell reference atlas for T cell states ProjecTILs. See figure 4E for the Reference map (left). (G-I) High-parametric flow cytometry analysis of $CD4^+$ T cells from BR1 and BR3 brains untreated or combo treated. (G) UMAP projection of $CD4^+$ T cell populations. (H) Heatmap representing expression level of indicated surface markers (scaled by marker) for each $CD4^+$ T cell cluster with hierarchical clustering indicated on left and markers on top. (I) Absolute number of indicated $CD4^+$ T cell clusters per gram of brain. A-D n = 2-3/group/experiment. F-G Data shown as mean ± SEM, n = 8-10/group/experiment. *$p < 0.05$, ***$p < 0.001$, ****$p < 0.0001$. See also Table S3-S4.

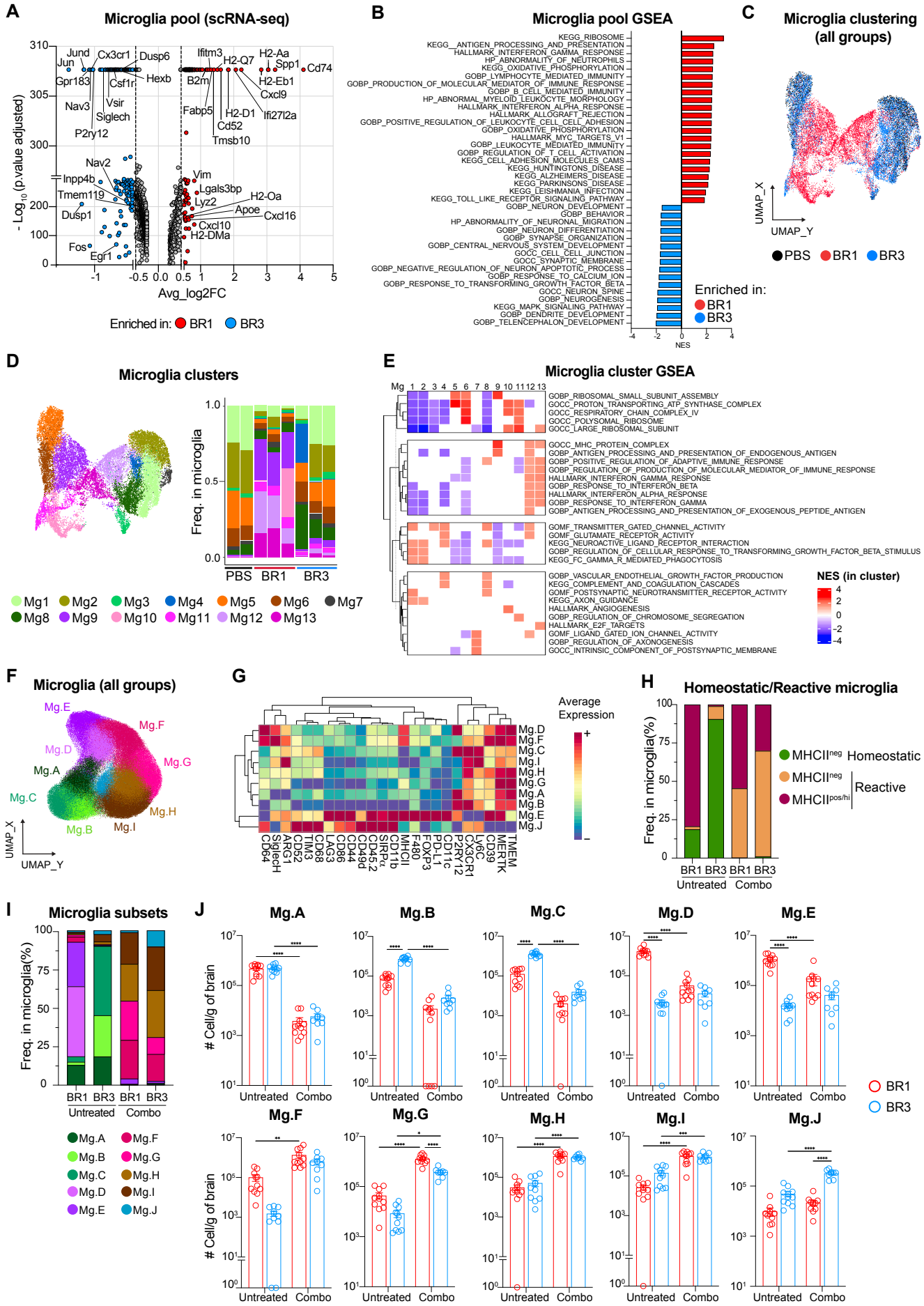
A
Microglia pool (scRNA-seq)
- Log10 (p.value adjusted)
Avg_log2FC
Jund
Jun
Cx3cr1
Dusp6
Gpr183
Csf1r
Hexb
Nav3
Vsir
Siglech
P2ry12
Ifitm3
H2-Q7
H2-Aa
Spp1
Cd74
B2m
H2-Eb1
Cxcl9
Fabp5
H2-D1
Ifi27l2a
Cd52
Tmsb10
Nav2
Inpp4b
Tmem119
Dusp1
Fos
Egr1
Vim
Lgals3bp
Lyz2
H2-Oa
Apoe
Cxcl16
Cxcl10
H2-DMa
Enriched in: BR1 BR3
B
Microglia pool GSEA
KEGG_RIBOSOME
KEGG_ANTIGEN_PROCESSING_AND_PRESENTATION
HALLMARK_INTERFERON_GAMMA_RESPONSE
HP_ABNORMALITY_OF_NEUTROPHILS
KEGG_OXIDATIVE_PHOSPHORYLATION
GOBP_LYMPHOCYTE_MEDIATED_IMMUNITY
GOBP_PRODUCTION_OF_MOLECULAR_MEDIATOR_OF_IMMUNE_RESPONSE
GOBP_B_CELL_MEDIATED_IMMUNITY
HP_ABNORMAL_MYELOID_LEUKOCYTE_MORPHOLOGY
HALLMARK_INTERFERON_ALPHA_RESPONSE
HALLMARK_ALLOGRAFT_REJECTION
GOBP_POSITIVE_REGULATION_OF_LEUKOCYTE_CELL_CELL_ADHESION
GOBP_OXIDATIVE_PHOSPHORYLATION
HALLMARK_MYC_TARGETS_V1
GOBP_LEUKOCYTE_MEDIATED_IMMUNITY
GOBP_REGULATION_OF_T_CELL_ACTIVATION
KEGG_CELL_ADHESION_MOLECULES_CAMS
KEGG_HUNTINGTONS_DISEASE
KEGG_ALZHEIMERS_DISEASE
KEGG_PARKINSONS_DISEASE
KEGG_LEISHMANIA_INFECTION
KEGG_TOLL_LIKE_RECEPTOR_SIGNALING_PATHWAY
GOBP_NEURON_DEVELOPMENT
GOBP_BEHAVIOR
HP_ABNORMALITY_OF_NEURONAL_MIGRATION
GOBP_NEURON_DIFFERENTIATION
GOBP_SYNAPSE_ORGANIZATION
GOBP_CENTRAL_NERVOUS_SYSTEM_DEVELOPMENT
GOCC_CELL_CELL_JUNCTION
GOCC_SYNAPTIC_MEMBRANE
GOBP_NEGATIVE_REGULATION_OF_NEURON_APOPTOTIC_PROCESS
GOBP_RESPONSE_TO_CALCIUM_ION
GOBP_RESPONSE_TO_TRANSFORMING_GROWTH_FACTOR_BETA
GOCC_NEURON_SPINE
GOBP_NEUROGENESIS
KEGG_MAPK_SIGNALING_PATHWAY
GOBP_DENDRITE_DEVELOPMENT
GOBP_TELENCEPHALON_DEVELOPMENT
NES
Enriched in:
BR1
BR3
C
Microglia clustering (all groups)
UMAP_X
UMAP_Y
PBS BR1 BR3
D
Microglia clusters
Freq. in microglia
PBS BR1 BR3
Mg1 Mg2 Mg3 Mg4 Mg5 Mg6 Mg7
Mg8 Mg9 Mg10 Mg11 Mg12 Mg13
E
Microglia cluster GSEA
GOBP_RIBOSOMAL_SMALL_SUBUNIT_ASSEMBLY
GOCC_PROTON_TRANSPORTING_ATP_SYNTHASE_COMPLEX
GOCC_RESPIRATORY_CHAIN_COMPLEX_IV
GOCC_POLYSOMAL_RIBOSOME
GOCC_LARGE_RIBOSOMAL_SUBUNIT
GOCC_MHC_PROTEIN_COMPLEX
GOBP_ANTIGEN_PROCESSING_AND_PRESENTATION_OF_ENDOGENOUS_ANTIGEN
GOBP_POSITIVE_REGULATION_OF_ADAPTIVE_IMMUNE_RESPONSE
GOBP_REGULATION_OF_PRODUCTION_OF_MOLECULAR_MEDIATOR_OF_IMMUNE_RESPONSE
HALLMARK_INTERFERON_GAMMA_RESPONSE
GOBP_RESPONSE_TO_INTERFERON_BETA
HALLMARK_INTERFERON_ALPHA_RESPONSE
GOBP_RESPONSE_TO_INTERFERON_GAMMA
GOBP_ANTIGEN_PROCESSING_AND_PRESENTATION_OF_EXOGENOUS_PEPTIDE_ANTIGEN
GOMF_TRANSMITTER_GATED_CHANNEL_ACTIVITY
GOMF_GLUTAMATE_RECEPTOR_ACTIVITY
KEGG_NEUROACTIVE_LIGAND_RECEPTOR_INTERACTION
GOBP_REGULATION_OF_CELLULAR_RESPONSE_TO_TRANSFORMING_GROWTH_FACTOR_BETA_STIMULUS
KEGG_FC_GAMMA_R_MEDIATED_PHAGOCYTOSIS
GOBP_VASCULAR_ENDOTHELIAL_GROWTH_FACTOR_PRODUCTION
KEGG_COMPLEMENT_AND_COAGULATION_CASCADES
GOMF_POSTSYNAPTIC_NEUROTRANSMITTER_RECEPTOR_ACTIVITY
KEGG_AXON_GUIDANCE
HALLMARK_ANGIOGENESIS
GOBP_REGULATION_OF_CHROMOSOME_SEGREGATION
HALLMARK_E2F_TARGETS
GOMF_LIGAND_GATED_ION_CHANNEL_ACTIVITY
GOBP_REGULATION_OF_AXONOGENESIS
GOCC_INTRINSIC_COMPONENT_OF_POSTSYNAPTIC_MEMBRANE
NES (in cluster)
F
Microglia (all groups)
Mg.E
Mg.F
Mg.D
Mg.G
Mg.A
Mg.C
Mg.H
Mg.B
Mg.I
UMAP_X
UMAP_Y
G
Average Expression
Mg.D
Mg.F
Mg.C
Mg.I
Mg.H
Mg.G
Mg.A
Mg.B
Mg.E
Mg.J
CD64 SiglecH ARG1 CD52 TIM3 CD68 LAG3 CD86 CD44 CD49d CD45.2 SIRPα CD11b MHCII F480 FOXP3 PD-L1 CD11c P2RY12 CX3CR1 Ly6C CD39 MERTK TMEM
H
Homeostatic/Reactive microglia
Freq. in microglia(%)
MHCIIneg Homeostatic
MHCIIneg
MHCIIpos/hi
Reactive
BR1 BR3 BR1 BR3
Untreated Combo
I
Microglia subsets
Freq. in microglia(%)
BR1 BR3 BR1 BR3
Untreated Combo
Mg.A Mg.F
Mg.B Mg.G
Mg.C Mg.H
Mg.D Mg.I
Mg.E Mg.J
J
Mg.A Mg.B Mg.C Mg.D Mg.E
Mg.F Mg.G Mg.H Mg.I Mg.J
Cell/g of brain
Untreated Combo
BR1
BR3

Figure 4. Unique reactive microglia signatures are found in ICB-responder BrMs.

(A-E) scRNA-seq analysis of microglia from untreated brains. (A) Volcano plot of BR1 (red) versus BR3 (blue) DEGs. (B) Gene set enrichment analysis (GSEA) showing selected pathways among the top 10 Hallmark (HP), Gene Ontology (GO), and Kyoto Encyclopedia of Genes and Genomes (KEGG) pathways enriched in BR1 (red) microglia versus BR3 (blue) (see Methods). NES: Normalized Enrichment Score. (C) UMAP projection of total microglia showing cell distribution among groups. (D) UMAP projection clustering (left) and proportion per sample (right) of indicated microglia clusters in total microglia. (E) GSEA showing selected HP, GO and KEGG top pathways enriched in each microglia cluster. NES: Normalized Enrichment Score in each cluster. (F-J) High-parametric spectral flow cytometry analysis of microglia from untreated or combo-treated BR1 and BR3 brains. (F) UMAP projection and unsupervised clustering. (G) Heatmap representing expression level of indicated surface markers (scaled by marker) for each cluster with hierarchical clustering indicated on left and markers on top. (H) Proportion of indicated microglia states in total microglia per group. (I) Proportion of indicated microglia clusters in total microglia per group. (J) Absolute number of indicated microglia clusters per gram of brain. A-E n = 2-3/group/experiment. F-J n = 8-10/group/experiment. J data shown as mean ± SEM, n = 8-10/group/experiment. *$p < 0.05$, **$p < 0.01$, ***$p < 0.001$, ****$p < 0.0001$. See also Figure S4.

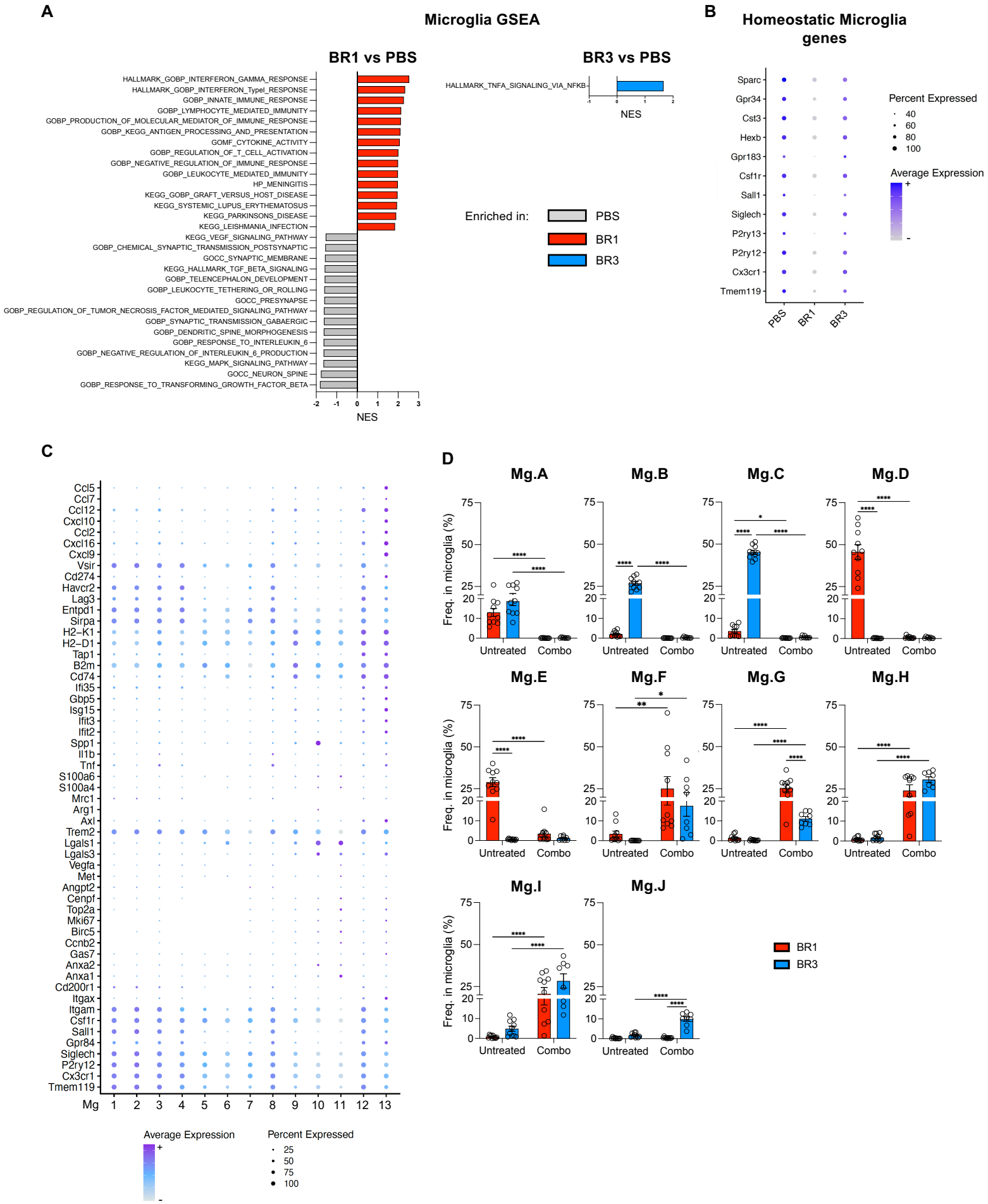
A
Microglia GSEA
BR1 vs PBS
HALLMARK_GOBP_INTERFERON_GAMMA_RESPONSE
HALLMARK_GOBP_INTERFERON_TypeI_RESPONSE
GOBP_INNATE_IMMUNE_RESPONSE
GOBP_LYMPHOCYTE_MEDIATED_IMMUNITY
GOBP_PRODUCTION_OF_MOLECULAR_MEDIATOR_OF_IMMUNE_RESPONSE
GOBP_KEGG_ANTIGEN_PROCESSING_AND_PRESENTATION
GOMF_CYTOKINE_ACTIVITY
GOBP_REGULATION_OF_T_CELL_ACTIVATION
GOBP_NEGATIVE_REGULATION_OF_IMMUNE_RESPONSE
GOBP_LEUKOCYTE_MEDIATED_IMMUNITY
HP_MENINGITIS
KEGG_GOBP_GRAFT_VERSUS_HOST_DISEASE
KEGG_SYSTEMIC_LUPUS_ERYTHEMATOSUS
KEGG_PARKINSONS_DISEASE
KEGG_LEISHMANIA_INFECTION
KEGG_VEGF_SIGNALING_PATHWAY
GOBP_CHEMICAL_SYNAPTIC_TRANSMISSION_POSTSYNAPTIC
GOCC_SYNAPTIC_MEMBRANE
KEGG_HALLMARK_TGF_BETA_SIGNALING
GOBP_TELENCEPHALON_DEVELOPMENT
GOBP_LEUKOCYTE_TETHERING_OR_ROLLING
GOCC_PRESYNAPSE
GOBP_REGULATION_OF_TUMOR_NECROSIS_FACTOR_MEDIATED_SIGNALING_PATHWAY
GOBP_SYNAPTIC_TRANSMISSION_GABAERGIC
GOBP_DENDRITIC_SPINE_MORPHOGENESIS
GOBP_RESPONSE_TO_INTERLEUKIN_6
GOBP_NEGATIVE_REGULATION_OF_INTERLEUKIN_6_PRODUCTION
KEGG_MAPK_SIGNALING_PATHWAY
GOCC_NEURON_SPINE
GOBP_RESPONSE_TO_TRANSFORMING_GROWTH_FACTOR_BETA
-2 -1 0 1 2 3
NES
BR3 vs PBS
HALLMARK_TNFA_SIGNALING_VIA_NFKB
-1 0 1 2
NES
Enriched in:
PBS
BR1
BR3
B
Homeostatic Microglia genes
Sparc
Gpr34
Cst3
Hexb
Gpr183
Csf1r
Sall1
Siglech
P2ry13
P2ry12
Cx3cr1
Tmem119
PBS
BR1
BR3
Percent Expressed
40
60
80
100
Average Expression
+
-
C
Ccl5
Ccl7
Ccl12
Cxcl10
Ccl2
Cxcl16
Cxcl9
Vsir
Cd274
Havcr2
Lag3
Entpd1
Sirpa
H2–K1
H2–D1
Tap1
B2m
Cd74
Ifi35
Gbp5
Isg15
Ifit3
Ifit2
Spp1
Il1b
Tnf
S100a6
S100a4
Mrc1
Arg1
Axl
Trem2
Lgals1
Lgals3
Vegfa
Met
Angpt2
Cenpf
Top2a
Mki67
Birc5
Ccnb2
Gas7
Anxa2
Anxa1
Cd200r1
Itgax
Itgam
Csf1r
Sall1
Gpr84
Siglech
P2ry12
Cx3cr1
Tmem119
Mg 1 2 3 4 5 6 7 8 9 10 11 12 13
Average Expression
+
-
Percent Expressed
25
50
75
100
D
Mg.A
Mg.B
Mg.C
Mg.D
Mg.E
Mg.F
Mg.G
Mg.H
Mg.I
Mg.J
Freq. in microglia (%)
Untreated
Combo
BR1
BR3

Figure S4. Distinct microglia are found in ICB-responder and resistant BrMs, related to Figure 4.

(A-C) scRNA-seq analysis of microglia from untreated BR1, BR3, and PBS brains. (A) GSEA showing HP, GO, and KEGG pathways selected among the top 10 enriched in total BR1 microglia versus PBS (left) and in total BR3 microglia versus PBS (right) (see Methods). (B) Dot plot showing the expression of homeostatic microglia genes per group. (C) Dot plot showing expression of selected genes among microglia clusters. (D) High-parametric spectral flow cytometry analysis of microglia from BR1 and BR3 bearing animals untreated or combo-treated. Proportion of indicated microglia clusters in total microglia. A-C n = 2-3/group/experiment. D n = 8-10/group/experiment. *$p < 0.05$, **$p < 0.01$, ***$p < 0.001$, ****$p < 0.0001$

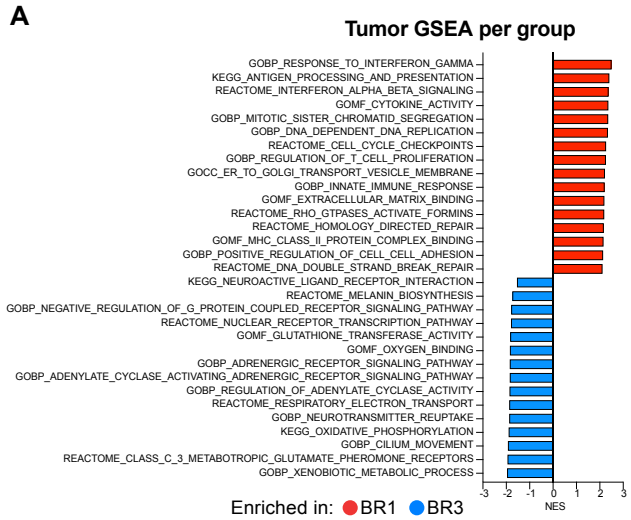

B

MP	Pathways associated
MP1	Cell cycle & DNA damage response
MP2	Melanin biosynthesis
MP3	Development and morphogenesis
MP4	Immune response & antigen presentation
MP5	Translation, RNA processing & mitochondrial metabolism
MP6	Neuron development & axon guidance
MP7	Melanin biosynthesis & fatty acid metabolism

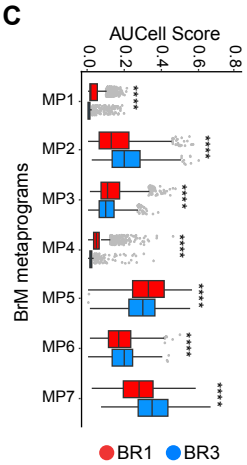

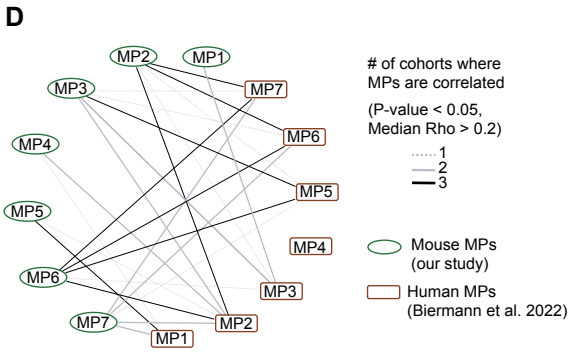

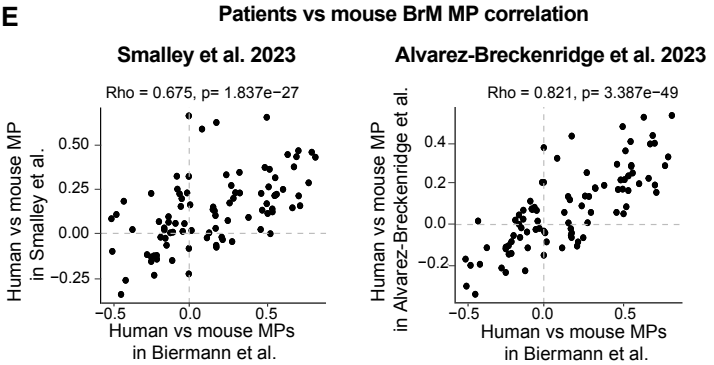

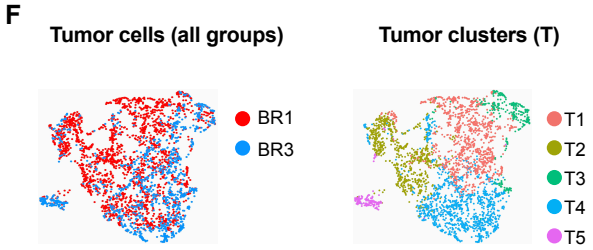

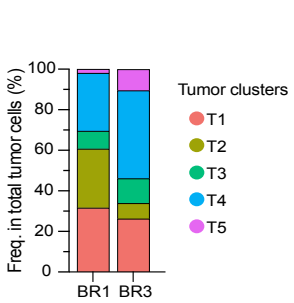

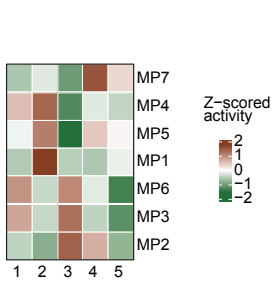

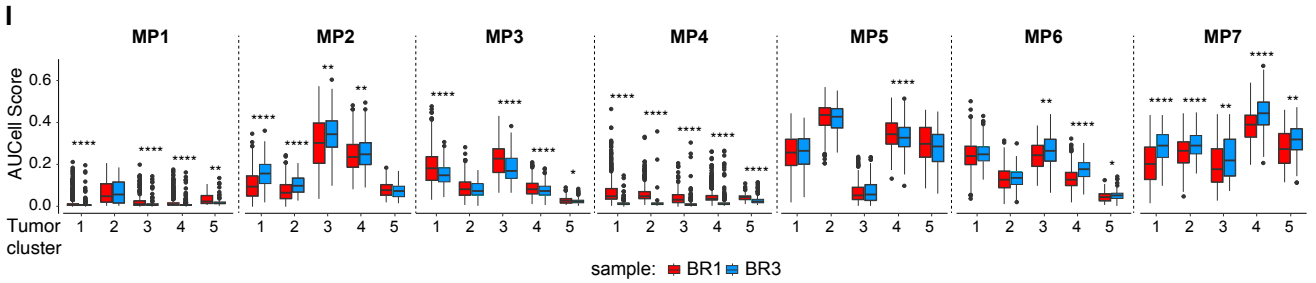

Figure 5. BR1 and BR3 tumor cells differentially express molecular programs that are present in human BrM tumor cells.

scRNA-seq analysis of tumor cells from untreated BR1 and BR3 brains. (A) GSEA showing selected GO, KEGG and REACTOME pathways enriched among the BR1-specific and BR3-specific genes (see Methods). (B) Metascape-associated pathways for BrM metaprograms (MP) identified in BR1 and BR3 tumor cells. (C) Per cell basis analysis of MP activity per group. (D) Correlation-based network analysis between mouse MPs derived in our study (green circles) and human MPs from Biermann et al. 2022 (brown rectangles), using three patient cohorts. Edge thickness and color represent the number of cohorts in which each MP pair is correlated. (E) Spearman correlation between mouse versus human MPs activities in the indicated data sets. x- and y-axis depict spearman correlation coefficient values (F) UMAP projection of tumor cells based on Z-scores of MP activities showing BR1 (red) and BR3 (blue) cell distribution (left) and tumor clusters distribution (right). (G) Proportion of tumor clusters per group. (H) Heatmap depicting Z-score of MP mean activity across malignant cells in each cluster (columns). (I) Per cell basis analysis of MP activity within each cluster from each group. A-C and F-I n = 2-3/group, D-E n = 2-3 mouse/group (our study), n= 25 (Biermann et. al), n=14 (Smalley et. al), n=27 (Alvarez-Breckenridge et. al). See also Figure S5 and Table S5. *$p < 0.05$, **$p < 0.01$, ***$p < 0.001$, ****$p < 0.0001$.

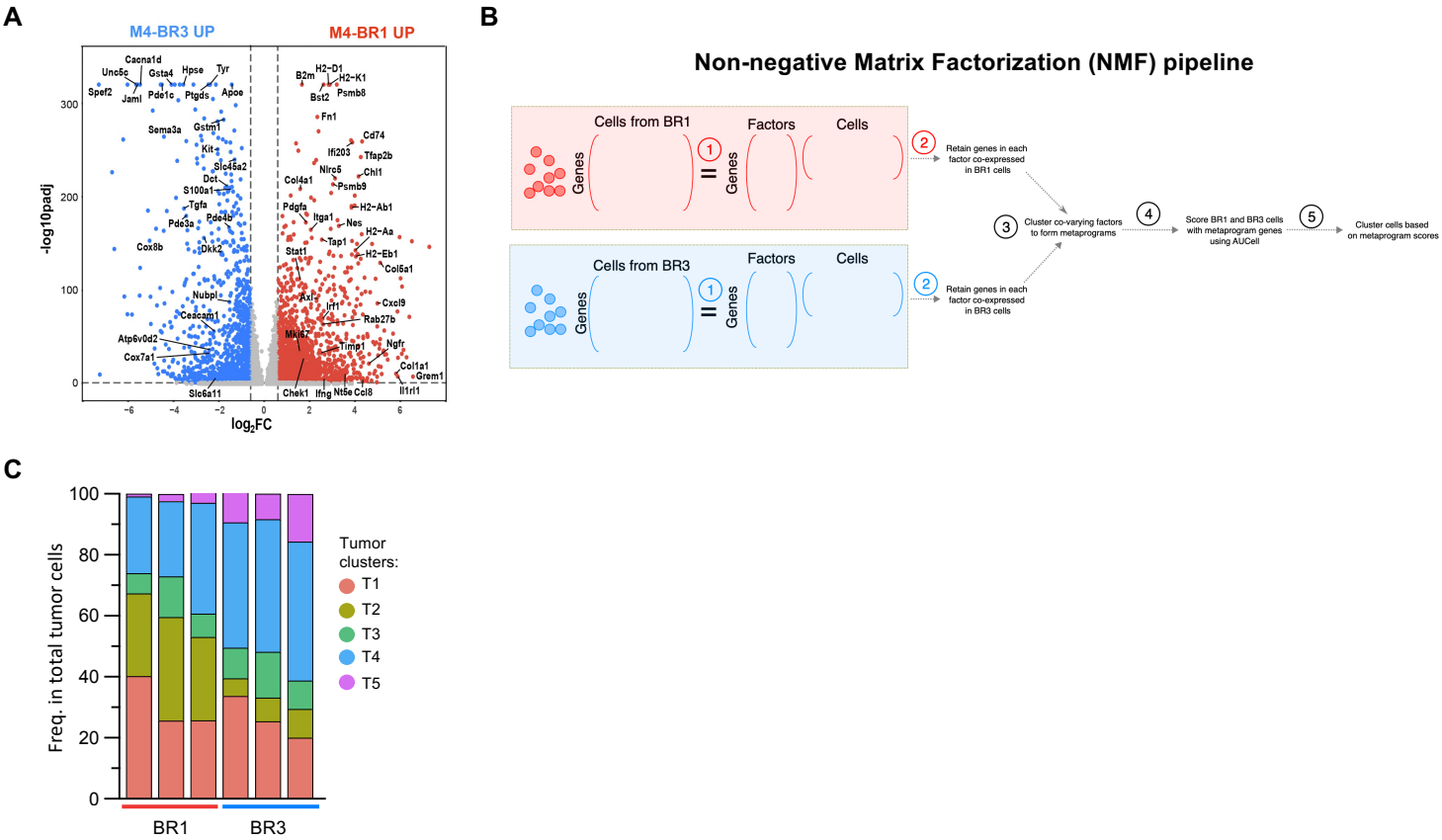
A
M4-BR3 UP
M4-BR1 UP
-log10padj
log2FC
B
Non-negative Matrix Factorization (NMF) pipeline
Cells from BR1
Factors
Cells
Genes
Retain genes in each factor co-expressed in BR1 cells
Cells from BR3
Retain genes in each factor co-expressed in BR3 cells
Cluster co-varying factors to form metaprograms
Score BR1 and BR3 cells with metaprogram genes using AUCell
Cluster cells based on metaprogram scores
C
Freq. in total tumor cells
Tumor clusters:
T1
T2
T3
T4
T5
BR1
BR3

Figure S5. BR1 and BR3 tumor cell molecular characterization by scRNA-seq, related to Figure 5.

scRNA-seq analysis of tumor cells from untreated BR1 and BR3 brains. (A) Volcano plot of BR1 versus BR3 differentially expressed genes. (B) Schematic of metaprogram discovery and their use in clustering malignant cells in BR1 and BR3 models. Step 1: NMF is carried out (k = 30 factors) separately in malignant cells from BR1 and BR3 models based on genes that are expressed in at least 1% of cells in either model. Step 2: Genes with a high weight in each factor are then filtered to retain genes that are co-expressed. Step 3: The activity of each filtered factor is computed across all malignant cells using AUCell. A correlation matrix between all pairs of factors is computed based on these activities, and after hierarchical clustering, correlated factors are grouped together. Genes occurring in at least 25% of constituent factors in a group are retained to form metaprograms. Step 4: AUCell is used to compute the activity of all metaprograms across all malignant cells. Step 5: Cluster cells using Louvain clustering based on metaprogram activity scores. (C) Proportion per sample of indicated tumor clusters. A-C n = 2-3/group. See also Table S5.

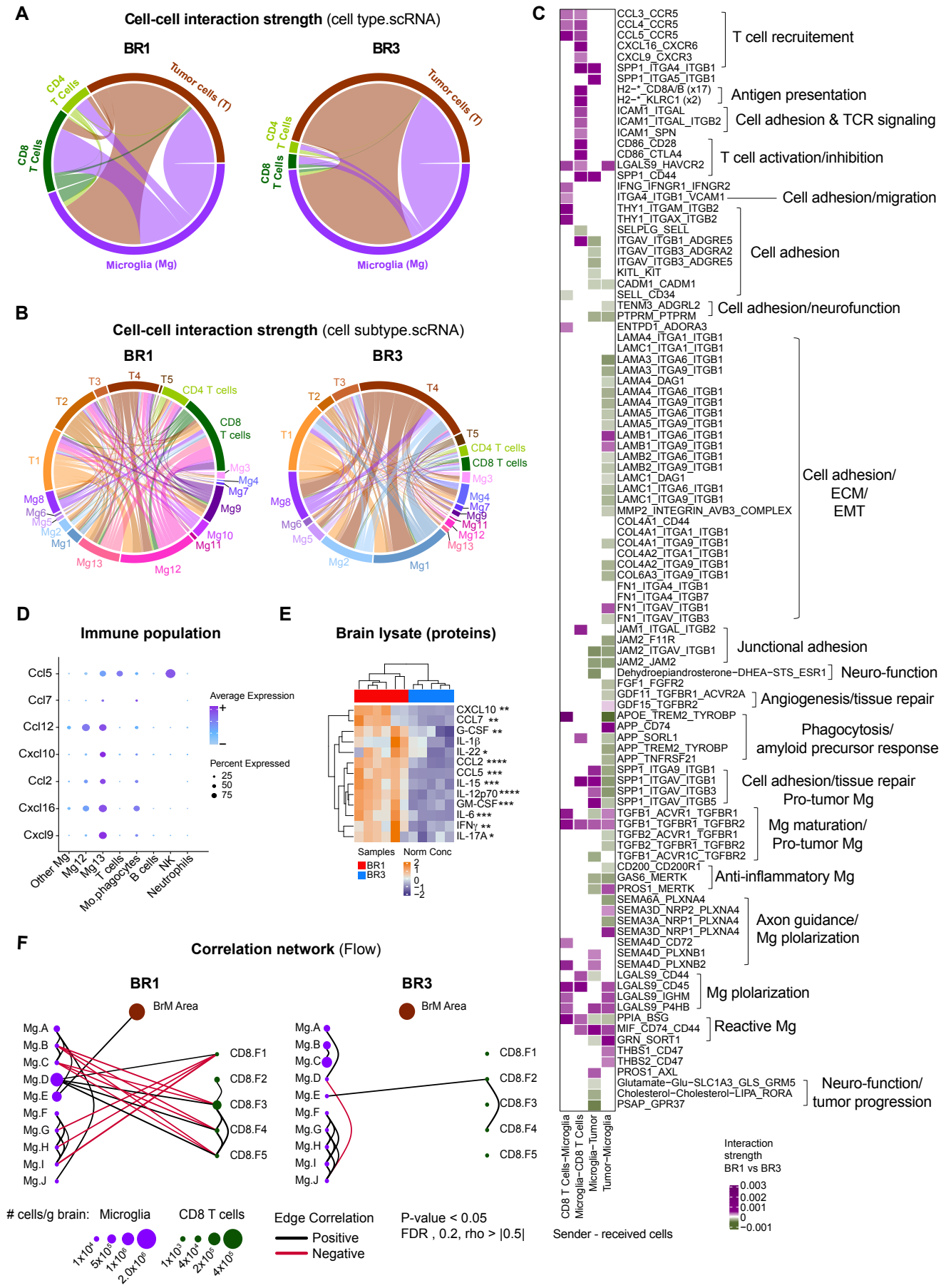
A
Cell-cell interaction strength (cell type.scRNA)
BR1
BR3
Tumor cells (T)
CD4 T Cells
CD8 T Cells
Microglia (Mg)
B
Cell-cell interaction strength (cell subtype.scRNA)
BR1
BR3
T1
T2
T3
T4
T5
CD4 T cells
CD8 T cells
Mg1
Mg2
Mg3
Mg4
Mg5
Mg6
Mg7
Mg8
Mg9
Mg10
Mg11
Mg12
Mg13
C
T cell recruitement
Antigen presentation
Cell adhesion & TCR signaling
T cell activation/inhibition
Cell adhesion/migration
Cell adhesion
Cell adhesion/neurofunction
Cell adhesion/ ECM/ EMT
Junctional adhesion
Neuro-function
Angiogenesis/tissue repair
Phagocytosis/ amyloid precursor response
Cell adhesion/tissue repair Pro-tumor Mg
Mg maturation/ Pro-tumor Mg
Anti-inflammatory Mg
Axon guidance/ Mg plolarization
Mg plolarization
Reactive Mg
Neuro-function/ tumor progression
CD8 T Cells−Microglia
Microglia−CD8 T Cells
Microglia−Tumor
Tumor−Microglia
Sender - received cells
Interaction strength BR1 vs BR3
D
Immune population
Ccl5
Ccl7
Ccl12
Cxcl10
Ccl2
Cxcl16
Cxcl9
Other Mg
Mg12
Mg13
T cells
Mo.phagocytes
B cells
NK
Neutrophils
Average Expression
Percent Expressed
E
Brain lysate (proteins)
CXCL10 **
CCL7 **
G-CSF **
IL-1β
IL-22 *
CCL2 ****
CCL5 ***
IL-15 ***
IL-12p70 ****
GM-CSF ***
IL-6 ***
IFNγ **
IL-17A *
Samples
Norm Conc
BR1
BR3
F
Correlation network (Flow)
BR1
BR3
BrM Area
Mg.A
Mg.B
Mg.C
Mg.D
Mg.E
Mg.F
Mg.G
Mg.H
Mg.I
Mg.J
CD8.F1
CD8.F2
CD8.F3
CD8.F4
CD8.F5
cells/g brain: Microglia
CD8 T cells
Edge Correlation
Positive
Negative
P-value < 0.05
FDR , 0.2, rho > |0.5|

Figure 6: BrM tumor cells dictate the TME differences between ICB-responder BR1 and ICB-resistant BR3.

(A-C) Cell-cell interaction analysis from scRNA-seq data of untreated BR1 and BR3 brains. (A-B) Circos plot showing the overall predicted interaction strength between indicated cell types (A) and indicated clusters within each cell type (B). The outside border color of the circos represent the sender and receiver cell populations. The width of the lines inside the circos plot indicates the interaction strength. The color of the lines inside the circos plot indicates the sender cell population. (C) Heatmap showing the top and bottom 10% most differential interaction (by strength) of ligand-receptor (L-R) pairs between models for indicated cell type pairs (see methods). Interactions stronger in BR1 versus BR3 are depicted in purple, interactions stronger in BR3 depicted in green. Numbers in parentheses indicate the number of different L-R pairs. No number indicates that only one L-R pair is present. (D) Dot plot showing the expression of selected chemokines in each immune cell population. (E) Cytokine/chemokine protein profile (normalized measurement) from untreated BR1 and BR3 whole brain lysates. (F) Correlation-based network analysis of total brain metastatic area (BrM area; determined by machine learning algorithm), microglia (Mg.A – Mg.J) and $CD8^+$ T cell (CD8.F1 – CD8.F5) cluster cell count per gram of brain (quantified by spectral high-parametric flow cytometry analysis) from untreated BR1 and BR3 brains. Lines represent spearman correlations. A-D n = 2-3/group, E n = 5-6/group, K n = 8-10/group/experiment. *$p < 0.05$, **$p < 0.01$, ***$p < 0.001$, ****$p < 0.0001$. See also Figure S6.

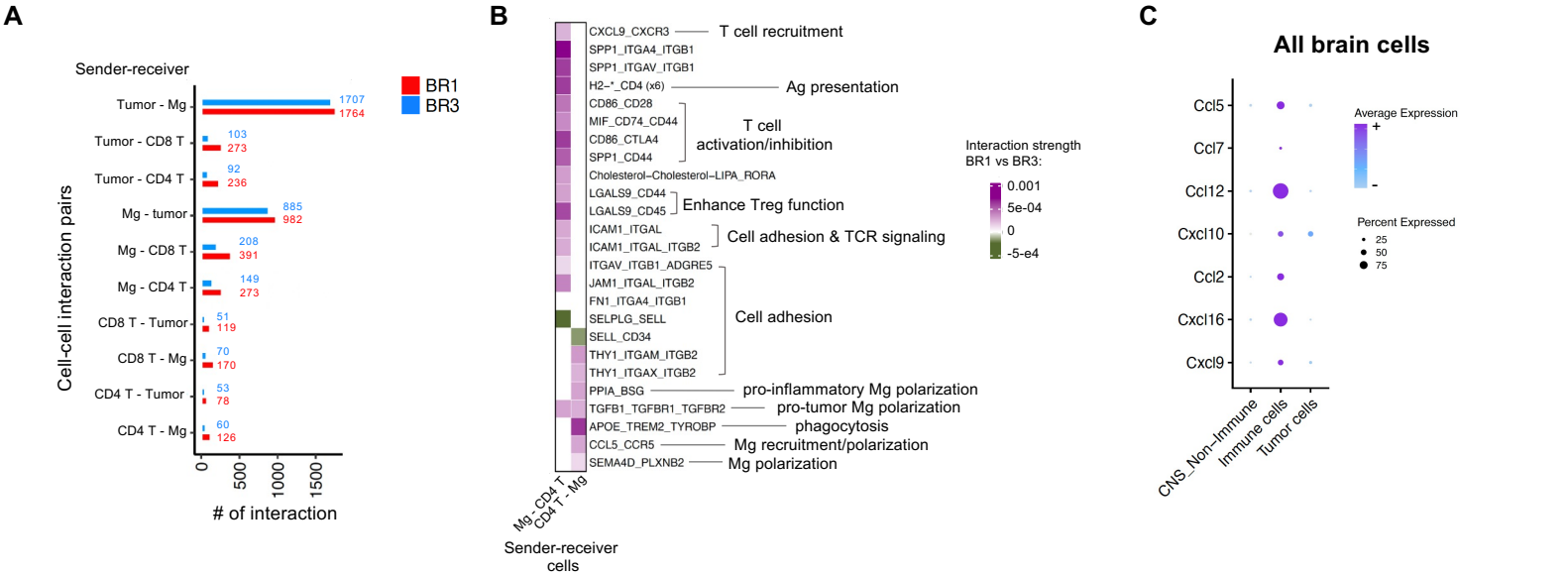

D

Human CD8 T cell clusters	Selected genes	Similar mouse CD8 T cell clusters*
0	*HAVCR2,LAG3,PRF1, ENTPD1*	**CD8.sc5** (“activated/exhausted”)
1	*ENTPD1,TOX,TCF7, CXCL13*	**CD8.sc4** (“exhausted stem cell-like”)
2	*PDCD1, GZMA, PRF1, ITGAE*	NA
3	*LAG3,TCF7*	**CD8.sc4** (“exhausted stem cell-like”)
4	*HAVCR2,LAG3,TIGIT, CTLA4, IFNG, TOX, ENTPD1*	**CD8.sc5** (“activated/exhausted”)
5	*SELL, CCR7, IL7R, TCF7, GZMK, GZMB, GZMA*	**Mix CD8.sc1 and CD8.sc3** (“naïve” and “effector memory”)
6	*MKI67,CDK1*	**CD8.sc6** (“proliferative”)
7	*MKI67,CDK1, ENTPD1*	**CD8.sc6** (“proliferative”)
8	*MKI67, CTLA4, GZMA, GZMK,GZMB, PRF1*	**CD8.sc6** (“proliferative”)

*Enriched in **BR1** or **BR3**

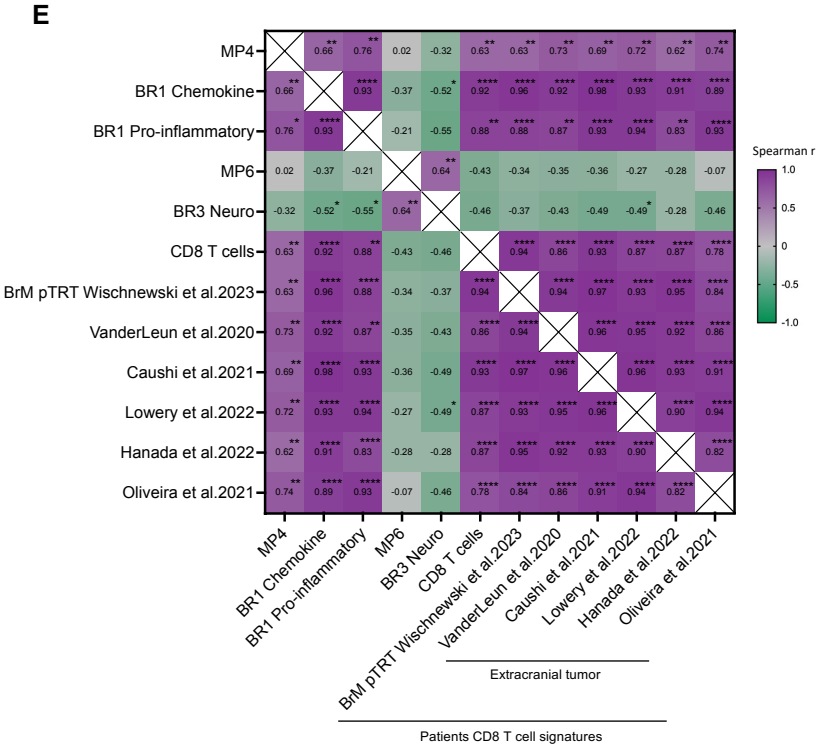

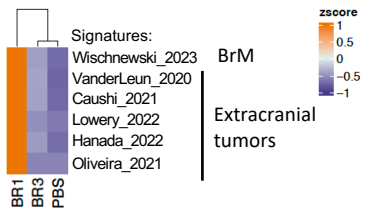

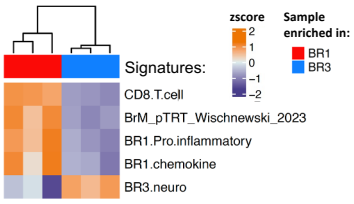

Figure S6: BR1 and BR3 tumor molecular features control the BrTME.

(A-B) Cell-cell interaction analysis from scRNA-seq data of untreated BR1 and BR3 brains. (A) Total number of interactions between indicated cell sender-cell receiver pairs per group. (B) Heatmap showing the top and bottom 10% most differential interaction strength of ligand-receptor (L-R) pairs between BR1 versus BR3 (see methods) for each indicated cell type pair. Interactions stronger in BR1 versus BR3 are depicted in purple, interactions stronger in BR3 depicted in green. Numbers in parentheses indicate the number of different L-R pairs. No number indicates that only one L-R pair is present. (C) scRNA-seq analysis of all brain cells from untreated BR1 and BR3-bearing mice. Dot plot showing the expression of selected chemokines in each cell type. (D) Human $CD8^+$ T cell clusters identified in Biermann et al. 2022 dataset with their selected expressed genes and similar mouse $CD8^+$ T cell clusters from BR1 and BR3 models. (E) Pseudobulk RNA-seq analysis of Sun et al. 2023 pan-cancer BrM patient cohort. Spearman correlation matrix between the different BR1 and BR3 signatures in patient biopsies. See also Table S6. (F) scRNA-seq analysis of total $CD8^+$ T cells from BR1, BR3, and non-tumor (PBS) bearing mice. Heatmap showing Z-score expression level of various published gene signatures described as "tumor-reactive" CD8 T cells in cancer patients. See supplementary table S8 for details. (G) Pseudobulk RNA-seq analysis of BR1 and BR3-bearing brains. Heatmap showing Z-score expression of $CD8^+$ T cells, BR1, and BR3 signatures among total brain cells across samples. A-C, F-G n = 2-3/group. D n= 10 patients. E n=17 patients. *$p < 0.05$, **$p < 0.01$, ***$p < 0.001$, ****$p < 0.0001$. See also Table S6.

Daugherty-Lopès et al. Fig7

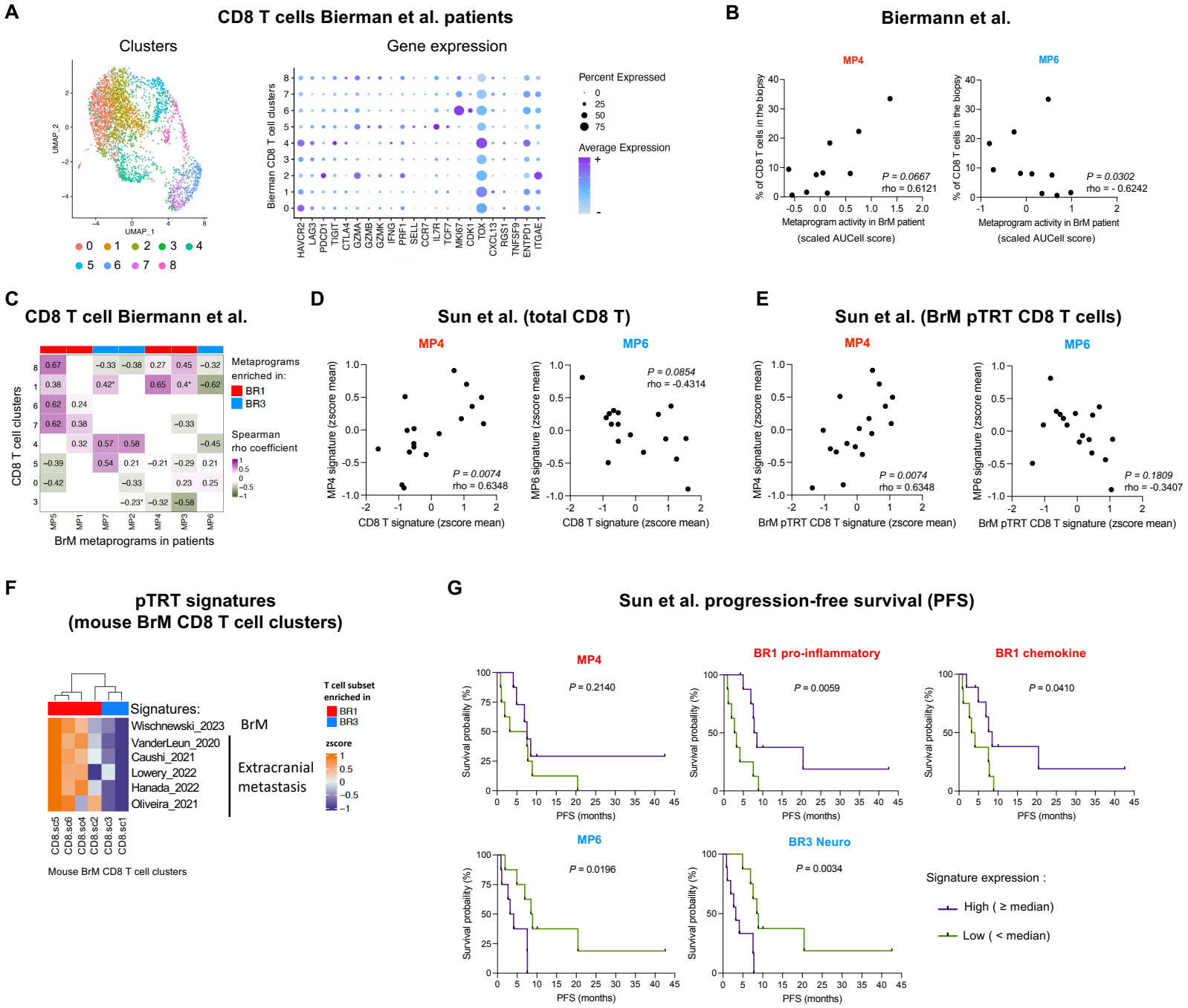

Figure 7. BR1 and BR3 signatures are associated with BrM patient CD8$^+$ T cell infiltration and survival.

(A-C) scRNA-seq analysis of CD8$^+$ T cells from Biermann et al. 2022 untreated melanoma BrM patient biopsies. (A) UMAP projection and clustering (left). Dot plot showing the expression of selected differentially expressed T cell markers (right). (B) Spearman correlation of MP4 (BR1-MP) or MP6 (BR3-MP) activity and CD8$^+$ T cell percentage among total cells per sample within each biopsy. (C) Heatmap representing spearman correlations between proportion (% of total cells) of individual CD8$^+$ T cell clusters (row) and the indicated MP activity (column) within each biopsy. (D-E) Pseudobulk RNA-seq analysis of untreated and treated patient pan-cancer BrM biopsies from Sun et al. 2023. Spearman correlations of the indicated signatures' expression (see methods). (F) Expression of "tumor-reactive" human CD8 T cell signatures defined by the indicated studies (row) within each mouse CD8$^+$ T cell cluster from our study (column). Heatmap depicts Z-score expression across rows. (G) Progression-free survival of BrM patients stratified by median expression of the indicated signatures. BR1 and BR3 signatures are indicated in red and blue respectively. A-C n= 10 patients. D-E, G n=17 patients. F n = 2-3/group. See also Figure S6 and Tables S5-S6.

RESOURCE AVAILABILITY

Lead contact

Further information and requests for resources and reagents should be directed to and will be fulfilled by the lead contact, Romina S. Goldszmid (rgoldszmid@mail.nih.gov).

Materials availability

Cell lines generated in this study will be made available from the lead contact (R.S.G) and/or G.M, C-P. D., E.P.-G. upon request but may require a completed NIH Materials Transfer Agreement.

Data and code availability

Single-cell RNA-seq and whole exosome sequencing data generated by this study will be deposited at GEO and made publicly available as of the date of publication. This paper also analyzes existing, publicly available data. All accession numbers will be listed in the key resources table and method section. Any additional information required to reanalyze the data reported in this paper is available from the lead contact upon request.

EXPERIMENTAL MODEL AND STUDY PARTICIPANT DETAILS

Animals

All animal studies were approved by the Institutional Animal Care and Use Committee of National Cancer Institute and were conducted in accordance with the IACUC guidelines at the National Institutes of Health Guide for the Care and Use of Laboratory Animals. C57BL6/NCr female mice were obtained from Charles River Laboratories (CRL) and were group-housed with up to 5 mice per cage, in a specific pathogen-free environment in the Center for Cancer Research (CCR) animal facility at the NCI Bethesda or the NCI Frederick. In both facilities, mice were housed under standard conditions with *ad libitum* access to food and water and under a 12/12h light/dark cycle. In all studies, 6-8 weeks-old mice were used. For experiments in which brain metastatic untreated mice were compared, the mice distribution per group was randomized to obtain similar weight per group, as weight can impact the success of the tumor implantation by intracardiac injection. Additional randomization was performed for brain metastatic therapy studies after tumor implantation but before the administration of the immunotherapy, considering the order of injection, as this factor might also influence tumor implantation.

Cell lines

M4-BR1 (BR1) and M4-BR3 (BR3) brain metastatic cell lines were generated by intracardiac (i.c.) injection of $5x10^5$ M4-B2905 (M4) cells, which originated in a hepatocyte growth factor (Hgf^{tg})

transgenic C57BL/6J male mouse as described before[27]. Successive *in-vivo* selection for homing to the brain was done for one (BR1) or three (BR3) cycles. Briefly, brains from 5-10 mice i.c. implanted were cut separately in small pieces and homogenized in 0.25% trypsin (Gibco #25200056) for less than 10 min. Whole brain homogenates were plated and maintained in culture for 2 weeks or until expanded in enough cell numbers. Successful cultures were harvested and injected i.c. again to repeat the cycle.

M4 cell line was cultured in RPMI medium supplemented with 10% FBS and 1% l-Glutamine (200 mM); BR1 and BR3 melanoma cell lines were cultured in high glucose, GlutaMAX™ supplement, HEPES DMEM medium (Gibco #10564011) supplemented with 10% heat inactivated FBS at 37°C, 5% CO_2 in air atmosphere. All cells were tested and found negative for specific mouse pathogens (MTBM test) and were confirmed as Mycoplasma negative using a Mycoplasma detection kit (Lonza, LT07-418).

Publicly available patient dataset

The single-cell read-count matrix of the single-cell RNA-sequencing (scRNA-seq) dataset from BrM patient biopsies used in this manuscript were downloaded from Gene Expression Omnibus (GEO): Smalley et al. 2021 (GSE174401) 14 melanoma patients untreated or treated with immune-checkpoint blockade (ICB) and/or targeted therapy, and/or radiotherapy (RT); Sun et al. 2023 (GSE193745), 17 pan-cancer patients untreated or treated with ICB and/or targeted therapies and/or RT. Alvarez-Breckenridge et al. 2023, was downloaded from Broad Single Cell Portal (SCP1493) and composed of 27 melanoma patients untreated or treated with ICB and/or targeted therapies and/or RT. Biermann et al. 2022 (GSE200218), single-nucleus RNA-seq from 25 untreated melanoma patients (15 BrM biopsies and 10 extra-BrM biospies) were downloaded from GEO.

Experimental brain metastasis

C57BL/6J mice were shaved at the chest and intracardially (i.c.) injected with $5x10^5$ BR1 cells or $7.5x10^4$ BR3 cells per mouse. Animals were kept under anesthesia (2-3% isoflurane in oxygen) and continuous monitoring during the whole procedure. The endpoint of the model was set when the animal weight loss reached 5% of the initial weight and/or any behavior changes were observed such as shortness of breath or slow motion, and was reached around 18-20 days after i.c. injection. When, in some rare cases, animals did not show any brain metastasis implantation at endpoint, they were excluded from the study.

Immune checkpoint inhibitor treatment

To test and compare ICB monotherapy and combination efficacy between the models we implanted BR1 and BR3 cells by ultrasound-guided intracardiac injection. Mice were treated with monotherapy anti-CTLA-4 (BioXcell, BP0164) and anti-gp120 IgG1 isotype control (BioXcell, BE0154), or anti-PD-L1 (Genentech, clone 6E11) and anti-IgG2b isotype control (BioXcell, BP0086), or anti-CTLA-4 and anti-PD-L1 combination therapy, or a mix of anti-gp120 IgG1 and anti-IgG2b isotype control, or with PBS as a supplementary control. Anti-CTLA-4 and anti-IgG2b antibodies were administered twice per week for a total of 4 doses. The first dose was administered intravenously (IV) at 200mg per mouse, and the following 3 doses were administered intraperitoneally (IP) at 200mg per mouse. Anti-PD-L1 and anti-gp120 IgG1 antibodies were administered twice per week for a total of 5 doses. The first dose was administered intravenously (IV) at 200mg per mouse, and the following 4 doses were administered intraperitoneally (IP) at 100mg per mouse. Depending on the studies this treatment regimen started 3 days or 7 days post-tumor implantation.

Tissue collection

Mice were euthanized in CO_2 chambers following the American Veterinary Medical Association (AVMA) guidelines at endpoint or as indicated for kinetic studies (4, 8 or 12 days after ic. injection). Mice were then intracardially perfused with 20 mL of ice-cold 1X PBS supplemented with 2 mM EDTA. Lungs, thymus, livers, kidneys, adrenal glands, digestive and reproductive ducts were harvested, fixed for 24h in 10% formalin at room temperature, and then kept in ethanol 70% at room temperature until metastasis quantification. Brains were harvested, immediately imaged using a stereomicroscope, and prepared for immunohistochemistry, immunophenotyping, or single-cell RNA-sequencing (scRNA-seq) experiments.

Microscopy imaging

Macroscopic whole-brain pictures were acquired using a Leica M165 FC stereomicroscope (LEICA, USA) equipped with a Leica LED5000 ring light illumination (RL-80/40) and a digital color FLEXACAM C1 camera, as previously described[30]. Briefly, two pictures per brain were acquired: the whole ventral surface and the whole dorsal surface, at 4X magnification using the camera set on brightfield. Pictures focusing on individual brain metastases were acquired using the same microscopic platform and settings but at 12.5X magnification. All images were acquired with the Leica Application Suite X (LAS X) software, version 5.1.0.

Metastasis burden quantification

Extracranial metastasis burden was assessed by manual counting on fresh organs using a SMZ745T Nikon (Nikon, USA) stereomicroscope trinocular system at 2-4X magnification range. Brain metastasis burden was assessed using a machine learning algorithm that we developed to detect, count and measure size of each metastatic lesions and total metastatic area on whole brain LEICA stereomicroscope pictures, as previously described[30] using the software QuPath[116].

Colony formation assay

BR1, BR3-BrM bearing, and PBS (non-tumor bearing controls) brains were harvested at 4 days post-i.c. injection (as described above) and were processed using Adult Brain Dissociation Kit (Miltenyi, #130-107-677) following the manufacturer's instruction. Each single cell suspension obtained were seeded in duplicate in 6-well plates and cultured in high glucose, GlutaMAX™ supplement, HEPES DMEM medium (Gibco #10564011) supplemented with 10% heat inactivated FBS and 50 mg/mL of gentamicin, at 37°C, 5% CO_2 in air atmosphere. Media was renewed and dead cell remove every 2 days. After 10 days, the cells were washed with 1X PBS, fixed for 5 min at room temperature in ice cold methanol (VWR Chemicals, 85800.290P), washed with 1X PBS and then stained with a 2.3% crystal violet solution (Sigma-Aldrich, HT90132). After removing the excess stain, the cells were washed in molecular biology water (Vita scientific, 351-029-101) and the well were air-dried overnight at room temperature and protected from light. The wells were then imaged using a Nikon D90 camera (Nikon, USA).

Histology and immunohistochemistry

Formalin-fixed and paraffin-embedded 5µm sagittal or longitudinal sections of brains from BR1 or BR3 BrM-bearing mice or injected with PBS as non-BrM control were stained with hematoxylin and eosin (HE) or DCT (Pep8h58[117]) antibody using standard immunohistochemistry methods. Antigen retrieval was performed at 95ºC for 20 minutes in a pressure cooker using target retrieval buffer pH6 (Dako, S1699). Protein Blocking reagent (Dako, X0909) and Bloxall blocking solution (Vector, SP-6000-100) were used to block nonspecific proteins and endogenous peroxidase and alkaline phosphatase activities following provider recommendations. DCT antibody (dilution 1:5000) was incubated overnight at 4˚C in a humidity chamber. Antibody detection was performed using Impress AP Reagent anti-rabbit Ig (Vector, MP-5401) and ImPACT Vector Red (Vector, SK-5105) following provider protocol. Slides were counterstained with Mayer's Hematoxylin (Electron Microscopy Sciences, 26043-06) and GIEMSA (New Comer Supply, 1120A) for 2-5 minutes each at. Whole slides

were scanned using an AT2 Leica scanner (Leica, USA) at 20X magnification and digital image files were visualized using HALO link (Indica labs).

Whole exome sequencing of brain metastatic cell lines

Mouse genomic DNA concentration was measured using Quant-iT PicoGreen dsDNA Assay Kit (Thermofisher scientific, P11496). 200ng of DNA was sheared by Covaris Instrument (E210) to ~150-200bp fragments. Shearing was done in a Covaris snap cap tube (microTUBE Covaris p/n 520045) with the following parameters: duty cycle, 10%; intensity, 5; cycle burst, 200; time, 360 seconds at 4°C. Samples quality assessment/size was validated by Bioanalyzer DNA-High sensitivity kit (Agilent # 5067-4626).

Agilent SureSelectXT library prep ILM Kit (Agilent Technologies, #G9611A) was used to prepare the library for each sheared mouse DNA sample. DNA fragment's ends were repaired, followed by Adenylation of the 3' end and then ligation of paired-end adaptor. Adaptor-ligated libraries were then amplified (Pre-capture PCR amplification: 98°C 2 minutes, 10 cycles; 98°C 30 seconds; 65°C 30 seconds; 72°C 1 minute; then 72°C 10 minutes, 4°C hold) by Herculase II fusion enzyme (Agilent Technologies, #600679). After each step DNA was purified by Ampure XP beads (Beckmann Coulter Genomics #A63882). DNA Lo Bind Tubes, 1.5mL PCR clean (Eppendorf # 022431021) or 96 well plates were used to process the samples.

Samples were analyzed by bioanalyzer using DNA-1000 kit (Agilent #5067-1504). Concentration of each library was determined by integrating under the peak of approximately 225-275bp. Then each gDNA library (~750-1000ng) was hybridized with biotinylated mouse specific capture RNA baits (SureSelectXT Mouse All Exon, catalog #5190-4641, 16 reactions) in the presence of blocking oligonucleotides. Hybridization was done at 65°C for 16 hours using SureSelectXT kit reagents. Bait-target hybrids were captured by streptavidin-coated magnetic beads (Dynabeads MyOne Streptavidin T1, Life Technologies, #6560) for 30 minutes at room temperature. Then after a series of washes to remove the non-specifically bound DNA, the captured library was eluted in nuclease free water and half volume was amplified with individual index (Post-capture PCR amplification: 98°C 2 minutes; 10 cycles of 98°C 30 seconds; 57°C 30 seconds; 72°C 1 minute; 72°C 10 minutes, 4°C hold). The Bioanalyzer High sensitivity kit was used to validate the size of the libraries prior to sequencing. The libraries were sequenced in a NovaSeq S2-300 chip.

Single nucleotide variant (SNV) analysis

Fastq sequence reads were mapped to the mouse reference genome mm10 (https://www.ncbi.nlm.nih.gov/datasets/genome/GCF_000001635.20) with BWA or Bowtie. Single nucleotide variants (SNV) were identified using samtools mpileup or GATK HaplotypeCaller. Mouse germline single nucleotide polymorphisms (SNPs) were filtered out using the Sanger Mouse Genomes Project database for variants identified from whole genome sequencing of 36 mouse strains (ftp://ftp-mouse.sanger.ac.uk/current_snps/mgp.v5.merged.snps_all.dbSNP142.vcf.gz). Variants with a Phred-scaled quality score of <30 were removed. Variants that are present in normal spleen samples (in-house collection) were also removed. Variants were annotated with Annovar software to identify non-synonymous mutations. All analyses were carried out on NIH biowulf2 high performance computing environment. Statistical analysis was carried out in R environment.

For pathway analysis of the genes mutated in each cell line we used Ingenuity Pathway Analysis (QIAGEN Digital Insights). For comparison with human BrM we selected 21 genes involved in MAPK and PI3K/mTOR pathways that were mutated in at least one of the BR cell lines and retrieved mutation data from cBioportal (https://www.cbioportal.org/). We used MSK MetTropism data set[31] selecting the samples from metastatic cutaneous melanoma patients and sorted the data in three groups: 1) brain metastases (BrM), 2) all other extracranial metastases, and 3) primary melanomas from patients with BrM. The heatmaps were generated using R package Ggplot2.

Flow cytometry on leukocytes

For immunophenotyping experiments, freshly harvested brains were processed to obtain single-cell suspension following a previously described protocol[118] with some adaptations. Briefly, whole brain tissues were mechanically disrupted using a dounce homogenizer in plain RPMI media. Brain leukocytes were enriched by a 70%/30% Percoll gradient centrifugation and then washed in 10 mL of 1X PBS. After centrifugation. Single cell suspensions were resuspended in 1X PBS and stained with LIVE/DEAD™ Fixable Dead Cell Stain Kit (Invitrogen). FC receptors were blocked with anti-CD16/32 antibody (2.4G2, BioXcell) and the cell suspensions were successively stained in Brilliant Stain Buffer (BD Biosciences) with one or a combination of the following anti-mouse antibodies: Ly6G (1A8, BD Biosciences) , P2RY12 (S16007D, Biolegend), Sirpα (P84, BD Biosciences), CD86 (GL1, BD Biosciences), CD4 (GK1.5, BD Biosciences), CD45.2 (104, BD Biosciences), CD11b (M1/70, BD Biosciences), CX3CR1 (SA011F12, Biolegend), CD8α (MCD0826, ThermoFisher scientific), Arg1 (A1exF5, ThermoFisher scientific), MHCII (M5/114.15.2, BD Biosciences), CD103 (M290, BD Biosciences), CD62L (MEL-14, Biolegend), PD-1 (J43, BD Biosciences), CD24 (M1/69,

BD Biosciences), PD-L1 (MIH5, BD Biosciences), SiglecH (440C, BD Biosciences), CD64 (X54-5/7.1, BD Biosciences), TMEM119 (106-6, abcam), CD3 (17A2, Biolegend), CD68 (FA-11, Biolegend), CD49d (9C10, BD Biosciences), LAG3 (ebioC9B7W, Invitrogen), CD44 (IM7, Biolegend), FOXP3 (FJK.16s, Invitrogen), CD69 (H1.2F3, Biolegend), CD25 (PC1, Biolegend), NK1.1 (PK136, Biolegend), CD11c (N418, ThermoFisher scientific), CD39 (Duha59, Biolegend), MertK (DS5MMER, ThermoFisher scientific), Tim3 (RMT4-54, BD Biosciences), F4/80 (BM8, Invitrogen), Ly6C (AL-21, BD Biosciences), CD52 (4C8, BD Biosciences), CD19 (6D5, Biolegend). When unlabeled primary rabbit antibodies or biotinylated antibodies were used, cells were subsequently incubated with anti-rabbit IgG antibodies or fluorochrome-conjugated streptavidin. For intracellular staining, the cell suspension was fixed and permeabilized with the eBioscience™ FOXP3/Transcription Factor Staining Buffer Set (eBioscience) after the cell surface staining, following the manufacturer's instruction.

The cell suspension was then filtered through a 40 µm filter and each sample was acquired using the spectral flow cytometer Cytek® Aurora (5 lasers, 5L UV-V-B-YG-R) and the SpectroFlo® software (v.3.3.0) (Cytek® Biosciences). For data analysis initial gating strategy were performed as previously described[119] with FlowJo software (v.10.10.0): (1) FSC-A versus SSC-A to exclude debris; (2) FSC-A versus FSC-H to select singlet; (3) SSC-A versus Live/Dead for dead cell exclusion; (4) SSC-A versus CD45 to select $CD45^+$ leukocytes. They were then followed by unsupervised high parametric analysis using Spectre package[120] (v.1.0.0) in R (v.4.2.1). Uniform Manifold Approximation and Projection (UMAP) and density UMAP was run with a concatenation of all samples per group simultaneously. For cluster analysis, Rphenograph was selected (k = 25-45) and the clusters were annotated based on expression level of the markers of interest. Cell populations were defined as indicated in Supplementary Table S2. Frequencies of total leukocytes and subpopulations were determined using FlowJo and Spectre respectively and total leukocytes and subpopulation absolute numbers per g of brain were calculated. Principal component analysis (PCA) was performed in R using the singular value decomposition and visualized using GraphPadPrism (v.10.2.3). Spearman correlation network between CD8 T cell subsets, microglia subsets, and brain metastatic area were calculated within each group using the R package Hmisc_5.1.0 and multiple hypothesis correction was performed using FDR. Correlations that passed p-value < 0.05, FDR < 0.2, spearman rho > |0.5| were visualized using the R package igraph_1.5.1.

Single-cell RNA sequencing (scRNAseq) of mouse BrM

- **Brain dissociation, cell capture and sequencing**

Single cell suspension from BR1 or BR3-BrM bearing or PBS (non-implanted controls) brains were obtained using Adult Brain Dissociation Kit (Miltenyi, #130-107-677) following manufacturer's protocol. Library preparation, captures and sequencing were performed by Single Cell Analysis Facility (SCAF, CCR, NCI). The sample concentration and viability were assessed using the LunaFx7 fluorescent cell counter. The cellular samples were loaded in the lanes according to the 10X Genomics 3' v3.1 Single Cell User Guide with a single capture lane per sample targeting recovery of up to 6,000 cells per lane. Cell partitioning completed successfully with uniform emulsion consistency and the reverse transcription PCR was run overnight. All subsequent steps and quality control was performed as described in the 10X Genomics 3' v3.1 Single Cell User Guide. Two NovaSeq runs for GEX were performed: NovaSeq 2k S1 100-cycle and NovaSeq 6k S1 100-cycle.

- **scRNA-seq data preprocessing (10x chromium single cell 3' v3) and analysis**

10x Genomics Cell Ranger (v.7.0.1) was used to perform demultiplexing, alignment to mouse reference mm10 (refdata-gex-mm10-2020-A), gene and transcript quantification. The parameters –include-introns –force-cells were applied in Cell Ranger count step. Seurat (v.4.2.0)[121] was used for preprocessing, normalization and clustering. Genes detected in fewer than 3 cells and cells containing less than 100 genes were removed from the data sets prior to further filtering. Doublets and background cells were filtered based on negative binomial distribution to determine the upper and lower limit of UMI count per cell (9-93,348) and gene count per cell (33-16,472). Mitochondrial percentages in cells were calculated in Seurat, we set up the filtering threshold as 15.46% (median + 4 x median absolute deviation), cells with higher mitochondrial expression than the selected threshold were filtered out. After removing unwanted cells from the dataset, the data was normalized by SCTransform from Seurat. Seurat RunPCA and ElbowPlot were used to find the optimal number of principal components (PCs), Seurat FindClusters function was called to use the first 20 PCs at the resolution of 0.6 and identified 37 distinct cell clusters. Uniform manifold approximation and (UMAP)[122] was used for data visualization in two-dimensional space. These upstream analyses were performed by CCR-SF Bioinformatics Team (NIH-CCR).

Then all downstream analysis were performed using Seurat package (v.5.1.0)[123] in R. Cell type identifications were performed using the reference cell type gene expression databases: Allen brain atlas (https://portal.brain-map.org/), Immgen (https://www.immgen.org/) and PanglaoDB

(https://panglaodb.se/) and the automated annotation algorithm: Azimuth (https://azimuth.hubmapconsortium.org/) and SC_Type[124].

Re-clustering on immune cell subsets was performed using FindNeighbors (dimension 1:30) and FindClusters (resolution 0.5), and visualized using RunUMAP (dimension 1:30). Cluster specific genes were identified using the FindMarkers function with a fold change of > 0.25. Re-clustering for specific downstream immune cell analysis was performed following the same approach. Re-clustering on tumor cells was performed using non-negative matrix (NMF) as described in the next section. For all immune cell analysis, the differentially expressed genes (DEGs) between groups and cluster was performed using the FindMarkers function (p_adj < 0.05 and Avg_Log2FC > 0.25). For volcano plot the thresholds of significance used were: p_adj < 0.05 and Avg_Log2FC > 0.5. For melanoma cells the DEGs between BR1 and BR3 groups were analyzed using MAST (Model-based Analysis of Single-cell Transcriptomics)[65]. Log_2 values of BR1 vs. BR3 fold change of gene expression levels (Log_2FC) and Log_{10} of p values adjusted of t-test ($-Log_{10}$p-value.adj) were analyzed to make the volcano plot. The threshold of significance used is $Log_2FC > 0.6$ and $p < 0.05$. Gene Set Enrichment Analysis (GSEA) (https://www.gsea-msigdb.org/gsea/index.jsp) were then performed and using GO, KEGG and Hallmark for microglia (group comparison and clusters), and using Gene Ontology (GO), Kyoto Encyclopedia of Genes and Genomes (KEGG) and REACTOME datasets for melanoma BrM cells. The top pathways determined by the highest Normalized Enrichment Score (NES) were used to select those represented on the figures.

Non-negative matrix factorization and metaprogram discovery

We retained genes expressed in at least 1% of all malignant cells from both BR1 and BR3 mouse models and ran a fast NMF implementation[67] separately on malignant cells from each model with no L1 or L2 penalty specified. We chose to obtain 30 factors for cells from each mouse model based on the change in reconstruction error of the gene expression matrix as the number of factors was increased. For a given NMF run within BR1 or BR3 models, we prioritized genes that contributed to each factor using a two-step procedure. We first z-scored the loadings of each gene across all factors and for a given factor, retained those genes with z > 1.5. Second, for a given factor, we computed the Spearman correlation coefficient of all gene pairs and used those pairs whose correlation was greater than 0.4 and constructed a gene co-expression graph. The final prioritized gene list (referred to as prioritized genes) consists of only those genes in the largest component of the co-expression graph. Any factor with less than ten prioritized genes is discarded. For each factor, we then use AUCell[125] to score the activity of prioritized genes across malignant cells from both the mouse models and compute the Pearson correlation coefficient between all pairs of factors including both models. We hierarchically

clustered the factors based on the inter-factor correlations and grouped all factors into eight clusters or metaprograms (this number maximized the Silhouette coefficient of the clustering). Within each metaprogram, we only retained those genes that were present in at least 25% of all constituent factors. The metaprograms that were active (based on the Global_k1 AUCell threshold) in less than 10% of cells from each model were discarded. This procedure yielded seven metaprograms spanning the cells in the two mouse models. Each metaprogram functional implication was characterized by pathway analysis using Metascape[71].

Since NMF factorizations are non-unique i.e., can yield different factors when re-run, we repeated the above procedure 100 times. For each run, we trained a logistic regression classifier to distinguish BR1 and BR3 tumor cells (using five-fold cross-validation) based on the metaprograms obtained from the procedure outlined above and computed its area under the ROC (auROC) value. We chose this criterion to ensure that our pipeline to derive metaprograms from an NMF run is able to capture differences between BR1 and BR3 models. The metaprograms derived in this paper were based on the NMF run whose auROC (auROC = 0.927) was the median auROC value amongst all NMF runs.

To cluster all malignant cells, we first scored the activity of these seven metaprograms using AUCell. We then z-scored each metaprogram activity across all cells and constructed a k-nearest neighbor graph (k=30) based on the seven z-scores for each cell. The Mahalanobis distance was used to compute distances between cells for neighborhood graph construction as this distance metric takes into account potential correlations between metaprogram scores. We ran 100 parallel iterations of Louvain clustering (with a resolution of 0.4) on this graph and kept the clustering with the highest Silhouette coefficient (where cell-cell distances were computed using the Mahalanobis distance metric). For visualization, we computed UMAP coordinates of each malignant cell based on the activity across the seven metaprograms.

Correlation analysis of mouse tumor metaprograms with tumor metaprograms derived in Biermann et. al

We used AUCell to compute the activity of our metaprograms as well as metaprograms derived by Biermann et al. 2022 in every malignant cell from Biermann et al. 2022, Smalley et al. 2023, Alvarez-Breckenridge et al. 2023. We then computed the pair-wise Spearman correlation coefficient between every mouse metaprogram and every Biermann et al. 2022 metaprogram across cells in each tumor biopsy. Within a given cohort, the median correlation coefficients computed for a given pair of metaprograms across all tumors was retained for further analyses. A metaprogram pair was considered to be significantly and positively correlated within a cohort if the set of tumor-wise correlations were

significantly above 0.2 (Wilcoxon one-sided p-value < 0.05). We then counted the number of cohorts in which a metaprogram pair were significantly positively correlated and only visualized those that were correlated in at least one cohort.

Cell-cell interaction discovery using Cellchat

We used Cellchat[126] to infer cell-cell communications between microglia, CD4 T cells, CD8 T cells and malignant cells in BR1 and BR3 samples separately. Given the relatively lower numbers of CD4 and CD8 T cells in the data, we grouped all sub-clusters of those two cell types while keeping CD4 and CD8 T cells separated and detected interactions between them and sub-clusters of microglia and up-regulated (p_adj < 0.05) in the sender and receiver cell type, respectively and (b) the ligand and receptor were expressed in at least 10% of cells in the sender and receiver cell type, respectively. Interactions amongst the top 10% most different in strength (which is defined by Cellchat as the product of ligand and receptor expression in sender and receiver cell types and weighted by the proportion of cells in each cell type) between BR1 and BR3 was labelled as either BR1-specific or BR3-specific.

Whole metastatic brain protein expression

Brain hemispheres were mechanically disrupted in 500 µL ProcartaPlex™ cell lysis buffer (ThermoFisher scientific, EPX-99999-000) for every 100mg of tissue, using an Omni Tissue Master 125 Homogenizer (Omni international). Supernatants were extracted and total concentration of protein was measured using the Pierce™ BCA Protein Assay Kit (ThermoFisher scientific, 23227). Samples were diluted to 10 mg/mL protein with PBS and cytokines concentration were measured using the ProcartaPlexTM Mouse Cytokine & Chemokine Panel 1A, 36plex (ThermoFisher scientific, EPX360-26092-901) according to manufacturer's instructions.

Patient single-cell transcriptomic analysis on T cells

The single-cell read-count matrix of Biermann et al. 2022 dataset were processed using Seurat (v4.3.0)[123]. We chose only brain metastatic biopsies and normalized read counts using the NormalizeData function. The 5000 most variable genes were chosen to compute 50 principal components, which were then clustered using the FindClusters function (with a resolution of 0.8). We then subset the data to those clusters with high expression of CD45 for re-analysis. Based on the expression of *CD3D*, *CD3E*, *NCR1*, *CD8A*, *CD8B*, *CD4*, *GZMA*, *GZMB*, *IFNG*, *GZMK*, *PRF1*, *ITGAM*, *ITGAX*, *CD14*, *NCAM1*, *FCGR3A*, *P2RY12*, *HBB*, we separated lymphoid cells from other CD45+ sub-populations. We then retained only those samples from BrM patients (n=15) with at least 50 lymphoid cells (resulting in a set of cells from 10 patients) and carried out batch-correction and

integration in Seurat (using 30 PCs and k.weight = 50). The expression of *HAVCR2*, *LAG3*, *PDCD1*, *TIGIT*, *CTLA4*, *GZMA*, *GZMB*, *GZMK*, *IFNG*, *PRF1*, *SELL*, *CCR7*, *IL7R*, *TCF7*, *MKI67*, *CDK1*, *CD45RO*, *TOX*, *CXCL13*, *RGS1*, *TNFSF9*, *ENTPD1*, *ITGAE* was used to annotate all $CD8^+$ T cell subclusters.

Patient bulk-RNA sequencing and survival analysis

MP4 and MP6 signatures were built using the whole gene lists that define these MPs. "BR1 pro-inflammatory" and "BR1 chemokine" include pro-inflammatory and chemokine, respectively, DEGs and cell-cell interactions enriched in BR1. "BR3 neuro" includes axon guidance BR3 DEGs that were also enriched in this group the interactome analysis. To yield a single gene expression vector for each biopsy in Sun et al. 2023 dataset, bulk RNA expression was calculated per sample by summing counts for all cells using the AggregateExpression function from the R package Seurat[123](v.5.0.1). Counts were normalized per sample using $\log_2$(CPM+0.001). Mouse metaprogram genes were converted to human homologs using R software and the Jackson laboratory database (http://www.informatics.jax.org/downloads/reports/HOM_MouseHumanSequence.rpT); genes without direct homologs or that were not contained in the dataset was omitted from signature calculations as well as genes not found in the Sun et al. human dataset. Z-scores were calculated for genes of interest across all samples and mean z-score for each gene signatures were performed. Spearman correlation between the different z-score signature in patients were performed using GraphPadPrism. For survival analysis: for each signature, patients were separated based on median into High (≥ median) and Low (< median) expression. Log-rank (Mantel-Cox) test was performed to calculate the correlation of the gene signature expression and the patient progression free survival after surgery, and p-value reported using GraphPadPrism.

QUANTIFICATION AND STATISTICAL ANALYSIS

Statistical analysis

Statistical analyses were performed using GraphPadPrism or R. Data were analyzed for normal distribution prior to comparisons. Outliers were detected using ROUT' test and excluded from the analysis. Values are presented as the mean ± SEM; individual values (representing individual samples when non indicated or individual experiment when indicated) are presented as scatterplots with column bar graphs or box plot. Data in pie charts represent mean of samples in group. Statistical significance between two groups was determined by two-tailed unpaired Student's t test (parametric) or Mann-Whitney (non-parametric). For the comparison of multiple groups, comparing different treatment in one unique model, one-way ANOVA followed by Tukey's multiple comparison correction test

(parametric) or Mann-Whitney (non-parametric) followed by Dunn's multiple comparison correction test were used). For the comparison of multiple groups, comparing BR1 and BR3 in untreated and treated conditions, two-way ANOVA followed by Tukey's multiple comparison correction test (parametric) or Mann-Whitney (non-parametric) followed by Dunn's multiple comparison correction test were used. Gene signature z-scores were calculated for bulk/pseudobulk and single-cell RNA expression in R using scale and AddModule (Seurat) functions, respectively. Tumor metaprogram z-scores were calculated as z-score = (activity - mean(activity))/sd(activity).

REFERENCES

1. Sperduto, P.W., Mesko, S., Li, J., Cagney, D., Aizer, A., Lin, N.U., Nesbit, E., Kruser, T.J., Chan, J., Braunstein, S., et al. (2020). Survival in Patients With Brain Metastases: Summary Report on the Updated Diagnosis-Specific Graded Prognostic Assessment and Definition of the Eligibility Quotient. J Clin Oncol *38*, 3773–3784. https://doi.org/10.1200/JCO.20.01255.

2. Bander, E.D., Yuan, M., Carnevale, J.A., Reiner, A.S., Panageas, K.S., Postow, M.A., Tabar, V., and Moss, N.S. (2021). Melanoma brain metastasis presentation, treatment, and outcomes in the age of targeted and immunotherapies. Cancer *127*, 2062–2073. https://doi.org/10.1002/cncr.33459.

3. Long, G.V., Atkinson, V., Lo, S., Sandhu, S., Guminski, A.D., Brown, M.P., Wilmott, J.S., Edwards, J., Gonzalez, M., Scolyer, R.A., et al. (2018). Combination nivolumab and ipilimumab or nivolumab alone in melanoma brain metastases: a multicentre randomised phase 2 study. The Lancet Oncology *19*, 672–681. https://doi.org/10.1016/S1470-2045(18)30139-6.

4. Tawbi, H.A., Forsyth, P.A., Hodi, F.S., Algazi, A.P., Hamid, O., Lao, C.D., Moschos, S.J., Atkins, M.B., Lewis, K., Postow, M.A., et al. (2021). Long-term outcomes of patients with active melanoma brain metastases treated with combination nivolumab plus ipilimumab (CheckMate 204): final results of an open-label, multicentre, phase 2 study. The Lancet Oncology *22*, 1692–1704. https://doi.org/10.1016/S1470-2045(21)00545-3.

5. Tawbi, H.A., Forsyth, P.A., Algazi, A., Hamid, O., Hodi, F.S., Moschos, S.J., Khushalani, N.I., Lewis, K., Lao, C.D., Postow, M.A., et al. (2018). Combined Nivolumab and Ipilimumab in Melanoma Metastatic to the Brain. N Engl J Med *379*, 722–730. https://doi.org/10.1056/NEJMoa1805453.

6. Tawbi, H.A., Forsyth, P.A., Hodi, F.S., Lao, C.D., Moschos, S.J., Hamid, O., Atkins, M.B., Lewis, K., Thomas, R.P., Glaspy, J.A., et al. (2021). Safety and efficacy of the combination of nivolumab plus ipilimumab in patients with melanoma and asymptomatic or symptomatic brain metastases (CheckMate 204). Neuro Oncol *23*, 1961–1973. https://doi.org/10.1093/neuonc/noab094.

7. Brastianos, P.K., Kim, A.E., Giobbie-Hurder, A., Lee, E.Q., Lin, N.U., Overmoyer, B., Wen, P.Y., Nayak, L., Cohen, J.V., Dietrich, J., et al. (2023). Pembrolizumab in brain metastases of diverse histologies: phase 2 trial results. Nat Med *29*, 1728–1737. https://doi.org/10.1038/s41591-023-02392-7.

8. Quail, D.F., and Joyce, J.A. (2017). The Microenvironmental Landscape of Brain Tumors. Cancer Cell *31*, 326–341. https://doi.org/10.1016/j.ccell.2017.02.009.

9. Aili, Y., Maimaitiming, N., Qin, H., Ji, W., Fan, G., Wang, Z., and Wang, Y. (2022). Tumor microenvironment and exosomes in brain metastasis: Molecular mechanisms and clinical application. Front. Oncol. *12*. https://doi.org/10.3389/fonc.2022.983878.

10. Caffarel, M.M., and Braza, M.S. (2022). Microglia and metastases to the central nervous system: victim, ravager, or something else? J Exp Clin Cancer Res *41*, 1–13. https://doi.org/10.1186/s13046-022-02535-7.

11. Arvanitis, C.D., Ferraro, G.B., and Jain, R.K. (2020). The blood–brain barrier and blood–tumour barrier in brain tumours and metastases. Nat Rev Cancer *20*, 26–41. https://doi.org/10.1038/s41568-019-0205-x.

12. Wu, D., Chen, Q., Chen, X., Han, F., Chen, Z., and Wang, Y. (2023). The blood-brain barrier: structure, regulation, and drug delivery. Signal Transduct Target Ther *8*, 217. https://doi.org/10.1038/s41392-023-01481-w.

13. Biermann, J., Melms, J.C., Amin, A.D., Wang, Y., Caprio, L.A., Karz, A., Tagore, S., Barrera, I., Ibarra-Arellano, M.A., Andreatta, M., et al. (2022). Dissecting the treatment-naive ecosystem of human melanoma brain metastasis. Cell *185*, 2591-2608.e30. https://doi.org/10.1016/j.cell.2022.06.007.

14. Fischer, G.M., Jalali, A., Kircher, D.A., Lee, W.-C., McQuade, J.L., Haydu, L.E., Joon, A.Y., Reuben, A., de Macedo, M.P., Carapeto, F.C.L., et al. (2019). Molecular Profiling Reveals Unique Immune and Metabolic Features of Melanoma Brain Metastases. Cancer Discov *9*, 628–645. https://doi.org/10.1158/2159-8290.CD-18-1489.

15. Lusby, R., Carl, S., and Tiwari, V.K. (2024). Integrating single-cell transcriptomics with Artificial Intelligence reveals pan-cancer biomarkers of brain metastasis. bioRxiv, 2024.03.08.584083. https://doi.org/10.1101/2024.03.08.584083.

16. Ikarashi, D., Okimoto, T., Shukuya, T., Onagi, H., Hayashi, T., Sinicropi-Yao, S.L., Amann, J.M., Nakatsura, T., Kitano, S., and Carbone, D.P. (2021). Comparison of Tumor Microenvironments Between Primary Tumors and Brain Metastases in Patients With NSCLC. JTO Clin Res Rep *2*, 100230. https://doi.org/10.1016/j.jtocrr.2021.100230.

17. Friebel, E., Kapolou, K., Unger, S., Núñez, N.G., Utz, S., Rushing, E.J., Regli, L., Weller, M., Greter, M., Tugues, S., et al. (2020). Single-Cell Mapping of Human Brain Cancer Reveals Tumor-Specific Instruction of Tissue-Invading Leukocytes. Cell *181*, 1626-1642.e20. https://doi.org/10.1016/j.cell.2020.04.055.

18. Klemm, F., Maas, R.R., Bowman, R.L., Kornete, M., Soukup, K., Nassiri, S., Brouland, J.-P., Iacobuzio-Donahue, C.A., Brennan, C., Tabar, V., et al. (2020). Interrogation of the Microenvironmental Landscape in Brain Tumors Reveals Disease-Specific Alterations of Immune Cells. Cell *181*, 1643-1660.e17. https://doi.org/10.1016/j.cell.2020.05.007.

19. Wischnewski, V., Maas, R.R., Aruffo, P.G., Soukup, K., Galletti, G., Kornete, M., Galland, S., Fournier, N., Lilja, J., Wirapati, P., et al. (2023). Phenotypic diversity of T cells in human primary and metastatic brain tumors revealed by multiomic interrogation. Nat Cancer *4*, 908–924. https://doi.org/10.1038/s43018-023-00566-3.

20. Gonzalez, H., Mei, W., Robles, I., Hagerling, C., Allen, B.M., Hauge Okholm, T.L., Nanjaraj, A., Verbeek, T., Kalavacherla, S., van Gogh, M., et al. (2022). Cellular architecture of human brain metastases. Cell *185*, 729-745.e20. https://doi.org/10.1016/j.cell.2021.12.043.

21. Sun, L., Kienzler, J.C., Reynoso, J.G., Lee, A., Shiuan, E., Li, S., Kim, J., Ding, L., Monteleone, A.J., Owens, G.C., et al. (2023). Immune checkpoint blockade induces distinct alterations in the microenvironments of primary and metastatic brain tumors. J Clin Invest *133*, e169314. https://doi.org/10.1172/JCI169314.

22. Álvarez-Prado, Á.F., Maas, R.R., Soukup, K., Klemm, F., Kornete, M., Krebs, F.S., Zoete, V., Berezowska, S., Brouland, J.-P., Hottinger, A.F., et al. (2023). Immunogenomic analysis of human brain metastases reveals diverse immune landscapes across genetically distinct tumors. Cell Reports Medicine *4*, 100900. https://doi.org/10.1016/j.xcrm.2022.100900.

23. Miarka, L., and Valiente, M. (2021). Animal models of brain metastasis. Neurooncol Adv *3*, v144–v156. https://doi.org/10.1093/noajnl/vdab115.

24. Valiente, M., Van Swearingen, A.E.D., Anders, C.K., Bairoch, A., Boire, A., Bos, P.D., Cittelly, D.M., Erez, N., Ferraro, G.B., Fukumura, D., et al. (2020). Brain Metastasis Cell Lines Panel: A Public Resource of Organotropic Cell Lines. Cancer Research *80*, 4314–4323. https://doi.org/10.1158/0008-5472.CAN-20-0291.

25. Cho, J.H., Robinson, J.P., Arave, R.A., Burnett, W.J., Kircher, D.A., Chen, G., Davies, M.A., Grossmann, A.H., VanBrocklin, M.W., McMahon, M., et al. (2015). AKT1 Activation Promotes Development of Melanoma Metastases. Cell Rep *13*, 898–905. https://doi.org/10.1016/j.celrep.2015.09.057.

26. Kircher, D.A., Trombetti, K.A., Silvis, M.R., Parkman, G.L., Fischer, G.M., Angel, S.N., Stehn, C.M., Strain, S.C., Grossmann, A.H., Duffy, K.L., et al. (2019). AKT1E17K Activates Focal Adhesion Kinase and Promotes Melanoma Brain Metastasis. Mol Cancer Res *17*, 1787–1800. https://doi.org/10.1158/1541-7786.MCR-18-1372.

27. Pérez-Guijarro, E., Yang, H.H., Araya, R.E., El Meskini, R., Michael, H.T., Vodnala, S.K., Marie, K.L., Smith, C., Chin, S., Lam, K.C., et al. (2020). Multimodel preclinical platform predicts clinical response of melanoma to immunotherapy. Nat Med *26*, 781–791. https://doi.org/10.1038/s41591-020-0818-3.

28. Bloom, M.B., Perry-Lalley, D., Robbins, P.F., Li, Y., El-Gamil, M., Rosenberg, S.A., and Yang, J.C. (1997). Identification of Tyrosinase-related Protein 2 as a Tumor Rejection Antigen for the B16 Melanoma. J Exp Med *185*, 453–460.

29. Tímár, J., Mészáros, L., Ladányi, A., Puskás, L.G., and Rásó, E. (2006). Melanoma genomics reveals signatures of sensitivity to bio- and targeted therapies. Cell Immunol *244*, 154–157. https://doi.org/10.1016/j.cellimm.2006.12.009.

30. Rappaport, J., Chen, Q., McGuire, T., Daugherty-Lopes, A., and Goldszmid, R.S. (2024). Development of an optimized machine learning approach to enhance brain metastatic burden assessment in preclinical models. bioRxiv, 2024.08.21.608131. https://doi.org/10.1101/2024.08.21.608131.

31. Nguyen, B., Fong, C., Luthra, A., Smith, S.A., DiNatale, R.G., Nandakumar, S., Walch, H., Chatila, W.K., Madupuri, R., Kundra, R., et al. (2022). Genomic characterization of metastatic patterns from prospective clinical sequencing of 25,000 patients. Cell *185*, 563-575.e11. https://doi.org/10.1016/j.cell.2022.01.003.

32. Cerami1, E., Gao, J., Dogrusoz, U., Gross, B.E., Sumer, S.O., Aksoy, B.A., Jacobsen, A., Byrne, C.J., Heuer, M.L., Larsson, E., et al. (2012). The cBio Cancer Genomics Portal: An Open Platform for Exploring Multidimensional Cancer Genomics Data. Cancer Discov *2*, 401–404. https://doi.org/10.1158/2159-8290.CD-12-0095.

33. Gao, J., Aksoy, B.A., Dogrusoz, U., Dresdner, G., Gross, B., Sumer, S.O., Sun, Y., Jacobsen, A., Sinha, R., Larsson, E., et al. (2013). Integrative Analysis of Complex Cancer Genomics and Clinical Profiles Using the cBioPortal. Science Signaling. https://doi.org/10.1126/scisignal.2004088.

34. de Bruijn, I., Kundra, R., Mastrogiacomo, B., Tran, T.N., Sikina, L., Mazor, T., Li, X., Ochoa, A., Zhao, G., Lai, B., et al. (2023). Analysis and Visualization of Longitudinal Genomic and Clinical Data from the AACR Project GENIE Biopharma Collaborative in cBioPortal. Cancer Res *83*, 3861–3867. https://doi.org/10.1158/0008-5472.CAN-23-0816.

35. Chen, G., Chakravarti, N., Aardalen, K., Lazar, A.J., Tetzlaff, M.T., Wubbenhorst, B., Kim, S.-B., Kopetz, S., Ledoux, A.A., Gopal, Y.N.V., et al. (2014). Molecular Profiling of Patient-Matched Brain and Extracranial Melanoma Metastases Implicates the PI3K Pathway as a Therapeutic Target. Clin Cancer Res *20*, 5537–5546. https://doi.org/10.1158/1078-0432.CCR-13-3003.

36. Brastianos, P.K., Carter, S.L., Santagata, S., Cahill, D.P., Taylor-Weiner, A., Jones, R.T., Van Allen, E.M., Lawrence, M.S., Horowitz, P.M., Cibulskis, K., et al. (2015). Genomic Characterization of Brain Metastases Reveals Branched Evolution and Potential Therapeutic Targets. Cancer Discov *5*, 1164–1177. https://doi.org/10.1158/2159-8290.CD-15-0369.

37. Morad, G., Helmink, B.A., Sharma, P., and Wargo, J.A. (2021). Hallmarks of response, resistance, and toxicity to immune checkpoint blockade. Cell *184*, 5309–5337. https://doi.org/10.1016/j.cell.2021.09.020.

38. Petitprez, F., Meylan, M., de Reyniès, A., Sautès-Fridman, C., and Fridman, W.H. (2020). The Tumor Microenvironment in the Response to Immune Checkpoint Blockade Therapies. Front Immunol *11*, 784. https://doi.org/10.3389/fimmu.2020.00784.

39. Lam, K.C., Araya, R.E., Huang, A., Chen, Q., Di Modica, M., Rodrigues, R.R., Lopès, A., Johnson, S.B., Schwarz, B., Bohrnsen, E., et al. (2021). Microbiota triggers STING-type I IFN-dependent monocyte reprogramming of the tumor microenvironment. Cell *184*, 5338-5356.e21. https://doi.org/10.1016/j.cell.2021.09.019.

40. Smalley, I., Chen, Z., Phadke, M., Li, J., Yu, X., Wyatt, C., Evernden, B., Messina, J.L., Sarnaik, A., Sondak, V.K., et al. (2021). Single-Cell Characterization of the Immune Microenvironment of Melanoma Brain and Leptomeningeal Metastases. Clin Cancer Res *27*, 4109–4125. https://doi.org/10.1158/1078-0432.CCR-21-1694.

41. Zakaria, R., Jenkinson, M.D., Radon, M., Das, K., Poptani, H., Rathi, N., and Rudland, P.S. (2023). Immune checkpoint inhibitor treatment of brain metastasis associated with a less invasive growth pattern, higher T-cell infiltration and raised tumor ADC on diffusion weighted MRI. Cancer Immunol Immunother *72*, 3387–3393. https://doi.org/10.1007/s00262-023-03499-z.

42. Andreatta, M., Corria-Osorio, J., Müller, S., Cubas, R., Coukos, G., and Carmona, S.J. (2021). Interpretation of T cell states from single-cell transcriptomics data using reference atlases. Nat Commun *12*, 2965. https://doi.org/10.1038/s41467-021-23324-4.

43. Sade-Feldman, M., Yizhak, K., Bjorgaard, S.L., Ray, J.P., de Boer, C.G., Jenkins, R.W., Lieb, D.J., Chen, J.H., Frederick, D.T., Barzily-Rokni, M., et al. (2018). Defining T cell states associated with response to checkpoint immunotherapy in melanoma. Cell *175*, 998-1013.e20. https://doi.org/10.1016/j.cell.2018.10.038.

44. Giles, J.R., Globig, A.-M., Kaech, S.M., and Wherry, E.J. (2023). CD8+ T cells in the cancer-immunity cycle. Immunity *56*, 2231–2253. https://doi.org/10.1016/j.immuni.2023.09.005.

45. Miller, B.C., Sen, D.R., Al Abosy, R., Bi, K., Virkud, Y.V., LaFleur, M.W., Yates, K.B., Lako, A., Felt, K., Naik, G.S., et al. (2019). Subsets of exhausted CD8+ T cells differentially mediate tumor control and respond to checkpoint blockade. Nat Immunol *20*, 326–336. https://doi.org/10.1038/s41590-019-0312-6.

46. Jiang, W., He, Y., He, W., Wu, G., Zhou, X., Sheng, Q., Zhong, W., Lu, Y., Ding, Y., Lu, Q., et al. (2021). Exhausted CD8+T Cells in the Tumor Immune Microenvironment: New Pathways to Therapy. Front. Immunol. *11*, 622509. https://doi.org/10.3389/fimmu.2020.622509.

47. Acharya, N., Madi, A., Zhang, H., Klapholz, M., Escobar, G., Dulberg, S., Christian, E., Ferreira, M., Dixon, K.O., Fell, G., et al. (2020). Endogenous Glucocorticoid Signaling Regulates CD8+ T Cell Differentiation and Development of Dysfunction in the Tumor Microenvironment. Immunity *53*, 658-671.e6. https://doi.org/10.1016/j.immuni.2020.08.005.

48. Damei, I., Trickovic, T., Mami-Chouaib, F., and Corgnac, S. (2023). Tumor-resident memory T cells as a biomarker of the response to cancer immunotherapy. Front. Immunol. *14*, 1205984. https://doi.org/10.3389/fimmu.2023.1205984.

49. Corgnac, S., Malenica, I., Mezquita, L., Auclin, E., Voilin, E., Kacher, J., Halse, H., Grynszpan, L., Signolle, N., Dayris, T., et al. (2020). CD103+CD8+ TRM Cells Accumulate in Tumors of Anti-PD-1-Responder Lung Cancer Patients and Are Tumor-Reactive Lymphocytes Enriched with Tc17. Cell Reports Medicine *1*. https://doi.org/10.1016/j.xcrm.2020.100127.

50. Edwards, J., Wilmott, J.S., Madore, J., Gide, T.N., Quek, C., Tasker, A., Ferguson, A., Chen, J., Hewavisenti, R., Hersey, P., et al. (2018). CD103+ Tumor-Resident CD8+ T Cells Are Associated with Improved Survival in Immunotherapy-Naïve Melanoma Patients and Expand Significantly During Anti–PD-1 Treatment. Clinical Cancer Research *24*, 3036–3045. https://doi.org/10.1158/1078-0432.CCR-17-2257.

51. Colonna, M., and Butovsky, O. (2017). Microglia Function in the Central Nervous System During Health and Neurodegeneration. Annu Rev Immunol *35*, 441–468. https://doi.org/10.1146/annurev-immunol-051116-052358.

52. Borst, K., Dumas, A.A., and Prinz, M. (2021). Microglia: Immune and non-immune functions. Immunity *54*, 2194–2208. https://doi.org/10.1016/j.immuni.2021.09.014.

53. Paolicelli, R.C., Sierra, A., Stevens, B., Tremblay, M.-E., Aguzzi, A., Ajami, B., Amit, I., Audinat, E., Bechmann, I., Bennett, M., et al. (2022). Microglia states and nomenclature: A field at its crossroads. Neuron *110*, 3458. https://doi.org/10.1016/j.neuron.2022.10.020.

54. Guldner, I.H., Wang, Q., Yang, L., Golomb, S.M., Zhao, Z., Lopez, J.A., Brunory, A., Howe, E.N., Zhang, Y., Palakurthi, B., et al. (2020). CNS-Native Myeloid Cells Drive Immune Suppression in the Brain Metastatic Niche through Cxcl10. Cell *183*, 1234-1248.e25. https://doi.org/10.1016/j.cell.2020.09.064.

55. You, H., Baluszek, S., and Kaminska, B. (2019). Immune Microenvironment of Brain Metastases—Are Microglia and Other Brain Macrophages Little Helpers? Front. Immunol. *10*, 1941. https://doi.org/10.3389/fimmu.2019.01941.

56. Evans, K.T., Blake, K., Longworth, A., Coburn, M.A., Insua-Rodríguez, J., McMullen, T.P., Nguyen, Q.H., Ma, D., Lev, T., Hernandez, G.A., et al. (2023). Microglia promote anti-tumour immunity and suppress breast cancer brain metastasis. Nat Cell Biol *25*, 1848–1859. https://doi.org/10.1038/s41556-023-01273-y.

57. Lin, S.-S., Tang, Y., Illes, P., and Verkhratsky, A. (2021). The Safeguarding Microglia: Central Role for P2Y12 Receptors. Front Pharmacol *11*, 627760. https://doi.org/10.3389/fphar.2020.627760.

58. Huang, C., Wang, X., Wang, Y., Feng, Y., Wang, X., Chen, S., Yan, P., Liao, J., Zhang, Q., Mao, C., et al. (2024). Sirpα on tumor-associated myeloid cells restrains antitumor immunity in colorectal cancer independent of its interaction with CD47. Nat Cancer *5*, 500–516. https://doi.org/10.1038/s43018-023-00691-z.

59. Hutter, G., Theruvath, J., Graef, C.M., Zhang, M., Schoen, M.K., Manz, E.M., Bennett, M.L., Olson, A., Azad, T.D., Sinha, R., et al. (2019). Microglia are effector cells of CD47-SIRPα antiphagocytic axis disruption against glioblastoma. Proceedings of the National Academy of Sciences *116*, 997–1006. https://doi.org/10.1073/pnas.1721434116.

60. Bian, Z., Shi, L., Kidder, K., Zen, K., Garnett-Benson, C., and Liu, Y. (2021). Intratumoral SIRPα-deficient macrophages activate tumor antigen-specific cytotoxic T cells under radiotherapy. Nat Commun *12*, 1–16. https://doi.org/10.1038/s41467-021-23442-z.

61. Niu, F., Yu, Y., Li, Z., Ren, Y., Li, Z., Ye, Q., Liu, P., Ji, C., Qian, L., and Xiong, Y. (2022). Arginase: An emerging and promising therapeutic target for cancer treatment. Biomed Pharmacother *149*, 112840. https://doi.org/10.1016/j.biopha.2022.112840.

62. Dixon, K.O., Lahore, G.F., and Kuchroo, V.K. (2024). Beyond T cell exhaustion: TIM-3 regulation of myeloid cells. Science Immunology. https://doi.org/10.1126/sciimmunol.adf2223.

63. Ausejo-Mauleon, I., Labiano, S., de la Nava, D., Laspidea, V., Zalacain, M., Marrodán, L., García-Moure, M., González-Huarriz, M., Hervás-Corpión, I., Dhandapani, L., et al. (2023). TIM-3 blockade in diffuse intrinsic pontine glioma models promotes tumor regression and antitumor immune memory. Cancer Cell *41*, 1911-1926.e8. https://doi.org/10.1016/j.ccell.2023.09.001.

64. Ocaña-Guzman, R., Torre-Bouscoulet, L., and Sada-Ovalle, I. (2016). TIM-3 Regulates Distinct Functions in Macrophages. Front Immunol *7*, 229. https://doi.org/10.3389/fimmu.2016.00229.

65. Finak, G., McDavid, A., Yajima, M., Deng, J., Gersuk, V., Shalek, A.K., Slichter, C.K., Miller, H.W., McElrath, M.J., Prlic, M., et al. (2015). MAST: a flexible statistical framework for assessing transcriptional changes and characterizing heterogeneity in single-cell RNA sequencing data. Genome Biol *16*, 278. https://doi.org/10.1186/s13059-015-0844-5.

66. Wang, T., Li, B., Nelson, C.E., and Nabavi, S. (2019). Comparative analysis of differential gene expression analysis tools for single-cell RNA sequencing data. BMC Bioinformatics *20*, 40. https://doi.org/10.1186/s12859-019-2599-6.

67. Lin, X., and Boutros, P.C. (2020). Optimization and expansion of non-negative matrix factorization. BMC Bioinformatics *21*, 7. https://doi.org/10.1186/s12859-019-3312-5.

68. Tirosh, I., Venteicher, A.S., Hebert, C., Escalante, L.E., Patel, A.P., Yizhak, K., Fisher, J.M., Rodman, C., Mount, C., Filbin, M.G., et al. (2016). Single-cell RNA-seq supports a developmental hierarchy in human oligodendroglioma. Nature *539*, 309–313. https://doi.org/10.1038/nature20123.

69. Kinker, G.S., Greenwald, A.C., Tal, R., Orlova, Z., Cuoco, M.S., McFarland, J.M., Warren, A., Rodman, C., Roth, J.A., Bender, S.A., et al. (2020). Pan-cancer single-cell RNA-seq identifies recurring programs of cellular heterogeneity. Nat Genet *52*, 1208–1218. https://doi.org/10.1038/s41588-020-00726-6.

70. Gavish, A., Tyler, M., Greenwald, A.C., Hoefflin, R., Simkin, D., Tschernichovsky, R., Galili Darnell, N., Somech, E., Barbolin, C., Antman, T., et al. (2023). Hallmarks of transcriptional intratumour heterogeneity across a thousand tumours. Nature *618*, 598–606. https://doi.org/10.1038/s41586-023-06130-4.

71. Zhou, Y., Zhou, B., Pache, L., Chang, M., Khodabakhshi, A.H., Tanaseichuk, O., Benner, C., and Chanda, S.K. (2019). Metascape provides a biologist-oriented resource for the analysis of systems-level datasets. Nat Commun *10*, 1523. https://doi.org/10.1038/s41467-019-09234-6.

72. Alvarez-Breckenridge, C., Markson, S.C., Stocking, J.H., Nayyar, N., Lastrapes, M., Strickland, M.R., Kim, A.E., de Sauvage, M., Dahal, A., Larson, J.M., et al. (2022). Microenvironmental Landscape of Human Melanoma Brain Metastases in Response to Immune Checkpoint Inhibition. Cancer Immunol Res *10*, 996–1012. https://doi.org/10.1158/2326-6066.CIR-21-0870.

73. Jin, C., Shao, Y., Zhang, X., Xiang, J., Zhang, R., Sun, Z., Mei, S., Zhou, J., Zhang, J., and Shi, L. (2021). A Unique Type of Highly-Activated Microglia Evoking Brain Inflammation via Mif/Cd74 Signaling Axis in Aged Mice. Aging Dis *12*, 2125–2139. https://doi.org/10.14336/AD.2021.0520.

74. Potru, P.S., and Spittau, B. (2023). CD74: a prospective marker for reactive microglia? Neural Regen Res *18*, 2673–2674. https://doi.org/10.4103/1673-5374.371350.

75. Jahn, J., Bollensdorf, A., Kalischer, C., Piecha, R., Weiß-Müller, J., Potru, P.S., Ruß, T., and Spittau, B. (2022). Microglial CD74 Expression Is Regulated by TGFβ Signaling. Int J Mol Sci *23*, 10247. https://doi.org/10.3390/ijms231810247.

76. Wiersma, V.R., de Bruyn, M., Helfrich, W., and Bremer, E. (2013). Therapeutic potential of Galectin-9 in human disease. Medicinal Research Reviews *33*, E102–E126. https://doi.org/10.1002/med.20249.

77. Nobumoto, A., Oomizu, S., Arikawa, T., Katoh, S., Nagahara, K., Miyake, M., Nishi, N., Takeshita, K., Niki, T., Yamauchi, A., et al. (2009). Galectin-9 expands unique macrophages exhibiting plasmacytoid dendritic cell-like phenotypes that activate NK cells in tumor-bearing mice. Clinical Immunology *130*, 322–330. https://doi.org/10.1016/j.clim.2008.09.014.

78. Ozga, A.J., Chow, M.T., and Luster, A.D. (2021). Chemokines and the immune response to cancer. Immunity *54*, 859. https://doi.org/10.1016/j.immuni.2021.01.012.

79. Harlin, H., Meng, Y., Peterson, A.C., Zha, Y., Tretiakova, M., Slingluff, C., McKee, M., and Gajewski, T.F. (2009). Chemokine Expression in Melanoma Metastases Associated with CD8+ T-Cell Recruitment. Cancer Res *69*, 3077–3085. https://doi.org/10.1158/0008-5472.CAN-08-2281.

80. Allen, F., Bobanga, I.D., Rauhe, P., Barkauskas, D., Teich, N., Tong, C., Myers, J., and Huang, A.Y. (2017). CCL3 augments tumor rejection and enhances CD8+ T cell infiltration through NK and CD103+ dendritic cell recruitment via IFNγ. Oncoimmunology *7*, e1393598. https://doi.org/10.1080/2162402X.2017.1393598.

81. Caushi, J.X., Zhang, J., Ji, Z., Vaghasia, A., Zhang, B., Hsiue, E.H.-C., Mog, B.J., Hou, W., Justesen, S., Blosser, R., et al. (2021). Transcriptional programs of neoantigen-specific TIL in anti-PD-1-treated lung cancers. Nature *596*, 126–132. https://doi.org/10.1038/s41586-021-03752-4.

82. Lowery, F.J., Krishna, S., Yossef, R., Parikh, N.B., Chatani, P.D., Zacharakis, N., Parkhurst, M.R., Levin, N., Sindiri, S., Sachs, A., et al. (2022). Molecular signatures of antitumor neoantigen-reactive T cells from metastatic human cancers. Science *375*, 877–884. https://doi.org/10.1126/science.abl5447.

83. Hanada, K.-I., Zhao, C., Gil-Hoyos, R., Gartner, J.J., Chow-Parmer, C., Lowery, F.J., Krishna, S., Prickett, T.D., Kivitz, S., Parkhurst, M.R., et al. (2022). A phenotypic signature that identifies neoantigen-reactive T cells in fresh human lung cancers. Cancer Cell *40*, 479-493.e6. https://doi.org/10.1016/j.ccell.2022.03.012.

84. Oliveira, G., Stromhaug, K., Klaeger, S., Kula, T., Frederick, D.T., Le, P.M., Forman, J., Huang, T., Li, S., Zhang, W., et al. (2021). Phenotype, specificity and avidity of antitumour CD8+ T cells in melanoma. Nature *596*, 119–125. https://doi.org/10.1038/s41586-021-03704-y.

85. van der Leun, A.M., Thommen, D.S., and Schumacher, T.N. (2020). CD8+ T cell states in human cancer: insights from single-cell analysis. Nat Rev Cancer *20*, 218–232. https://doi.org/10.1038/s41568-019-0235-4.

86. Tan, X.-L., Le, A., Scherrer, E., Tang, H., Kiehl, N., Han, J., Jiang, R., Diede, S.J., and Shui, I.M. (2022). Systematic literature review and meta-analysis of clinical outcomes and prognostic factors for melanoma brain metastases. Frontiers in Oncology *12*.

87. Achrol, A.S., Rennert, R.C., Anders, C., Soffietti, R., Ahluwalia, M.S., Nayak, L., Peters, S., Arvold, N.D., Harsh, G.R., Steeg, P.S., et al. (2019). Brain metastases. Nat Rev Dis Primers *5*, 5. https://doi.org/10.1038/s41572-018-0055-y.

88. Lee, J.E., and Yang, S.H. (2023). Advances in Brain Metastasis Models. Brain Tumor Res Treat *11*, 16–21. https://doi.org/10.14791/btrt.2022.0037.

89. Jansen, C.S., Prabhu, R.S., Pagadala, M.S., Chappa, P., Goyal, S., Zhou, C., Neill, S.G., Prokhnevska, N., Cardenas, M., Hoang, K.B., et al. (2023). Immune niches in brain metastases contain TCF1+ stem-like T cells, are associated with disease control and are modulated by preoperative SRS. Res Sq, rs.3.rs-2722744. https://doi.org/10.21203/rs.3.rs-2722744/v1.

90. Zakaria, R., Platt-Higgins, A., Rathi, N., Radon, M., Das, S., Das, K., Bhojak, M., Brodbelt, A., Chavredakis, E., Jenkinson, M.D., et al. (2018). T-Cell Densities in Brain Metastases Are Associated with Patient Survival Times and Diffusion Tensor MRI Changes. Cancer Res *78*, 610–616. https://doi.org/10.1158/0008-5472.CAN-17-1720.

91. Harter, P.N., Bernatz, S., Scholz, A., Zeiner, P.S., Zinke, J., Kiyose, M., Blasel, S., Beschorner, R., Senft, C., Bender, B., et al. (2015). Distribution and prognostic relevance of tumor-infiltrating lymphocytes (TILs) and PD-1/PD-L1 immune checkpoints in human brain metastases. Oncotarget *6*. https://doi.org/10.18632/oncotarget.5696.

92. Berghoff, A.S., Ricken, G., Wilhelm, D., Rajky, O., Widhalm, G., Dieckmann, K., Birner, P., Bartsch, R., and Preusser, M. (2016). Tumor infiltrating lymphocytes and PD-L1 expression in brain metastases of small cell lung cancer (SCLC). J Neurooncol *130*, 19–29. https://doi.org/10.1007/s11060-016-2216-8.

93. Schetters, S.T.T., Gomez-Nicola, D., Garcia-Vallejo, J.J., and Van Kooyk, Y. (2018). Neuroinflammation: Microglia and T Cells Get Ready to Tango. Front Immunol *8*, 1905. https://doi.org/10.3389/fimmu.2017.01905.

94. Rodríguez, A.M., Rodríguez, J., and Giambartolomei, G.H. (2022). Microglia at the Crossroads of Pathogen-Induced Neuroinflammation. ASN Neuro *14*, 17590914221104566. https://doi.org/10.1177/17590914221104566.

95. Chen, X., Firulyova, M., Manis, M., Herz, J., Smirnov, I., Aladyeva, E., Wang, C., Bao, X., Finn, M.B., Hu, H., et al. (2023). Microglia-mediated T cell Infiltration Drives Neurodegeneration in Tauopathy. Nature *615*, 668–677. https://doi.org/10.1038/s41586-023-05788-0.

96. Chen, D., Varanasi, S.K., Hara, T., Traina, K., Sun, M., McDonald, B., Farsakoglu, Y., Clanton, J., Xu, S., Garcia-Rivera, L., et al. (2023). CTLA-4 blockade induces a microglia-Th1 cell partnership that stimulates microglia phagocytosis and anti-tumor function in glioblastoma. Immunity *56*, 2086-2104.e8. https://doi.org/10.1016/j.immuni.2023.07.015.

97. von Roemeling, C.A., Patel, J.A., Carpenter, S.L., Yegorov, O., Yang, C., Bhatia, A., Doonan, B.P., Russell, R., Trivedi, V.S., Klippel, K., et al. (2024). Adeno-associated virus delivered CXCL9 sensitizes glioblastoma to anti-PD-1 immune checkpoint blockade. Nat Commun *15*, 5871. https://doi.org/10.1038/s41467-024-49989-1.

98. Wang, L., Li, C., Zhan, H., Li, S., Zeng, K., Xu, C., Zou, Y., Xie, Y., Zhan, Z., Yin, S., et al. (2024). Targeting the HSP47-collagen axis inhibits brain metastasis by reversing M2 microglial polarization and restoring anti-tumor immunity. CR Med *5*. https://doi.org/10.1016/j.xcrm.2024.101533.

99. Feng, Y., Hu, X., Zhang, Y., and Wang, Y. (2024). The Role of Microglia in Brain Metastases: Mechanisms and Strategies. Aging Dis *15*, 169–185. https://doi.org/10.14336/AD.2023.0514.

100. Nguyen, L.T., Aprico, A., Nwoke, E., Walsh, A.D., Blades, F., Avneri, R., Martin, E., Zalc, B., Kilpatrick, T.J., and Binder, M.D. (2023). Mertk-expressing microglia influence oligodendrogenesis and myelin modelling in the CNS. Journal of Neuroinflammation *20*, 253. https://doi.org/10.1186/s12974-023-02921-8.

101. Gilchrist, S.E., Goudarzi, S., and Hafizi, S. (2020). Gas6 Inhibits Toll-Like Receptor-Mediated Inflammatory Pathways in Mouse Microglia via Axl and Mer. Front Cell Neurosci *14*, 576650. https://doi.org/10.3389/fncel.2020.576650.

102. Moertel, C.L., Xia, J., LaRue, R., Waldron, N.N., Andersen, B.M., Prins, R.M., Okada, H., Donson, A.M., Foreman, N.K., Hunt, M.A., et al. (2014). CD200 in CNS tumor-induced immunosuppression: the role for CD200 pathway blockade in targeted immunotherapy. J Immunother Cancer *2*, 46. https://doi.org/10.1186/s40425-014-0046-9.

103. Ngwa, C., and Liu, F. (2019). CD200-CD200R signaling and diseases: a potential therapeutic target? Int J Physiol Pathophysiol Pharmacol *11*, 297–309.

104. Timmerman, R., Zuiderwijk-Sick, E.A., Baron, W., and Bajramovic, J.J. (2023). In silico-in vitro modeling to uncover cues involved in establishing microglia identity: TGF-β3 and laminin can drive microglia signature gene expression. Front Cell Neurosci *17*, 1178504. https://doi.org/10.3389/fncel.2023.1178504.

105. Rigby, M.J., Gomez, T.M., and Puglielli, L. (2020). Glial Cell-Axonal Growth Cone Interactions in Neurodevelopment and Regeneration. Front Neurosci *14*, 203. https://doi.org/10.3389/fnins.2020.00203.

106. Lee, W.S., Lee, W.-H., Bae, Y.C., and Suk, K. (2019). Axon Guidance Molecules Guiding Neuroinflammation. Exp Neurobiol *28*, 311–319. https://doi.org/10.5607/en.2019.28.3.311.

107. Tang, J., Jin, Y., Jia, F., Lv, T., Manaenko, A., Zhang, L.-F., Zhang, Z., Qi, X., Xue, Y., Zhao, B., et al. (2023). Gas6 Promotes Microglia Efferocytosis and Suppresses Inflammation Through Activating Axl/Rac1 Signaling in Subarachnoid Hemorrhage Mice. Transl Stroke Res *14*, 955–969. https://doi.org/10.1007/s12975-022-01099-0.

108. Fazio, F., Ulivieri, M., Volpi, C., Gargaro, M., and Fallarino, F. (2018). Targeting metabotropic glutamate receptors for the treatment of neuroinflammation. Current Opinion in Pharmacology *38*, 16–23. https://doi.org/10.1016/j.coph.2018.01.010.

109. Szepesi, Z., Manouchehrian, O., Bachiller, S., and Deierborg, T. (2018). Bidirectional Microglia-Neuron Communication in Health and Disease. Front Cell Neurosci *12*, 323. https://doi.org/10.3389/fncel.2018.00323.

110. Colonna, M. (2023). The biology of TREM receptors. Nat Rev Immunol *23*, 580–594. https://doi.org/10.1038/s41577-023-00837-1.

111. Yin, R.-H., Yu, J.-T., and Tan, L. (2015). The Role of SORL1 in Alzheimer's Disease. Mol Neurobiol *51*, 909–918. https://doi.org/10.1007/s12035-014-8742-5.

112. Rogaeva, E., Meng, Y., Lee, J.H., Gu, Y., Kawarai, T., Zou, F., Katayama, T., Baldwin, C.T., Cheng, R., Hasegawa, H., et al. (2007). The neuronal sortilin-related receptor SORL1 is genetically associated with Alzheimer disease. Nat Genet *39*, 168–177. https://doi.org/10.1038/ng1943.

113. Kleffman, K., Levinson, G., Rose, I.V.L., Blumenberg, L.M., Shadaloey, S.A.A., Dhabaria, A., Wong, E., Galán-Echevarría, F., Karz, A., Argibay, D., et al. (2022). Melanoma-Secreted Amyloid Beta Suppresses Neuroinflammation and Promotes Brain Metastasis. Cancer Discovery *12*, 1314–1335. https://doi.org/10.1158/2159-8290.CD-21-1006.

114. So, J.-S., Kim, H., and Han, K.-S. (2021). Mechanisms of Invasion in Glioblastoma: Extracellular Matrix, Ca2+ Signaling, and Glutamate. Frontiers in Cellular Neuroscience *15*. https://doi.org/10.3389/fncel.2021.663092.

115. Huang, Q., Chen, L., Liang, J., Huang, Q., and Sun, H. (2022). Neurotransmitters: Potential Targets in Glioblastoma. Cancers (Basel) *14*, 3970. https://doi.org/10.3390/cancers14163970.

116. Bankhead, P., Loughrey, M.B., Fernández, J.A., Dombrowski, Y., McArt, D.G., Dunne, P.D., McQuaid, S., Gray, R.T., Murray, L.J., Coleman, H.G., et al. (2017). QuPath: Open source software for digital pathology image analysis. Sci Rep *7*, 16878. https://doi.org/10.1038/s41598-017-17204-5.

117. Virador, V., Matsunaga, N., Matsunaga, J., Valencia, J., Oldham, R.J., Kameyama, K., Peck, G.L., Ferrans, V.J., Vieira, W.D., Abdel-Malek, Z.A., et al. (2001). Production of Melanocyte-Specific Antibodies to Human Melanosomal Proteins: Expression Patterns in Normal Human Skin and in Cutaneous Pigmented Lesions. Pigment Cell Research *14*, 289–297. https://doi.org/10.1034/j.1600-0749.2001.140410.x.

118. Korin, B., Dubovik, T., and Rolls, A. (2018). Mass cytometry analysis of immune cells in the brain. Nat Protoc *13*, 377–391. https://doi.org/10.1038/nprot.2017.155.

119. Araya, R.E., and Goldszmid, R.S. (2020). Characterization of the tumor immune infiltrate by multiparametric flow cytometry and unbiased high-dimensional data analysis. Methods Enzymol *632*, 309–337. https://doi.org/10.1016/bs.mie.2019.11.012.

120. Ashhurst, T.M., Marsh-Wakefield, F., Putri, G.H., Spiteri, A.G., Shinko, D., Read, M.N., Smith, A.L., and King, N.J.C. (2022). Integration, exploration, and analysis of high-dimensional single-cell cytometry data using Spectre. Cytometry Part A *101*, 237–253. https://doi.org/10.1002/cyto.a.24350.

121. Hao, Y., Hao, S., Andersen-Nissen, E., Mauck, W.M., Zheng, S., Butler, A., Lee, M.J., Wilk, A.J., Darby, C., Zager, M., et al. (2021). Integrated analysis of multimodal single-cell data. Cell *184*, 3573-3587.e29. https://doi.org/10.1016/j.cell.2021.04.048.

122. McInnes, L., Healy, J., Saul, N., and Großberger, L. (2018). UMAP: Uniform Manifold Approximation and Projection. Journal of Open Source Software *3*, 861. https://doi.org/10.21105/joss.00861.

123. Hao, Y., Stuart, T., Kowalski, M.H., Choudhary, S., Hoffman, P., Hartman, A., Srivastava, A., Molla, G., Madad, S., Fernandez-Granda, C., et al. (2024). Dictionary learning for integrative, multimodal and scalable single-cell analysis. Nat Biotechnol *42*, 293–304. https://doi.org/10.1038/s41587-023-01767-y.

124. Ianevski, A., Giri, A.K., and Aittokallio, T. (2022). Fully-automated and ultra-fast cell-type identification using specific marker combinations from single-cell transcriptomic data. Nat Commun *13*, 1246. https://doi.org/10.1038/s41467-022-28803-w.

125. Aibar, S., González-Blas, C.B., Moerman, T., Huynh-Thu, V.A., Imrichova, H., Hulselmans, G., Rambow, F., Marine, J.-C., Geurts, P., Aerts, J., et al. (2017). SCENIC: Single-cell regulatory network inference and clustering. Nature methods *14*, 1083. https://doi.org/10.1038/nmeth.4463.

126. Jin, S., Guerrero-Juarez, C.F., Zhang, L., Chang, I., Ramos, R., Kuan, C.-H., Myung, P., Plikus, M.V., and Nie, Q. (2021). Inference and analysis of cell-cell communication using CellChat. Nat Commun *12*, 1088. https://doi.org/10.1038/s41467-021-21246-9.

SUPPLEMENTARY TABLES

Table S1: Tumor cell lines mutated genes.

Table S2: Immune cell annotations.

Table S3: $CD8^+$ T cell T cell cluster-defining genes.

Table S4: $CD4^+$ T cell T cell cluster-defining genes.

Table S5: List of the genes associated with each metaprogram.

Table S6: Patient T cell signatures and BR1 and BR3 gene signatures.

Table S1: Tumor cell line mutated genes.

The number is variant allele frequncy (VAF). Subline-specific mutated genes can be shown by filtering genes with VAF = 0 in other two lines.

In red: unique mutations found in BR1

In blue: unique mutations found in BR3

	parental	BR1	BR3
Abca1	1	1	0.99
Inpp5b	1	0.99	1
Ago4	0.99	1	0.99
Mcf2	0.99	1	1
Prpf38a	0.99	0.99	0.99
Aifm1	0.98	1	1
Plp1	0.94	0.99	1
Rbm19	0.69	0.71	0.65
Irak3	0.68	0.66	0.68
Pilrb1	0.68	0.59	0.66
Baiap2l1	0.66	0.65	0.67
Adamts19	0.65	0.61	0.65
Mcph1	0.65	0.68	0.64
Inpp4b	0.64	0.68	0.64
Lphn1	0.64	0.67	0.67
Trim46	0.64	0.55	0.42
Vdr	0.64	0.58	0.33
Hmgb2	0.63	0.64	0.55
Usp13	0.63	0.54	0.49
Glra3	0.62	0.64	0.52
Ikbkb	0.62	0.69	0.62
Cyp2d34	0.61	0.51	0.32
Scg2	0.6	0.56	0.32
Gimap6	0.57	0.34	0.38
Ikzf3	0.56	0.47	0.53
Dnah6	0.55	0.38	0.36
Gm4636	0.55	0.4	0.53
Vmn1r42	0.55	0.38	0.35
Cul9	0.54	0.49	0.5
Knstrn	0.54	0.47	0.52
Obscn	0.54	0.53	0.48
Sec14l4	0.54	0.46	0.47
Vmn1r8	0.54	0.36	0.34
Alas1	0.53	0.53	0.48
Fam98c	0.53	0.46	0.49
Pepd	0.53	0.5	0.41
Ptchd3	0.53	0.51	0.49
Vmn1r17	0.53	0.32	0.35
1700029F12Rik	0.52	0.47	0.49

Casc5	0.52	0.46	0.46
Gpank1	0.52	0.47	0.5
Il3	0.52	0.5	0.53
Larp1	0.52	0.5	0.5
Lrrn2	0.52	0.47	0.29
Pde11a	0.52	0.47	0.47
Slc22a6	0.52	0.48	0.49
Uggt2	0.52	0.5	0.52
Uso1	0.52	0.54	0.46
Zfp748	0.52	0.29	0.5
Actc1	0.51	0.53	0.44
Atxn7l1	0.51	0.56	0.48
Ebf2	0.51	0.48	0.49
Gas8	0.51	0.54	0.47
Gcfc2	0.51	0.34	0.34
Gm527	0.51	0.63	0.46
Macf1	0.51	0.54	0.47
Ms4a5	0.51	0.47	0.47
Shank1	0.51	0.45	0.48
Snta1	0.51	0.47	0.49
Sp110	0.51	0.5	0.47
Sp140	0.51	0.51	0.52
Abcc4	0.5	0.49	0.55
Acsf3	0.5	0.5	0.52
Actl9	0.5	0.45	0.48
Cd36	0.5	0.47	0.48
Cdh15	0.5	0.48	0.49
Dis3l	0.5	0.49	0.48
Dock9	0.5	0.47	0.49
Erbb4	0.5	0.57	0.32
Fn3k	0.5	0.49	0.5
Gdpd5	0.5	0.49	0.5
Gnaq	0.5	0.49	0.42
Lrdd	0.5	0.51	0.48
Nsmaf	0.5	0.49	0.47
Pde3b	0.5	0.44	0.52
Rab11fip3	0.5	0.47	0.45
Rims1	0.5	0.48	0.48
Tfap2a	0.5	0.45	0.51
Tmeff2	0.5	0.48	0.5
Wdr60	0.5	0.58	0.5
Bai3	0.49	0.47	0.41
Cbx2	0.49	0.52	0.45
Exph5	0.49	0.5	0.5
Fes	0.49	0.51	0.5

Fmn1	0.49	0.49	0.5
Gm12169	0.49	0.47	0.45
Gpr125	0.49	0.47	0.47
Itgad	0.49	0.49	0.45
Mlh3	0.49	0.6	0.55
Ms4a4d	0.49	0.48	0.46
N4bp2	0.49	0.47	0.48
Naip5	0.49	0.45	0.48
Olfr1494	0.49	0.49	0.48
Olfr77	0.49	0.48	0.48
Slc19a1	0.49	0.46	0.51
Tcerg1l	0.49	0.49	0.49
Vmn2r115	0.49	0.46	0.48
7-Mar	0.48	0.46	0.46
2610008E11Rik	0.48	0.54	0.44
A830010M20Rik	0.48	0.48	0.5
Aatk	0.48	0.51	0.52
Atp10a	0.48	0.52	0.51
Bnip3l	0.48	0.43	0.45
C2cd4c	0.48	0.46	0.47
Chek2	0.48	0.47	0.47
Dock8	0.48	0.52	0.49
Hc	0.48	0.45	0.49
Hs3st5	0.48	0.45	0.49
Itgb1	0.48	0.5	0.5
Mctp1	0.48	0.45	0.51
Polr2a	0.48	0.45	0.46
Serpina3k	0.48	0.39	0.47
Vmn2r110	0.48	0.46	0.47
Zfyve27	0.48	0.46	0.46
9030617O03Rik	0.47	0.59	0.44
Acaa2	0.47	0.46	0.46
Anapc1	0.47	0.51	0.47
Col6a2	0.47	0.47	0.51
Col7a1	0.47	0.5	0.5
Dse	0.47	0.48	0.46
Enam	0.47	0.52	0.49
Fat3	0.47	0.49	0.39
Gpr83	0.47	0.53	0.51
Hbp1	0.47	0.39	0.54
Hrasls5	0.47	0.49	0.43
Llgl1	0.47	0.46	0.48
Nlrp4c	0.47	0.51	0.5
Nme9	0.47	0.48	0.47
Olfr1373	0.47	0.5	0.49

Olfr352	0.47	0.47	0.45
Pdcd6ip	0.47	0.46	0.45
Taf5l	0.47	0.51	0.49
Tnks1bp1	0.47	0.46	0.52
Vmn2r97	0.47	0.44	0.47
Zbtb12	0.47	0.46	0.47
Zfp865	0.47	0.46	0.5
Atr	0.46	0.48	0.45
Cdh23	0.46	0.49	0.52
Csf2ra	0.46	0.42	0.44
Fra10ac1	0.46	0.47	0.48
Gm597	0.46	0.46	0.46
Khk	0.46	0.47	0.48
Myh6	0.46	0.43	0.47
Myo9a	0.46	0.47	0.47
Nedd4l	0.46	0.47	0.46
Nom1	0.46	0.46	0.43
Nt5dc1	0.46	0.52	0.41
Olfr1024	0.46	0.5	0.52
Ostm1	0.46	0.5	0.44
Pfas	0.46	0.42	0.49
Phyhipl	0.46	0.52	0.47
Pramel7	0.46	0.5	0.42
Prr14l	0.46	0.45	0.46
Rab26	0.46	0.44	0.48
Abca13	0.45	0.45	0.44
Atp4a	0.45	0.48	0.46
B4galnt4	0.45	0.47	0.46
Ceacam20	0.45	0.45	0.52
Fras1	0.45	0.46	0.52
Gapdhs	0.45	0.55	0.61
Gm12185	0.45	0.43	0.44
Gnaz	0.45	0.47	0.49
Grid1	0.45	0.46	0.44
Gzmd	0.45	0.5	0.47
Map4k4	0.45	0.48	0.49
Mettl9	0.45	0.48	0.43
Olfr1466	0.45	0.5	0.46
Olfr90	0.45	0.5	0.45
Pds5a	0.45	0.47	0.45
Pla2g4d	0.45	0.49	0.49
Ppp1r18	0.45	0.44	0.49
Proser2	0.45	0.5	0.48
Ric8	0.45	0.49	0.44
Rps12	0.45	0.45	0.44

Tmc5	0.45	0.47	0.51
Top2a	0.45	0.5	0.47
Vmn2r124	0.45	0.48	0.44
Zfyve19	0.45	0.5	0.47
Cpeb1	0.44	0.44	0.51
Gm4745	0.44	0.44	0.47
Hoxb2	0.44	0.52	0.56
Mbd5	0.44	0.43	0.46
Mrc1	0.44	0.44	0.45
Ncoa7	0.44	0.45	0.45
Psmd13	0.44	0.45	0.45
Tdrd5	0.44	0.5	0.64
Ttn	0.44	0.48	0.48
5730507C01Rik	0.43	0.35	0.43
9530053A07Rik	0.43	0.5	0.46
Ager	0.43	0.47	0.43
Eef2	0.43	0.44	0.46
Enpp7	0.43	0.44	0.52
Fat2	0.43	0.43	0.45
Gm1110	0.43	0.49	0.5
Khnyn	0.43	0.48	0.56
Med13	0.43	0.48	0.49
Mia2	0.43	0.59	0.45
Prg4	0.43	0.48	0.65
Trp53bp2	0.43	0.46	0.67
Pon3	0.42	0.62	0.49
Astn1	0.41	0.46	0.7
Atp2b4	0.41	0.42	0.63
Kcnj3	0.41	0.5	0.43
Nfxl1	0.41	0.42	0.48
Pkhd1	0.41	0.44	0.53
Sele	0.41	0.49	0.62
Capn3	0.4	0.53	0.47
E330021D16Rik	0.4	0.61	0.62
Mapk7	0.4	0.43	0.45
Aox3	0.39	0.42	0.65
Crhr2	0.39	0.63	0.58
Dnah2	0.39	0.48	0.48
Srebf2	0.39	0.51	0.68
Ubash3b	0.39	0.44	0.46
Tatdn3	0.38	0.43	0.64
Apol7e	0.37	0.43	0.67
Cacna1i	0.37	0.47	0.64
Dennd6b	0.37	0.45	0.62
Lmna	0.37	0.43	0.48

Atp2b1	0.36	0.36	0.31
Cttnbp2	0.36	0.61	0.47
S100a9	0.36	0.45	0.5
Ankhd1	0.35	0.41	0.3
Asic1	0.35	0.46	0.67
Cdh8	0.35	0.29	0.33
Col24a1	0.35	0.44	0.5
Dync1li2	0.35	0.34	0.36
Pdxp	0.35	0.45	0.62
Sf3b1	0.35	0.42	0.6
Sharpin	0.35	0.42	0.68
Tlr2	0.35	0.44	0.48
Chga	0.34	0.41	0.52
Pnpla3	0.34	0.41	0.67
Slc48a1	0.34	0.2	0.31
Sprr2f	0.34	0.41	0.5
Trps1	0.34	0.37	0.61
Vmn2r121	0.34	0.36	0.37
Bai1	0.33	0.26	0.33
Cog4	0.33	0.34	0.32
Mfn1	0.33	0.31	0.49
Nav3	0.33	0.32	0.3
Rsbn1	0.33	0.4	0.52
Slc29a4	0.33	0.26	0.28
Bcar1	0.32	0.31	0.32
Cage1	0.32	0.36	0.37
Ccdc53	0.32	0.34	0.3
Eea1	0.32	0.3	0.29
Gm8298	0.32	0.58	0.43
Scube1	0.32	0.41	0.66
Spag1	0.32	0.29	0.64
Ido2	0.31	0.32	0.36
Nr4a1	0.31	0.42	0.63
Ptpro	0.31	0.3	0.29
Tdpoz3	0.31	0.39	0.45
Trio	0.31	0.37	0.62
Cul2	0.3	0.37	0.32
Gdf1	0.3	0.32	0.47
Irs2	0.3	0.34	0.31
Tbxas1	0.3	0.33	0.31
Adamts20	0.29	0.18	0.29
Kras	0.29	0.28	0.29
Nod1	0.29	0.31	0.28
BC094916	0.28	0.32	0.43
Jhdm1d	0.28	0.27	0.21

Vmn2r18	0.27	0.2	0.31
Cep120	0.26	0.33	0.32
Gm14446	0.26	0.26	0.24
Peg10	0.25	0.29	0.27
Rictor	0.24	0.26	0.32
Vmn1r77	0.24	0.24	0.24
Amfr	0.23	0.17	0.25
Ptpn3	0.23	0.25	0.48
Il17rc	0.21	0.34	0.34
Clec4a2	0.2	0.3	0.32
Cdca3	0.19	0.31	0.3
Gm13154	0.18	0.53	0.42
Vmn2r89	0.17	0.2	0.17
Eri1	0.16	0.24	0.18
Apba3	0.14	0	0
Asmt	0.5	0	0
Atl2	0.19	0	0
Bbs9	0.14	0	0
Bcorl1	0.12	0	0
Clca6	0.34	0	0
Cog2	0.14	0	0
Cst7	0.14	0	0
Cyp2f2	0.13	0	0
Ect2l	0.13	0	0
Irf2bp2	0.13	0	0
Mphosph6	0.16	0	0
Mx2	0.13	0	0
Olfr902	0.16	0	0
Olfr951	0.16	0	0
Peg3	0.15	0	0
Plekho1	0.31	0	0
R3hdm1	0.12	0	0
Slc13a4	0.22	0	0
Smarcc1	0.19	0	0
Snai1	0.16	0	0
Stk32c	0.13	0	0
Tenm2	0.15	0	0
Vps13b	0.13	0	0
Xrn1	0.17	0	0
Zfc3h1	0.12	0	0
2310035C23Rik	0	0.11	0
4632434I11Rik	0	0.23	0
4921506M07Rik	0	0.17	0
4930402H24Rik	0	0.11	0
Abcc2	0	0.14	0

Abcc6	0	0.13	0
Abhd16b	0	0.23	0
Adam19	0	0.21	0
Adamts9	0	0.16	0
Agpat4	0	0.24	0
Ajap1	0	0.25	0
Ak2	0	0.22	0
Akap13	0	0.13	0
Alpk2	0	0.22	0
Alpk3	0	0.1	0
Ankk1	0	0.1	0
Atp13a2	0	0.15	0
Atp2b2	0	0.19	0
Atp6v0d2	0	0.12	0
Atpaf2	0	0.26	0
Bcmo1	0	0.18	0
Cacna1b	0	0.17	0
Ccdc162	0	0.12	0
Ccdc171	0	0.14	0
Ccdc177	0	0.25	0
Ccdc64b	0	0.14	0
Chrm2	0	0.17	0
Ckm	0	0.12	0
Coq9	0	0.12	0
Cpz	0	0.2	0
Csrnp3	0	0.11	0
Cxadr	0	0.2	0
Cyp2b23	0	0.21	0
Diap1	0	0.12	0
Dido1	0	0.19	0
Dlg5	0	0.13	0
Dnah7a	0	0.18	0
Dspp	0	0.12	0
Eif5	0	0.32	0
Elmo2	0	0.13	0
En2	0	0.15	0
Fam179b	0	0.12	0
Fanca	0	0.12	0
Fancg	0	0.12	0
Fbxo40	0	0.21	0
Frem1	0	0.18	0
Fuca1	0	0.11	0
Gab2	0	0.21	0
Galnt3	0	0.24	0
Gm10220	0	0.15	0

Gm6614	0	0.1	0
Greb1	0	0.19	0
Gse1	0	0.13	0
Gstk1	0	0.13	0
Herc4	0	0.24	0
Hiatl1	0	0.1	0
Hnrnpul2	0	0.18	0
Huwe1	0	0.22	0
Il13ra2	0	0.19	0
Il17d	0	0.12	0
Il17rd	0	0.2	0
Il1f10	0	0.13	0
Itgb8	0	0.19	0
Jmy	0	0.22	0
Kcnab2	0	0.23	0
Kcnq5	0	0.19	0
Kcnu1	0	0.15	0
Klf2	0	0.1	0
Klhdc4	0	0.19	0
Kndc1	0	0.24	0
Krt82	0	0.14	0
Lipi	0	0.2	0
Lmf1	0	0.12	0
Ltbp1	0	0.13	0
Mark4	0	0.11	0
Mid1ip1	0	0.28	0
Mllt6	0	0.22	0
Ms4a4c	0	0.13	0
Msh4	0	0.2	0
Muc4	0	0.21	0
Nedd4	0	0.25	0
Nfatc2	0	0.14	0
Nlgn3	0	0.1	0
Npb	0	0.21	0
Nxf2	0	0.49	0
Ogdh	0	0.19	0
Olfr1341	0	0.13	0
Olfr1347	0	0.23	0
Olfr198	0	0.23	0
Olfr304	0	0.24	0
Olfr676	0	0.19	0
Olfr691	0	0.2	0
Olfr911-ps1	0	0.22	0
Paqr3	0	0.09	0
Phf3	0	0.12	0

Phf8	0	0.42	0
Pias2	0	0.23	0
Pikfyve	0	0.19	0
Plec	0	0.12	0
Ppm1g	0	0.18	0
Prkrip1	0	0.15	0
Prr14	0	0.22	0
Prrc2a	0	0.28	0
Prrt4	0	0.12	0
Prss50	0	0.09	0
Rab3gap1	0	0.11	0
Rad21l	0	0.22	0
Rbp3	0	0.13	0
Rdh13	0	0.16	0
Rnf139	0	0.15	0
Rusc2	0	0.21	0
Scube3	0	0.11	0
Serpinb10	0	0.18	0
Sgms2	0	0.14	0
Shroom4	0	0.27	0
Slc2a12	0	0.13	0
Slc35f1	0	0.12	0
Smc2	0	0.18	0
Smurf1	0	0.15	0
Sos1	0	0.14	0
Spopl	0	0.2	0
Stk33	0	0.13	0
Stxbp5l	0	0.11	0
Syt10	0	0.15	0
Sytl2	0	0.11	0
Tcl1b4	0	0.37	0
Tdrd7	0	0.14	0
Trip12	0	0.2	0
Trpm8	0	0.24	0
Unc79	0	0.18	0
Wdhd1	0	0.2	0
Xrra1	0	0.17	0
Zbed6	0	0.22	0
Zfp869	0	0.13	0
1700066M21Rik	0	0	0.32
5330417C22Rik	0	0	0.5
Abcb5	0	0	0.14
Acot12	0	0	0.49
Aim1l	0	0	0.5
Ankrd13d	0	0	0.45

Arhgap29	0	0	0.5
Arhgap44	0	0	0.48
Aspa	0	0	0.14
Atp13a3	0	0	0.99
B020004J07Rik	0	0	0.16
Car3	0	0	0.42
Cast	0	0	0.36
Ccdc55	0	0	0.15
Cd101	0	0	0.45
Cdc25c	0	0	0.24
Cdh26	0	0	0.37
Cep250	0	0	0.46
Chl1	0	0	0.28
Cit	0	0	0.32
Cnot1	0	0	0.31
Coro1c	0	0	0.32
Crb2	0	0	0.45
Csmd3	0	0	0.33
Ctnna2	0	0	0.33
Ctsq	0	0	0.44
Cul5	0	0	0.46
Cyp2t4	0	0	0.5
Dchs1	0	0	0.5
Ddx50	0	0	0.32
Dgkz	0	0	0.46
Dmd	0	0	0.26
Dmtf1	0	0	0.47
Dnah10	0	0	0.32
Doc2a	0	0	0.48
Duoxa1	0	0	0.4
Dync2h1	0	0	0.4
Efcab6	0	0	0.24
Efnb2	0	0	0.34
Epha3	0	0	1
Ephx3	0	0	0.51
Fermt1	0	0	0.5
Fgd6	0	0	0.31
Frmd4a	0	0	0.46
Gcc2	0	0	0.46
Gcg	0	0	0.45
Gm5150	0	0	0.48
Gpr98	0	0	0.5
Gpt2	0	0	0.28
Gtl3	0	0	0.32
Hepacam2	0	0	0.24

Hexa	0	0	0.47
Hibch	0	0	0.47
Hlf	0	0	0.47
Hspa12b	0	0	0.46
Kdm4c	0	0	0.14
Klra6	0	0	0.28
Lao1	0	0	0.43
Lrig3	0	0	0.27
Lrrc52	0	0	0.66
Map2k4	0	0	0.5
Mfn2	0	0	0.45
Mfsd1	0	0	0.51
Midn	0	0	0.45
Mpdz	0	0	0.52
Myh7b	0	0	0.16
Myh8	0	0	0.5
Myo18a	0	0	0.46
Nell1	0	0	0.44
Net1	0	0	0.55
Olfr1116-ps	0	0	0.46
Olfr1263	0	0	0.47
Olfr134	0	0	0.49
Olfr1501	0	0	0.47
Olfr591	0	0	0.47
Olfr776	0	0	0.34
Olfr847	0	0	0.18
Pcdh12	0	0	0.34
Pde3a	0	0	0.22
Pnpt1	0	0	0.5
Ppp1r35	0	0	0.46
Psd4	0	0	0.32
Pten	0	0	0.35
Ptgr1	0	0	0.51
Ptprt	0	0	0.46
Rab10	0	0	0.44
Rad51d	0	0	0.37
Rimbp2	0	0	0.33
Rin2	0	0	0.44
Rps6kb2	0	0	0.48
Scn9a	0	0	0.35
Sh3yl1	0	0	0.53
Skint5	0	0	0.46
Slc12a6	0	0	0.47
Snx24	0	0	0.3
Sppl2c	0	0	0.46

Stx16	0	0	0.45
Syne2	0	0	0.44
Tas2r122	0	0	0.29
Tmem104	0	0	0.48
Tmem132d	0	0	0.3
Tmem177	0	0	0.63
Tmem2	0	0	0.49
Tomm40	0	0	0.44
Trem1	0	0	0.18
Trim71	0	0	0.5
Trip11	0	0	0.44
Tsc1	0	0	0.13
Ubap2	0	0	0.51
Ubtfl1	0	0	0.18
Vim	0	0	0.52
Wdr59	0	0	0.31
Xkr4	0	0	0.19
Zar1	0	0	0.52
Zfp341	0	0	0.53
Zfp831	0	0	0.17
Abca3	0.18	0.23	0
Atp13a5	0.66	0.97	0
Atp6v1a	0.63	0.96	0
Bcor	0.31	0.16	0
Clcn5	0.16	0.22	0
Foxb2	0.16	0.13	0
Gria1	0.18	0.13	0
Hnrnph2	0.32	0.21	0
Igsf5	0.65	0.97	0
Lrrc40	0.22	0.1	0
Pou3f3	0.15	0.12	0
Setx	0.14	0.13	0
Slc4a11	0.16	0.13	0
Sycp2	0.16	0.14	0
Topors	0.17	0.13	0
Ube2dnl2	0.33	0.26	0
Usp9y	0.99	1	0
4930451C15Rik	0.29	0	1
Ccdc14	0.13	0	0.99
Gm8693	0.95	0	0.93
Olfr656	0.2	0	0.45
Olfr820	0.13	0	0.32
Smpd4	0.3	0	1
Dpp10	0	0.22	0.66
Fat1	0	0.14	0.11

Rsf1	0	0.62	0.5

Table S2. Immune cell annotations.

Population	Abbreviation	Primary markers used for identification
Infiltrating cells	$CD45^{hi}$	$^{a}Lin^{neg}CD45.2^{hi}CD44^{pos/hi}CD49d^{pos/hi}$
Microglia	Mg	$CD45^{low/+}CD44^{low}CD49d^{low}TMEM119^{+/hi}P2RY12^{low/hi}SiglecH^{low/hi}CX3CR1^{+/hi}CD11b^{+}$
Total T cells	T cells	$^{a}Lin^{neg}CD45.2^{hi}SSC\text{-}A^{low}NK1.1^{neg}CD19^{neg}CD3^{+}$
CD8 T cells	CD8 T	$^{a}Lin^{neg}CD45.2^{hi}SSC\text{-}A^{low}NK1.1^{neg}CD19^{neg}CD3^{+}CD8^{+}CD4^{neg}$
CD4 T cells	CD4 T	$^{a}Lin^{neg}CD45.2^{hi}SSC\text{-}A^{low}NK1.1^{neg}CD19^{neg}CD3^{+}CD8^{neg}CD4^{+}$
$CD8^{+}CD4^{+}$ T cells	DP T	$^{a}Lin^{neg}CD45.2^{hi}SSC\text{-}A^{low}NK1.1^{neg}CD19^{neg}CD3^{+}CD8^{+}CD4^{+}$
$CD8^{-}CD4^{-}$ T cells	DN T	$^{a}Lin^{neg}CD45.2^{hi}SSC\text{-}A^{low}NK1.1^{neg}CD19^{neg}CD3^{+}CD8^{neg}CD4^{neg}$
Natural killer	NK	$^{a}Lin^{neg}CD45.2^{hi}SSC\text{-}A^{low}CD19^{neg}CD3^{neg}NK1.1^{hi}$
Natural killer T cells	NKT	$^{a}Lin^{neg}CD45.2^{hi}SSC\text{-}A^{low}CD19^{neg}CD3^{+}NK1.1^{hi}$
Innate lymphoid cells	ILCs	$^{a}Lin^{neg}CD45.2^{hi}SSC\text{-}A^{low}NK1.1^{neg}CD19^{neg}CD3^{neg}CD11b^{neg}CD11c^{neg}$
B cells	B cells	$^{a}Lin^{neg}CD45.2^{hi}CD3^{neg}NK1.1^{neg}CD19^{+}MHCII^{+}$
Neutrophils	Neu	$^{b}Lin^{neg}CD45.2^{hi}SSC\text{-}A^{int}CD11b^{+}Ly6C^{int}Ly6G^{+}$
Mononuclear phagocytes	Mononuclear phagocytes	$^{b}Lin^{neg}CD45.2^{hi}CD44^{+/hi}CD49d^{hi}Ly6G^{neg}CD11b^{+}$ $^{b}Lin^{neg}CD45.2^{hi}CD44^{+/hi}CD49d^{hi}Ly6G^{neg}CD11c^{+}$
Classical Monocytes	$Ly6C^{hi}$ Monocytes	$^{b}Lin^{neg}Ly6G^{neg}CX3CR1^{+}CD44^{hi}F4/80^{neg\text{-}low}CD11c^{neg}MHCII^{neg}Ly6C^{hi}$
Non-classical Monocytes	$Ly6C^{low}$ Monocytes	$^{b}Lin^{neg}Ly6G^{neg}CX3CR1^{+}CD44^{hi}F4/80^{low/int}CD11c^{low}MHCII^{neg}Ly6C^{low}$
Monocyte-derived	Monoderived	$^{b}Lin^{neg}CD45.2^{hi}Ly6G^{neg}CD11b^{int/hi}CD11c^{neg\text{-}low\text{-}int}SiglecH^{neg}CD24^{neg}MHCII^{+/hi}MertK^{pos/hi}$ $F4/80^{pos/hi}$
Dendritic cells	DC	$^{a}Lin^{neg}Ly6G^{neg}CD11c^{+}MHCII^{+}F4/80^{neg}CD24^{+}$
Dendritic cells 1	DC1	$^{a}Lin^{neg}Ly6G^{neg}CD11c^{hi}MHCII^{+}F4/80^{neg}CD11b^{neg}CD24^{hi}CD103^{hi}$
Dendritic cells 2	DC2	$^{a}Lin^{neg}Ly6G^{neg}CD11c^{+}MHCII^{hi}F4/80^{neg}CD11b^{+}CD24^{neg}CD103^{neg}$
Dendritic cells 3	DC.pop3	$^{a}Lin^{neg}Ly6G^{neg}CD11c^{+}MHCII^{+}F4/80^{neg}CD11b^{neg}CD24^{hi}CD103^{neg}$
Plasmacytoid DC	pDC	$^{a}Lin^{neg}Ly6G^{neg}CD11c^{int}MHCII^{lo}Ly6C^{+}SiglecH^{+}$

$^{a}Lin^{neg}$: $TMEM119^{neg}P2RY12^{neg}$
$^{b}Lin^{neg}$: $TMEM119^{neg}P2RY12^{neg}NK1.1^{neg}CD3^{neg}CD19^{neg}$

Table S3: CD8+ T cell cluster-defining genes.

p_val	avg_log 2FC	pct.1	pct.2	p_val_adj	cluster	cluster name	gene
1.95E-68	1.931	0.983	0.550	5.11E-64	0	sc.5	S100a6
2.54E-66	1.235	1.000	0.817	6.67E-62	0	sc.5	Cd3g
2.61E-65	1.362	1.000	0.788	6.85E-61	0	sc.5	Nkg7
9.43E-62	1.314	1.000	0.790	2.47E-57	0	sc.5	AW112010
9.58E-62	1.411	1.000	0.581	2.51E-57	0	sc.5	Cxcr6
1.55E-60	2.079	0.991	0.658	4.05E-56	0	sc.5	Ccl5
2.26E-59	1.733	0.945	0.396	5.92E-55	0	sc.5	S100a4
3.96E-59	1.364	0.766	0.162	1.04E-54	0	sc.5	Gm36723
6.75E-52	1.044	0.830	0.254	1.77E-47	0	sc.5	Fgl2
2.33E-49	1.852	0.770	0.223	6.10E-45	0	sc.5	Gzmb
2.16E-48	0.979	0.996	0.750	5.67E-44	0	sc.5	Cd8a
1.43E-47	1.160	0.689	0.175	3.75E-43	0	sc.5	Tcrg-C2
7.43E-47	1.383	0.923	0.406	1.95E-42	0	sc.5	Ccl4
6.27E-46	1.055	0.953	0.642	1.64E-41	0	sc.5	S100a11
2.05E-43	1.104	0.983	0.565	5.36E-39	0	sc.5	Id2
4.23E-43	1.288	0.932	0.633	1.11E-38	0	sc.5	Klrd1
7.42E-42	0.948	0.987	0.571	1.95E-37	0	sc.5	Rbpj
1.46E-41	0.941	0.932	0.429	3.84E-37	0	sc.5	Pdcd1
1.95E-41	1.196	0.983	0.681	5.12E-37	0	sc.5	Lgals1
1.06E-39	1.087	0.677	0.202	2.78E-35	0	sc.5	Trgv2
1.23E-37	0.933	0.783	0.292	3.24E-33	0	sc.5	Lag3
2.82E-37	0.949	0.685	0.192	7.39E-33	0	sc.5	Havcr2
2.16E-35	0.935	0.647	0.200	5.66E-31	0	sc.5	Cd200r1
3.43E-35	1.140	0.651	0.192	9.00E-31	0	sc.5	Ccl3
1.97E-33	0.941	0.877	0.467	5.16E-29	0	sc.5	Cdk6
1.02E-30	1.011	0.728	0.294	2.68E-26	0	sc.5	Prf1
7.87E-28	1.052	0.553	0.181	2.06E-23	0	sc.5	Klre1
1.80E-27	1.007	0.685	0.277	4.72E-23	0	sc.5	Ifng
1.69E-22	0.955	0.749	0.375	4.44E-18	0	sc.5	Ctla4
1.20E-16	0.956	0.677	0.419	3.14E-12	0	sc.5	Plac8
7.42E-22	1.600	0.639	0.290	1.95E-17	1	sc.3	Ly6c2
1.22E-20	0.629	0.614	0.241	3.20E-16	1	sc.3	Cxcr3
1.91E-16	0.638	0.975	0.791	5.02E-12	1	sc.3	Hcst
1.07E-15	0.617	0.772	0.425	2.82E-11	1	sc.3	Gramd3
1.96E-15	0.561	0.810	0.564	5.15E-11	1	sc.3	Smap1
1.33E-14	0.537	0.709	0.392	3.48E-10	1	sc.3	Hopx
2.46E-14	0.454	1.000	0.993	6.46E-10	1	sc.3	Rpl13a
3.79E-14	0.457	0.994	0.700	9.95E-10	1	sc.3	Ccl5

6.85E-14	0.732	0.854	0.621	1.80E-09	1	sc.3	Zfp36l2
1.04E-13	0.795	0.918	0.794	2.72E-09	1	sc.3	Itgb1
2.79E-13	0.490	1.000	0.992	7.31E-09	1	sc.3	Rps27
3.63E-13	0.593	0.962	0.844	9.52E-09	1	sc.3	Gimap4
1.11E-11	0.497	0.956	0.901	2.92E-07	1	sc.3	Ly6e
1.56E-11	0.526	1.000	0.987	4.09E-07	1	sc.3	Tmsb10
6.09E-11	0.449	0.981	0.814	1.60E-06	1	sc.3	Ptpn18
6.78E-11	0.581	0.892	0.786	1.78E-06	1	sc.3	Ifngr1
1.30E-10	0.561	0.949	0.841	3.41E-06	1	sc.3	Epsti1
2.28E-10	0.531	0.842	0.595	5.98E-06	1	sc.3	Gm2682
4.01E-10	0.490	0.880	0.626	1.05E-05	1	sc.3	Gimap7
6.25E-10	0.528	0.570	0.298	1.64E-05	1	sc.3	Gzmk
8.08E-10	0.440	0.506	0.260	2.12E-05	1	sc.3	Rtp4
1.18E-09	0.563	0.627	0.410	3.09E-05	1	sc.3	Slfn1
1.70E-09	0.451	0.709	0.513	4.46E-05	1	sc.3	Sorl1
3.38E-09	0.437	0.728	0.516	8.85E-05	1	sc.3	Sp110
4.12E-09	0.436	0.905	0.797	0.000	1	sc.3	Gimap3
1.01E-08	0.453	0.994	0.945	0.000	1	sc.3	Ms4a4b
3.58E-08	0.709	0.772	0.591	0.001	1	sc.3	Ly6a
3.98E-08	0.461	0.753	0.538	0.001	1	sc.3	Txnip
6.03E-08	0.495	0.684	0.471	0.002	1	sc.3	Slco3a1
1.31E-55	1.145	0.866	0.186	3.45E-51	2	sc.2	Cd81
1.62E-54	1.324	0.843	0.170	4.25E-50	2	sc.2	Sparc
2.40E-49	1.119	0.827	0.180	6.29E-45	2	sc.2	Sparcl1
1.28E-45	1.068	0.764	0.161	3.35E-41	2	sc.2	Ctsl
1.06E-41	1.374	0.858	0.304	2.78E-37	2	sc.2	Mt1
6.87E-40	1.173	0.835	0.272	1.80E-35	2	sc.2	Ckb
1.37E-38	1.117	0.906	0.346	3.60E-34	2	sc.2	Qk
2.72E-38	1.808	0.984	0.973	7.13E-34	2	sc.2	mt-Nd1
5.42E-37	1.498	1.000	1.000	1.42E-32	2	sc.2	mt-Co1
7.78E-37	1.540	1.000	0.984	2.04E-32	2	sc.2	mt-Nd2
1.05E-36	1.736	1.000	0.994	2.76E-32	2	sc.2	mt-Nd4
1.10E-36	1.084	0.819	0.245	2.89E-32	2	sc.2	Cd63
1.61E-36	1.578	1.000	1.000	4.21E-32	2	sc.2	mt-Atp6
2.87E-35	1.566	1.000	1.000	7.52E-31	2	sc.2	mt-Cytb
5.45E-35	1.099	0.874	0.336	1.43E-30	2	sc.2	C1qb
6.74E-35	1.676	1.000	1.000	1.77E-30	2	sc.2	mt-Co2
4.97E-33	1.568	1.000	1.000	1.30E-28	2	sc.2	mt-Co3
9.81E-33	1.282	0.984	0.682	2.57E-28	2	sc.2	Apoe
1.76E-32	1.027	0.866	0.374	4.61E-28	2	sc.2	C1qa
7.42E-32	1.477	0.992	0.846	1.95E-27	2	sc.2	Ttr
6.28E-31	1.314	0.992	0.811	1.65E-26	2	sc.2	Macf1
2.72E-26	1.213	0.992	0.954	7.14E-22	2	sc.2	AY036118

4.96E-21	1.076	0.984	0.893	1.30E-16	2	sc.2	Cst3
6.15E-21	1.237	0.969	0.667	1.61E-16	2	sc.2	Zbtb20
1.67E-20	1.218	0.992	0.978	4.38E-16	2	sc.2	Camk1d
4.60E-17	1.064	0.992	0.900	1.21E-12	2	sc.2	Elmo1
6.89E-17	1.055	0.969	0.775	1.81E-12	2	sc.2	Gphn
4.70E-15	1.165	0.843	0.621	1.23E-10	2	sc.2	Nr3c1
9.94E-15	1.090	0.945	0.868	2.61E-10	2	sc.2	mt-Nd5
1.21E-10	1.043	0.976	0.882	3.17E-06	2	sc.2	Xist
#######	2.066	0.886	0.043	1.15E-109	3	sc.1	Sell
1.23E-90	1.827	0.927	0.111	3.23E-86	3	sc.1	Cmah
2.59E-89	1.253	0.740	0.035	6.78E-85	3	sc.1	Ccr7
2.08E-84	2.628	0.984	0.209	5.45E-80	3	sc.1	Lef1
1.12E-83	2.250	0.959	0.139	2.93E-79	3	sc.1	Klf2
1.74E-77	1.778	0.967	0.188	4.55E-73	3	sc.1	Tcf7
1.28E-73	2.291	0.943	0.220	3.36E-69	3	sc.1	Satb1
1.62E-65	1.349	0.862	0.150	4.24E-61	3	sc.1	S1pr1
1.66E-65	1.829	0.935	0.241	4.35E-61	3	sc.1	Txk
1.12E-64	1.471	0.837	0.139	2.95E-60	3	sc.1	Klf3
3.84E-60	1.448	0.959	0.220	1.01E-55	3	sc.1	Aff3
2.27E-58	1.832	0.821	0.185	5.95E-54	3	sc.1	Fam241a
1.24E-55	1.273	0.854	0.166	3.26E-51	3	sc.1	Slamf6
1.78E-53	1.676	0.951	0.301	4.68E-49	3	sc.1	Bach2
1.67E-49	1.126	1.000	1.000	4.37E-45	3	sc.1	Rps29
5.83E-49	1.556	0.984	0.710	1.53E-44	3	sc.1	Foxp1
3.10E-47	1.844	0.927	0.391	8.12E-43	3	sc.1	Il7r
2.97E-46	1.667	0.967	0.483	7.78E-42	3	sc.1	Ripor2
9.54E-46	1.450	0.870	0.231	2.50E-41	3	sc.1	Fgf13
3.22E-45	1.426	0.943	0.337	8.45E-41	3	sc.1	Emb
7.15E-44	1.712	0.862	0.323	1.88E-39	3	sc.1	Sidt1
8.78E-44	1.197	0.919	0.421	2.30E-39	3	sc.1	Dgka
5.35E-43	1.623	0.992	0.579	1.40E-38	3	sc.1	Gm2682
1.00E-41	1.081	0.992	0.994	2.62E-37	3	sc.1	Rps19
3.64E-40	1.329	0.764	0.236	9.55E-36	3	sc.1	Rras2
1.96E-38	1.346	0.902	0.380	5.14E-34	3	sc.1	Scml4
1.56E-34	1.231	0.959	0.642	4.09E-30	3	sc.1	Crlf3
1.80E-33	1.154	1.000	0.967	4.72E-29	3	sc.1	Arhgap15
2.79E-31	1.080	0.959	0.616	7.32E-27	3	sc.1	Ssh2
1.23E-26	1.110	0.902	0.419	3.23E-22	3	sc.1	Gramd3
4.72E-47	3.287	0.838	0.166	1.24E-42	4	sc.4	Xcl1
1.73E-34	1.333	0.865	0.236	4.53E-30	4	sc.4	Cd160
2.83E-17	1.037	0.878	0.476	7.41E-13	4	sc.4	Ybx3
9.62E-14	0.921	0.716	0.338	2.52E-09	4	sc.4	Bcl2a1d
3.24E-12	1.158	0.716	0.407	8.50E-08	4	sc.4	Il18r1

1.53E-11	0.918	0.649	0.292	4.02E-07	4	sc.4	Tnfrsf9
3.20E-11	0.729	0.635	0.276	8.40E-07	4	sc.4	Il18rap
3.24E-11	0.584	0.689	0.338	8.49E-07	4	sc.4	Fam162a
5.44E-11	0.800	0.649	0.294	1.43E-06	4	sc.4	Alcam
6.70E-11	0.587	0.878	0.540	1.76E-06	4	sc.4	Elk3
1.05E-10	0.846	0.622	0.302	2.74E-06	4	sc.4	Phactr2
2.15E-10	0.645	0.986	0.809	5.63E-06	4	sc.4	Cd8a
2.55E-10	0.964	0.959	0.758	6.69E-06	4	sc.4	Ifi27l2a
2.85E-10	0.746	0.824	0.496	7.48E-06	4	sc.4	Bcl2a1b
1.11E-09	1.041	0.797	0.499	2.90E-05	4	sc.4	St6galnac3
1.19E-09	0.759	0.838	0.562	3.12E-05	4	sc.4	Nfat5
1.22E-09	0.627	0.757	0.417	3.21E-05	4	sc.4	Cd44
1.53E-09	0.667	0.838	0.512	4.01E-05	4	sc.4	Adamts6
2.57E-09	0.611	0.757	0.411	6.74E-05	4	sc.4	Lag3
4.27E-09	0.679	0.986	0.863	1.119E-04	4	sc.4	Rabgap1l
4.79E-09	0.704	0.932	0.675	1.255E-04	4	sc.4	Rbpj
7.63E-09	0.589	1.000	0.993	2.001E-04	4	sc.4	Hsp90ab1
8.38E-09	0.795	0.608	0.285	2.198E-04	4	sc.4	Rgs16
9.43E-09	0.789	0.649	0.385	2.474E-04	4	sc.4	Nrp1
2.13E-08	0.595	0.959	0.812	5.592E-04	4	sc.4	Eif5a
3.04E-08	0.581	0.824	0.592	7.972E-04	4	sc.4	Trps1
3.80E-08	0.684	0.986	0.802	9.962E-04	4	sc.4	Itgb1
1.80E-07	0.603	0.568	0.297	4.729E-03	4	sc.4	Gpm6b
2.91E-07	0.600	0.824	0.537	7.634E-03	4	sc.4	Mdfic
7.11E-96	3.221	1.000	0.043	1.87E-91	5	sc.6	Hist1h3c
1.57E-94	3.143	0.974	0.040	4.11E-90	5	sc.6	Hist1h2ab
5.21E-78	2.336	1.000	0.063	1.37E-73	5	sc.6	Birc5
7.01E-76	2.096	1.000	0.066	1.84E-71	5	sc.6	Cdca8
1.60E-72	2.753	1.000	0.074	4.20E-68	5	sc.6	Pclaf
3.11E-72	2.367	0.974	0.067	8.16E-68	5	sc.6	Nusap1
7.96E-69	2.104	0.921	0.064	2.09E-64	5	sc.6	Hist1h3f
7.78E-65	2.006	0.974	0.081	2.04E-60	5	sc.6	Kif11
4.16E-56	2.658	0.974	0.117	1.09E-51	5	sc.6	Hist1h3e
2.28E-55	2.500	0.789	0.054	5.99E-51	5	sc.6	Cenpf
3.95E-52	2.195	0.974	0.117	1.04E-47	5	sc.6	Prc1
1.04E-49	2.671	0.816	0.074	2.73E-45	5	sc.6	Ube2c
5.00E-49	2.215	0.974	0.142	1.31E-44	5	sc.6	Hist1h4h
5.70E-49	2.465	0.974	0.148	1.50E-44	5	sc.6	Hist2h2ac
7.13E-48	4.304	1.000	0.169	1.87E-43	5	sc.6	Hist1h1b
5.15E-46	2.696	1.000	0.165	1.35E-41	5	sc.6	Mki67
1.73E-44	4.493	1.000	0.191	4.55E-40	5	sc.6	Hist1h2ae
2.73E-40	1.990	1.000	0.209	7.16E-36	5	sc.6	Smc2
1.39E-38	2.888	1.000	0.229	3.64E-34	5	sc.6	Stmn1

7.12E-37	2.137	0.947	0.185	1.87E-32	5	sc.6	Tubb4b
7.40E-37	3.210	1.000	0.264	1.94E-32	5	sc.6	Top2a
8.30E-37	2.115	0.921	0.183	2.18E-32	5	sc.6	H2afx
6.29E-36	4.842	1.000	0.290	1.65E-31	5	sc.6	Hist1h2ap
1.43E-31	2.358	1.000	0.365	3.76E-27	5	sc.6	Tuba1b
7.01E-29	3.416	1.000	0.497	1.84E-24	5	sc.6	Hist1h4d
6.92E-27	2.571	1.000	0.540	1.82E-22	5	sc.6	Hist1h1e
6.78E-26	2.500	1.000	0.656	1.78E-21	5	sc.6	Tubb5
3.00E-25	3.335	1.000	0.706	7.87E-21	5	sc.6	Hmgb2
5.01E-25	1.976	1.000	0.494	1.32E-20	5	sc.6	Ube2s
2.55E-24	2.124	1.000	0.859	6.69E-20	5	sc.6	H2afz

Table S4: CD4+ T cell cluster-defining genes.

p_val	avg_log2FC	pct.1	pct.2	p_val_adj	cluster	cluster name	gene
2.70E-74	2.4658	0.972	0.382	7.09E-70	0	CD4.sc1	Lef1
4.65E-70	2.2771	0.983	0.299	1.22E-65	0	CD4.sc1	Klf2
1.81E-66	2.4356	0.932	0.312	4.75E-62	0	CD4.sc1	Satb1
2.37E-62	1.4292	0.864	0.151	6.21E-58	0	CD4.sc1	Sell
2.69E-62	2.1106	1	0.497	7.04E-58	0	CD4.sc1	Gm2682
4.68E-62	2.0159	0.994	0.59	1.23E-57	0	CD4.sc1	Foxp1
9.41E-62	1.8122	0.909	0.246	2.47E-57	0	CD4.sc1	Txk
1.29E-58	1.5158	0.938	0.281	3.39E-54	0	CD4.sc1	S1pr1
2.65E-58	1.92	0.926	0.354	6.95E-54	0	CD4.sc1	Bach2
6.09E-55	1.0629	1	1	1.60E-50	0	CD4.sc1	Rps29
2.41E-52	0.9964	0.67	0.078	6.33E-48	0	CD4.sc1	Pik3ip1
2.75E-51	1.5112	0.926	0.374	7.20E-47	0	CD4.sc1	Tcf7
5.81E-48	1.1393	0.71	0.133	1.52E-43	0	CD4.sc1	Actn1
9.80E-48	1.4496	0.972	0.698	2.57E-43	0	CD4.sc1	Crlf3
2.28E-47	1.2499	0.812	0.214	5.99E-43	0	CD4.sc1	Klf3
5.35E-46	1.1001	0.591	0.058	1.40E-41	0	CD4.sc1	Rflnb
3.98E-45	1.4041	0.972	0.636	1.04E-40	0	CD4.sc1	Ripor2
1.43E-44	1.3212	1	0.965	3.74E-40	0	CD4.sc1	Arhgap15
2.40E-44	1.6137	0.506	0.03	6.29E-40	0	CD4.sc1	Igfbp4
8.62E-44	1.143	0.545	0.048	2.26E-39	0	CD4.sc1	St8sia6
6.04E-43	1.0328	0.71	0.136	1.58E-38	0	CD4.sc1	Ccr7
1.23E-42	1.1636	0.932	0.497	3.23E-38	0	CD4.sc1	Dgka
1.35E-40	1.2443	0.858	0.364	3.55E-36	0	CD4.sc1	Scml4
9.21E-40	1.3161	0.778	0.249	2.42E-35	0	CD4.sc1	Cmah
6.09E-35	1.2343	0.835	0.397	1.60E-30	0	CD4.sc1	Tmem71
1.56E-34	1.1863	0.955	0.678	4.09E-30	0	CD4.sc1	Prkcq
8.82E-34	1.0426	0.977	0.907	2.31E-29	0	CD4.sc1	Rapgef6
1.68E-33	1.1313	0.761	0.266	4.41E-29	0	CD4.sc1	St6gal1
2.80E-27	1.0327	0.943	0.751	7.34E-23	0	CD4.sc1	Ikzf1
1.48E-26	1.0186	0.688	0.271	3.88E-22	0	CD4.sc1	Ugcg
1.45E-69	2.6831	0.981	0.296	3.79E-65	1	CD4.sc5	Ikzf2
6.35E-65	1.5118	0.786	0.077	1.66E-60	1	CD4.sc5	Foxp3
6.43E-53	1.8706	0.78	0.14	1.69E-48	1	CD4.sc5	Tnfrsf9
6.99E-47	1.6338	0.761	0.154	1.83E-42	1	CD4.sc5	Il2ra
2.77E-46	1.833	0.95	0.361	7.26E-42	1	CD4.sc5	Tnfrsf4
1.39E-45	1.5504	0.969	0.513	3.65E-41	1	CD4.sc5	Tnfrsf18
3.04E-44	1.208	0.629	0.087	7.97E-40	1	CD4.sc5	Neb
1.90E-38	1.6722	0.962	0.448	5.00E-34	1	CD4.sc5	Ctla4
1.32E-35	1.4683	0.78	0.318	3.46E-31	1	CD4.sc5	Arl5a
4.44E-35	1.3279	0.824	0.34	1.16E-30	1	CD4.sc5	Izumo1r
2.70E-32	1.0323	0.547	0.089	7.08E-28	1	CD4.sc5	Itgb8

3.08E-32	1.1847	0.874	0.414	8.09E-28	1	CD4.sc5	Capg
7.62E-31	1.0991	0.792	0.318	2.00E-26	1	CD4.sc5	Tnfrsf1b
4.00E-30	1.0045	0.906	0.407	1.05E-25	1	CD4.sc5	Il2rb
7.21E-29	1.3823	0.824	0.402	1.89E-24	1	CD4.sc5	Itgav
1.83E-28	1.1439	0.855	0.508	4.79E-24	1	CD4.sc5	Gimap7
1.02E-27	1.2783	0.736	0.323	2.67E-23	1	CD4.sc5	Ighm
4.78E-27	1.3767	0.975	0.848	1.25E-22	1	CD4.sc5	Ifi27l2a
1.40E-26	0.9938	0.906	0.571	3.66E-22	1	CD4.sc5	Pim1
2.49E-23	1.0318	0.881	0.525	6.53E-19	1	CD4.sc5	Samsn1
3.30E-21	1.1678	0.717	0.337	8.66E-17	1	CD4.sc5	Hopx
2.02E-20	0.9867	0.811	0.431	5.29E-16	1	CD4.sc5	Maf
6.45E-20	1.0151	0.969	0.798	1.69E-15	1	CD4.sc5	Rabgap1l
8.10E-19	1.0454	0.912	0.713	2.12E-14	1	CD4.sc5	Sdf4
1.59E-18	1.1913	0.818	0.453	4.17E-14	1	CD4.sc5	S100a6
1.14E-17	0.9536	0.566	0.214	3.00E-13	1	CD4.sc5	Iigp1
1.60E-17	0.9873	0.748	0.373	4.21E-13	1	CD4.sc5	Odc1
1.91E-15	0.9527	0.893	0.672	5.01E-11	1	CD4.sc5	Ly6a
2.28E-15	0.9349	0.881	0.646	5.98E-11	1	CD4.sc5	Icos
2.97E-12	0.9491	0.836	0.677	7.80E-08	1	CD4.sc5	Vim
1.04E-13	0.69	0.672	0.345	2.73E-09	2	CD4.sc2	Arhgap26
6.88E-09	0.5019	0.513	0.262	0.00018	2	CD4.sc2	Cd63
1.06E-07	0.6665	0.807	0.582	0.00277	2	CD4.sc2	Itgb1
2.40E-07	0.7834	0.756	0.582	0.006293	2	CD4.sc2	Emb
4.60E-07	0.635	0.697	0.519	0.012059	2	CD4.sc2	Pde7a
6.15E-07	0.4858	0.958	0.879	0.016137	2	CD4.sc2	Celf2
2.18E-06	0.6497	0.723	0.569	0.05709	2	CD4.sc2	Btg2
3.53E-06	0.7988	0.605	0.378	0.092528	2	CD4.sc2	C1qb
4.44E-42	2.1955	0.965	0.203	1.16E-37	3	CD4.sc3	Cxcr6
6.45E-30	2.1697	0.965	0.311	1.69E-25	3	CD4.sc3	Nkg7
3.56E-25	3.0164	0.895	0.331	9.35E-21	3	CD4.sc3	Ccl5
8.47E-24	1.6638	0.544	0.085	2.22E-19	3	CD4.sc3	Ifng
1.25E-21	1.1158	0.579	0.104	3.29E-17	3	CD4.sc3	Tmem163
1.65E-21	1.5962	0.912	0.427	4.33E-17	3	CD4.sc3	Id2
9.99E-21	1.3405	0.86	0.294	2.62E-16	3	CD4.sc3	Pdcd1
2.02E-18	1.081	1	0.954	5.31E-14	3	CD4.sc3	Cd3g
8.21E-18	1.2564	0.93	0.538	2.15E-13	3	CD4.sc3	Rbpj
5.91E-17	1.6558	0.877	0.414	1.55E-12	3	CD4.sc3	S100a4
6.78E-17	1.3834	1	0.814	1.78E-12	3	CD4.sc3	AW112010
2.36E-15	1.0615	0.825	0.346	6.20E-11	3	CD4.sc3	Hip1
2.96E-15	1.3437	0.772	0.304	7.78E-11	3	CD4.sc3	Dusp2
9.25E-15	0.8408	0.684	0.244	2.43E-10	3	CD4.sc3	Tnfsf10
1.25E-14	1.9371	0.509	0.13	3.27E-10	3	CD4.sc3	Ccl4
4.34E-14	0.9849	0.561	0.159	1.14E-09	3	CD4.sc3	Rgs16
4.95E-14	1.3471	0.86	0.453	1.30E-09	3	CD4.sc3	Rgs1
7.77E-14	1.032	0.947	0.578	2.04E-09	3	CD4.sc3	AU020206

6.53E-13	1.2485	0.947	0.511	1.71E-08	3	CD4.sc3	S100a6
1.62E-12	0.9067	1	0.662	4.26E-08	3	CD4.sc3	S100a11
5.45E-12	0.8826	1	0.973	1.43E-07	3	CD4.sc3	Cd52
6.76E-12	0.9882	0.684	0.273	1.77E-07	3	CD4.sc3	Bhlhe40
1.43E-11	0.972	0.982	0.677	3.75E-07	3	CD4.sc3	Lgals1
7.31E-11	0.7638	0.877	0.507	1.92E-06	3	CD4.sc3	Gng2
6.32E-10	0.7972	0.544	0.193	1.66E-05	3	CD4.sc3	Lgals3
7.11E-10	0.9605	0.807	0.472	1.86E-05	3	CD4.sc3	Cd226
7.43E-10	0.7606	1	0.901	1.95E-05	3	CD4.sc3	Arl6ip1
7.47E-08	1.1071	0.649	0.338	0.001958	3	CD4.sc3	Ctla2a
1.15E-07	0.7851	0.965	0.865	0.003019	3	CD4.sc3	Sub1
1.62E-07	0.7853	0.649	0.354	0.004261	3	CD4.sc3	Ctsw
6.60E-39	1.395	0.775	0.079	1.73E-34	4	CD4.sc4	Gm49180
1.69E-29	2.5873	0.95	0.257	4.44E-25	4	CD4.sc4	Tnfsf8
1.13E-25	1.6995	0.8	0.157	2.96E-21	4	CD4.sc4	Tnfsf11
7.07E-20	1.4357	0.875	0.272	1.85E-15	4	CD4.sc4	Bhlhe40
7.14E-20	1.9977	0.925	0.378	1.87E-15	4	CD4.sc4	Eea1
1.70E-17	1.7789	0.975	0.515	4.47E-13	4	CD4.sc4	Trps1
2.27E-17	1.5468	0.825	0.303	5.96E-13	4	CD4.sc4	Tbc1d4
5.60E-17	1.6436	0.95	0.446	1.47E-12	4	CD4.sc4	Gm15283
6.28E-17	1.3698	0.75	0.2	1.65E-12	4	CD4.sc4	Mir155hg
1.03E-16	1.4134	0.825	0.281	2.71E-12	4	CD4.sc4	Phactr2
9.60E-16	1.5897	0.95	0.566	2.52E-11	4	CD4.sc4	Arap2
4.14E-15	1.5608	0.95	0.691	1.09E-10	4	CD4.sc4	Hif1a
1.06E-13	1.1862	0.8	0.264	2.77E-09	4	CD4.sc4	Kcnq5
1.57E-13	1.1136	0.675	0.202	4.12E-09	4	CD4.sc4	Cd200
4.69E-13	1.1912	0.925	0.537	1.23E-08	4	CD4.sc4	Itpr1
5.07E-13	1.3477	0.9	0.446	1.33E-08	4	CD4.sc4	Odc1
7.10E-13	1.1081	0.925	0.545	1.86E-08	4	CD4.sc4	Jak2
7.71E-13	1.2137	0.95	0.624	2.02E-08	4	CD4.sc4	Ostf1
2.00E-12	1.0762	0.9	0.478	5.24E-08	4	CD4.sc4	Etv6
2.17E-12	1.2973	0.975	0.547	5.69E-08	4	CD4.sc4	Rbpj
2.60E-12	1.1922	0.875	0.459	6.82E-08	4	CD4.sc4	Cd82
5.42E-12	1.2641	0.95	0.755	1.42E-07	4	CD4.sc4	Sdf4
1.69E-11	1.0617	0.95	0.605	4.42E-07	4	CD4.sc4	Itgb1
1.73E-11	1.288	0.625	0.221	4.54E-07	4	CD4.sc4	Gpm6b
2.00E-11	1.0825	0.925	0.479	5.24E-07	4	CD4.sc4	Nfat5
1.60E-10	1.195	0.9	0.513	4.19E-06	4	CD4.sc4	Slamf6
1.80E-10	1.3157	0.975	0.717	4.71E-06	4	CD4.sc4	Stat4
2.92E-10	1.1008	0.775	0.375	7.67E-06	4	CD4.sc4	Kdm2b
7.90E-09	1.1523	0.95	0.764	0.000207	4	CD4.sc4	Prkca
3.18E-07	1.1287	0.675	0.363	0.008349	4	CD4.sc4	Nrp1
1.43E-74	2.8862	1	0.031	3.76E-70	5	CD4.sc6	Hist1h2ab
6.56E-68	2.311	1	0.038	1.72E-63	5	CD4.sc6	Nusap1
5.05E-63	1.9574	0.957	0.038	1.33E-58	5	CD4.sc6	Tpx2

5.27E-61	2.8896	1	0.049	1.38E-56	5	CD4.sc6	Hist1h3c
3.61E-60	2.0618	1	0.049	9.48E-56	5	CD4.sc6	Kif11
1.30E-53	2.0623	0.87	0.038	3.41E-49	5	CD4.sc6	Cenpf
4.48E-49	2.1381	0.957	0.062	1.17E-44	5	CD4.sc6	Cdca8
2.30E-47	2.8141	1	0.08	6.02E-43	5	CD4.sc6	Pclaf
2.46E-45	2.1941	0.913	0.064	6.45E-41	5	CD4.sc6	Birc5
3.76E-43	2.3881	0.913	0.067	9.87E-39	5	CD4.sc6	Ube2c
1.27E-40	2.1334	1	0.098	3.34E-36	5	CD4.sc6	Hist1h4h
4.34E-40	2.2946	0.957	0.089	1.14E-35	5	CD4.sc6	Prc1
8.40E-38	2.1106	1	0.111	2.20E-33	5	CD4.sc6	Diaph3
1.16E-37	4.2177	1	0.122	3.05E-33	5	CD4.sc6	Hist1h1b
2.68E-35	2.3752	0.957	0.116	7.03E-31	5	CD4.sc6	Hist1h3e
4.67E-34	3.9954	1	0.142	1.22E-29	5	CD4.sc6	Hist1h2ae
5.19E-34	3.1412	1	0.138	1.36E-29	5	CD4.sc6	Mki67
6.56E-28	2.124	0.957	0.16	1.72E-23	5	CD4.sc6	Hist2h2ac
2.16E-27	3.3427	1	0.205	5.66E-23	5	CD4.sc6	Top2a
2.22E-26	2.0812	1	0.212	5.81E-22	5	CD4.sc6	Smc2
2.63E-25	1.9485	0.957	0.16	6.91E-21	5	CD4.sc6	Rad51b
1.17E-24	4.4356	1	0.247	3.06E-20	5	CD4.sc6	Hist1h2ap
1.38E-23	2.9391	1	0.26	3.62E-19	5	CD4.sc6	Stmn1
1.53E-19	2.034	1	0.365	4.01E-15	5	CD4.sc6	Lmnb1
8.97E-19	2.045	1	0.408	2.35E-14	5	CD4.sc6	Tuba1b
2.74E-18	3.2597	1	0.497	7.18E-14	5	CD4.sc6	Hist1h4d
8.10E-17	2.4069	1	0.675	2.13E-12	5	CD4.sc6	Tubb5
8.39E-16	3.1063	1	0.793	2.20E-11	5	CD4.sc6	Hmgb2
1.23E-15	2.6079	1	0.833	3.23E-11	5	CD4.sc6	H2afz
3.83E-15	2.2363	1	0.519	1.01E-10	5	CD4.sc6	Hist1h1e

Table S5: List of genes associated with each metaprogram.

MP1	MP2	MP3	MP4
2010110K18Rik	4930533B01Rik	1700006J14Rik	0610005C13Rik
2810408I11Rik	9530026P05Rik	1700025G04Rik	4930405A10Rik
4930503L19Rik	AC149090.1	6030407O03Rik	4930453C13Rik
4930558J18Rik	Acacb	8030451A03Rik	9330175E14Rik
4930579G24Rik	Acvr1c	Abhd2	9930111J21Rik2
5430427M07Rik	Appl2	Abtb2	A530032D15Rik
Alms1	Bhlhe41	Acss3	A730085K08Rik
Anapc15	Bnc2	Adamts1	A930037H05Rik
Ankle1	C1ql3	Adamts12	AC168977.2
Anln	Cdh1	Adamts5	Aida
Anp32e	Cdk15	Adgrl2	Ankrd34a
Arhgap11a	Cdk2	Ahr	Apol6
Arhgap19	Cfap54	Aldh1a3	Apol9a
Arhgap33	Chsy3	Ano6	Apol9b
Arhgef39	Daam1	Antxr1	Atp8b4
Asf1b	Dennd5b	Aopep	Axl
Aspm	Disp1	Apobec2	B2m
Aspn	Ehbp1	Aqp1	Batf2
Atad2	Eps8	Arhgap10	Bst2
Atad5	Fmn1	Arhgap24	C1ra
Aunip	Gk	Arhgap29	Casp12
Aurka	Gm13963	Arih1	Ccl2
Aurkb	Gm2115	Arl15	Cfap100
BC030867	Lyst	Atp2b4	Cfb
BC055324	Man1a	Atxn1	Clec2d
Bard1	Man2a1	Baiap2l1	Cmpk2
Batf3	Met	Bcar3	Csf1
Baz1b	Mgat5	Bcas3	Csprs
Birc5	Nceh1	Bche	Csta2
Blm	Nedd4l	Bgn	Cxcl10
Bora	Nhs	C030034L19Rik	Cxcl9
Brca1	Oca2	Cacna1d	Ddx58
Brca2	Osbpl6	Cacnb3	Ddx60
Brd8	Padi2	Cadps	Dhx58
Brip1	Pde10a	Cblb	Dtx3l
Bub1	Ppargc1a	Cdk14	Eif2ak2
Bub1b	Ralgapa2	Cdk6	F830016B08Rik
C230066G23Rik	Sfi1	Col15a1	Flacc1
Camk2n2	Slc24a4	Col28a1	Gbp10
Casp8ap2	Slc7a5	Col3a1	Gbp2
Cbx5	St3gal6	Col5a2	Gbp3
Ccdc18	Sytl2	Col6a1	Gbp4
Ccdc34	Tex2	Col6a2	Gbp5
Ccdc77	Tmod1	Col8a1	Gbp6
Cchcr1	Tspan5	Cped1	Gbp7
Ccna2	Tyr	Cspg4	Gbp8

Ccnb1	Tyrp1	Ctnnal1	Gbp9
Ccnb2	Ubl3	Dact1	Gm10827
Ccne1		Diaph2	Gm11747
Ccne2		Dip2c	Gm12185
Ccnf		Dkk2	Gm13822
Ccsap		Dmd	Gm15893
Cdc20		Dock10	Gm19684
Cdc25b		Dst	Gm20559
Cdc25c		Eefsec	Gm26789
Cdc45		Efna5	Gm4070
Cdc6		Efnb1	Gm42517
Cdc7		Egflam	Gm43727
Cdca2		Eln	Gm44091
Cdca3		Etv5	Gm44148
Cdca5		Ext1	Gm4841
Cdca7		Fam110b	Gm4951
Cdca7l		Fam178b	Gm50237
Cdca8		Farp1	Gm5148
Cdk1		Fgfr1	Gm7030
Cdkn2d		Fign	Gm8773
Cdkn3		Fkbp5	Gpr149
Cdt1		Frmd6	Gpr65
Cenpa		Gli3	Gvin1
Cenpc1		Gm13919	H2-D1
Cenpe		Gm20754	H2-K1
Cenpf		Gm35188	H2-Q10
Cenph		Gm4117	H2-Q4
Cenpi		Gnaq	H2-T22
Cenpk		Hapln1	H2-T23
Cenpl		Hdac9	Herc6
Cenpm		Hivep2	Ifi203
Cenpn		Hmga2	Ifi204
Cenpp		Hs2st1	Ifi205
Cenpq		Hspb2	Ifi206
Cenps		Htr2a	Ifi207
Cenpu		Ica1	Ifi211
Cenpw		Igfbp4	Ifi27
Cep128		Il1rap	Ifi35
Cep192		Insr	Ifi44
Cep295		Itgbl1	Ifi47
Cep55		Itprid2	Ifih1
Cep57l1		Jmjd1c	Ifit1
Cep72		Kank4	Ifit2
Cep89		Kcnn2	Ifit3
Cfap97d2		Kif13a	Ifit3b
Cgas		Kif26b	Ifitm3
Chaf1a		Klf4	Igtp
Chaf1b		L1cam	Iigp1
Chek1		Lama4	Irf1

Chek2		Large1	Irf7
Chgb		Ldlrad3	Irgm1
Chtf18		Lgr4	Irgm2
Cip2a		Limch1	Isg15
Cit		Lmcd1	Isg20
Ckap2		Lpar3	Ky
Ckap2l		Lrch1	Lgals9
Ckap5		Lrch3	Lrfn1
Cks1b		Lrp1	Ly6e
Cks2		Maml2	Map3k19
Clspn		Map2	Mlkl
Cmc2		Map4	Mndal
Cnih2		Map4k3	Nlrc5
Cntrob		Mcam	Nmi
D430018E03Rik		Megf10	Oas1a
Dbf4		Mgp	Oas1g
Dcdc2a		Mir100hg	Oas2
Dck		Mllt3	Oas3
Dctpp1		Moxd1	Oasl1
Ddias		Mpz	Oasl2
Ddx11		Myo5b	Olfr56
Dek		Myof	Parp10
Depdc1a		Nav3	Parp11
Depdc1b		Ndst3	Parp12
Dhfr		Neat1	Parp14
Diaph3		Nebl	Parp9
Dlgap5		Nes	Phf11a
Dna2		Ngfr	Phf11b
Dnaaf2		Nhsl1	Phf11d
Dnajc9		Nxn	Pml
Dnmt1		P3h2	Psmb10
Dnph1		Pam	Psmb8
Dscc1		Pcdh9	Psmb9
Dsn1		Pcgf5	Psme1
Dtl		Pcsk6	Psme2
Dtymk		Pdgfb	Rnf19b
Dut		Pdgfra	Rnf213
Dynlt1a		Pdgfrb	Rsad2
Dynlt1f		Pdgfrl	Rtp4
E2f1		Pdlim4	Samd9l
E2f2		Pdlim5	Samhd1
E2f7		Pdzrn3	Slc2a6
E2f8		Pitpnc1	Slfn8
Ect2		Plcb1	Slfn9
Efcab11		Plekha6	Socs1
Eldr		Plpp1	Sp100
Eme1		Ppp1r1c	Sp110
Emp1		Prelp	Sp140
Ercc6l		Ptpn13	Stat1

Eri1		Ptprj	Stat2
Eri2		Rab27b	Styk1
Esco2		Ramp3	Tap1
Espl1		Rapgef2	Tap2
Exo1		Raph1	Tapbp
Exosc8		Rasgrp2	Tapbpl
Ezh2		Rbms1	Tgtp1
Fam111a		Rere	Tgtp2
Fam83d		Rgs16	Tnfsf10
Fanca		Rnd3	Tomm6os
Fancb		Robo1	Tor3a
Fancd2		Robo2	Trafd1
Fanci		Rock2	Trim12a
Fbxo48		Ror1	Trim12c
Fbxo5		S100a6	Trim21
Fen1		Samd4	Trim25
Fignl1		Samd5	Trim30a
Fkbp2		Sdc3	Trim34a
Fn3k		Sec14l5	Ube2l6
Foxg1		Sema3a	Usp18
Foxm1		Sema3b	Wnt2b
Fzr1		Sema5a	Xaf1
G2e3		Sema6a	Xdh
Gabrb3		Serpinf1	Ypel4
Gas2l3		Serping1	Zbp1
Gemin6		Sertad4	Znfx1
Gen1		Sh3rf1	
Gins1		Sipa1l1	
Gins2		Sipa1l3	
Gins3		Slc35f1	
Gins4		Slc9a3r2	
Gm14091		Sntb1	
Gm20628		Sorcs2	
Gm20667		Taf4b	
Gm3550		Tanc1	
Gm38037		Tbck	
Gm41555		Tcf20	
Gm42031		Tcim	
Gm42047		Tead1	
Gm44238		Tecrl	
Gm47207		Tenm3	
Gm4737		Tfap2b	
Gm48646		Thbs2	
Gm49014		Thsd4	
Gm550		Tiam2	
Gmnn		Tln2	
Gpsm2		Tnc	
Grm1		Trio	
Gtse1		Tslp	

H2afx		Ttc39b	
H2afz		Ube2e2	
Haspin		Wnt4	
Hat1		Wnt6	
Haus4		Xirp1	
Haus6		Zbtb38	
Haus8		Zeb1	
Hdgf		Zfc3h1	
Hells		Zfp532	
Hid1			
Hirip3			
Hist1h1a			
Hist1h1b			
Hist1h1c			
Hist1h1d			
Hist1h1e			
Hist1h1t			
Hist1h2ab			
Hist1h2ac			
Hist1h2ad			
Hist1h2ae			
Hist1h2af			
Hist1h2ag			
Hist1h2ah			
Hist1h2ai			
Hist1h2ak			
Hist1h2an			
Hist1h2ap			
Hist1h2bb			
Hist1h2be			
Hist1h2bf			
Hist1h2bg			
Hist1h2bh			
Hist1h2bj			
Hist1h2bk			
Hist1h2bl			
Hist1h2bm			
Hist1h2bn			
Hist1h2bp			
Hist1h2br			
Hist1h3a			
Hist1h3b			
Hist1h3c			
Hist1h3e			
Hist1h3f			
Hist1h3g			
Hist1h3h			
Hist1h3i			
Hist1h4a			

Hist1h4b			
Hist1h4c			
Hist1h4d			
Hist1h4f			
Hist1h4h			
Hist1h4j			
Hist1h4k			
Hist1h4n			
Hist2h2aa1			
Hist2h2ab			
Hist2h2ac			
Hist2h2bb			
Hist2h3b			
Hjurp			
Hmgb2			
Hmgb3			
Hmgn2			
Hmgn5			
Hmgxb4			
Hmmr			
Hmx2			
Hyls1			
Il1rapl2			
Impa2			
Incenp			
Iqgap3			
Jpt1			
Kctd18			
Kif11			
Kif14			
Kif15			
Kif18a			
Kif18b			
Kif20a			
Kif20b			
Kif22			
Kif23			
Kif24			
Kif2c			
Kif4			
Kifc1			
Kifc5b			
Knl1			
Knstrn			
Kntc1			
Kpna2			
Lbr			
Lig1			
Lin54			

Lin9			
Lmnb1			
Lockd			
Lrfn1			
Lrr1			
Lsm2			
Lsm5			
Mad2l1			
Mastl			
Mcm10			
Mcm2			
Mcm3			
Mcm4			
Mcm5			
Mcm6			
Mcm7			
Mdc1			
Melk			
Mis18a			
Mis18bp1			
Mki67			
Mlf1			
Mms22l			
Mnd1			
Mns1			
Mtbp			
Mtfr2			
Mthfd2			
Mxd3			
Myb			
Mybl1			
Mybl2			
Nasp			
Ncapd2			
Ncapd3			
Ncapg			
Ncapg2			
Ncaph			
Ndc1			
Ndc80			
Nde1			
Neil3			
Nek2			
Nell1			
Nemp1			
Neurl1b			
Nfatc2ip			
Nmral1			
Nrm			

Nsd2			
Nsl1			
Nt5dc2			
Nucks1			
Nuf2			
Nup107			
Nup155			
Nup205			
Nup35			
Nup37			
Nup43			
Nup85			
Nusap1			
Nxt1			
Odf2			
Ogn			
Oip5			
Omd			
Orc6			
Otx2			
Parpbp			
Pask			
Pbk			
Pclaf			
Pcna			
Phf19			
Pif1			
Pimreg			
Pkmyt1			
Pla2g4c			
Plk1			
Plk4			
Pmf1			
Pola1			
Pola2			
Pold1			
Pold2			
Pold3			
Pole			
Pole2			
Polh			
Polq			
Prc1			
Prim1			
Prim2			
Prr11			
Psmc3ip			
Racgap1			
Rad18			

Rad21			
Rad50			
Rad51			
Rad51ap1			
Rad51b			
Rad54b			
Rad54l			
Rangap1			
Rbbp8			
Rbl1			
Rccd1			
Reep4			
Rfc1			
Rfc2			
Rfc3			
Rfc4			
Rfc5			
Rfwd3			
Rif1			
Rmi2			
Rnaseh2c			
Rnf168			
Rpa2			
Rpa3			
Rrm1			
Rrm2			
Rtkn2			
Sapcd2			
Sass6			
Scml2			
Selenoh			
Serpinb8			
Sgo1			
Sgo2a			
Shcbp1			
Siva1			
Ska1			
Ska2			
Ska3			
Skp2			
Slbp			
Slc30a10			
Slc43a3			
Slc9a5			
Slf1			
Slfn9			
Smc2			
Smc4			
Snrnp25			

Spag5			
Spc24			
Spc25			
Spdl1			
Stbd1			
Stil			
Stmn1			
Suv39h1			
Tacc3			
Tagln2			
Tbc1d31			
Tcf19			
Tedc1			
Terf1			
Tex30			
Tfdp1			
Ticrr			
Timeless			
Tipin			
Tk1			
Tmpo			
Tnfaip8l1			
Top2a			
Topbp1			
Tpx2			
Traip			
Trim59			
Trip13			
Troap			
Ttk			
Tuba1c			
Tubb4b			
Tubb6			
Tube1			
Tubg1			
Tyms			
Ube2c			
Ube2s			
Ube2t			
Uevld			
Uhrf1			
Ulbp1			
Ung			
Usp1			
Usp37			
Vrk1			
Wdhd1			
Wdr76			
Wee1			

Xkr5			
Xndc1			
Zfand4			
Zfp367			
Zfp993			
Zgrf1			
Zranb3			
Zwilch			

MP5	MP6	MP7
1110008P14Rik	1700016K05Rik	Acaca
2310009B15Rik	1700025G04Rik	Acacb
Abracl	2610035D17Rik	Aph1c
Ak6	4930517O19Rik	Bri3
Akr1a1	4930554G24Rik	Chpt1
Akr1b3	Adam12	Cited1
Anp32b	Adamts5	Cox17
Anp32e	Adamts6	Cox8b
Anxa2	Adgrl3	Cryab
Ap2m1	Aff3	Cst6
Ap2s1	Agap1	Cyba
Apex1	Akap12	Cystm1
Aprt	Arap2	Dct
Arf1	Asap1	Eif3f
Arhgdib	Atrnl1	Fabp3
Arpc3	B4galt6	Fabp5
Arpp19	Cd200	Fam104a
Asna1	Cd9	Foxp2
Atp5c1	Cdh10	Fundc2
Atp5d	Cdk5rap2	Gm3776
Atp5f1	Chl1	Gng8
Atp5g1	Col23a1	Gsk3b
Atp5h	Csad	Gsta1
Atp5j	Ctsh	Gsta2
Atp5k	Cttnbp2	Gstp1
Atp5o	Dkk3	Mlana
Atp6v0e	Dock3	Mtss1
Atpif1	Eno3	Myo5a
Aurkaip1	Erbb3	Ndufs2
Bag1	Etv1	Oat
Banf1	Fam184b	Oca2
Bax	Fap	Pmel
Bex3	Fbxl7	Ptgds
Bola2	Fxyd1	Ptprs
Btf3	Gjc3	Ralgapa2
Bud31	Gm15594	Reep5
Bzw1	Gm49267	Rgs10
C1qbp	Gpm6b	Rhoa
Cacybp	Gulp1	Rnasek
Ccdc124	Hecw2	Rnf7
Cct3	Hpgds	S100a1
Cct5	Ikbkb	S100b
Cct6a	Il16	Sec11c
Cct8	Inpp5f	Selenos
Cdk2ap1	Iqgap2	Sgcd
Cdk4	Itga2	Slc37a2

Cenpx	Klf12	Smpd1
Cetn3	Lgi4	Traf5
Chchd1	Lima1	Tspan10
Chchd4	Lmo4	Tyrp1
Chchd7	Map4k3	Uqcrfs1
Chmp2a	Mbp	Vegfb
Churc1	Mecom	Vps29
Ciao2b	Mef2c	
Cisd1	Megf9	
Clic1	Metrn	
Cnbp	Mmd	
Cnih4	Mprip	
Coa3	Mpzl1	
Commd1	Mtss1	
Cope	Mxra8	
Cops6	Myzap	
Cops9	Ndrg2	
Coq7	Nrn1	
Cox20	Ntn4	
Cox5a	P3h2	
Cox5b	Pde1c	
Cox6a1	Plat	
Cox7b	Plpp1	
Creld2	Ppm1l	
Cryab	Prickle2	
Cstb	Prkca	
Cuedc2	Prss23	
Cyc1	Psd3	
Cycs	Ptprm	
Dctn3	Rasal2	
Dctpp1	Rasgrp3	
Ddt	Rbfox2	
Ddx21	Rbm20	
Ddx39	Rnf152	
Denr	Sema3d	
Dynll1	Serpinb1a	
Ebna1bp2	Sgcd	
Eef1d	Slc12a2	
Eef1e1	Slc4a8	
Eif1ad	Snx25	
Eif2s1	Sort1	
Eif2s2	Sox5	
Eif3b	Sox5os4	
Eif3c	Sox6	
Eif3g	Stard13	
Eif3i	Tcf7l1	
Eif3j1	Tgfb2	
Eif4a1	Tnik	
Eif4e2	Tom1l2	

Eif4g2	Unc5c	
Eif5a	Zbtb7c	
Eif6	Zfhx4	
Elob	Zfp608	
Elof1	Zfp704	
Emc6		
Emg1		
Eno1		
Erh		
Esd		
Etfb		
Fabp5		
Fam162a		
Fbl		
Fkbp11		
Fkbp1a		
Fkbp3		
Fkbp4		
G3bp1		
Gadd45gip1		
Galk1		
Gapdh		
Gemin6		
Glrx3		
Gm2000		
Gnai2		
Gnb2		
Gnl3		
Gpx1		
Gspt1		
Gtf2h5		
Higd1a		
Hint1		
Hmgn1		
Hnrnpa3		
Hnrnpab		
Hnrnpd		
Hnrnpf		
Hras		
Hsp90aa1		
Hspa5		
Hspa8		
Hspd1		
Hspe1		
Idh2		
Idh3a		
Ier3ip1		
Ifitm2		
Impdh2		

Jpt1		
Kmt5a		
Lamtor1		
Lamtor4		
Lamtor5		
Ldha		
Llph		
Lrrc59		
Lsm12		
Lsm2		
Lsm4		
Lyar		
Magoh		
Mak16		
Manf		
Mbd3		
Mdh1		
Metap2		
Micos10		
Micos13		
Mien1		
Morf4l1		
Mpc2		
Mrpl12		
Mrpl13		
Mrpl14		
Mrpl17		
Mrpl18		
Mrpl20		
Mrpl21		
Mrpl23		
Mrpl27		
Mrpl28		
Mrpl30		
Mrpl34		
Mrpl35		
Mrpl36		
Mrpl52		
Mrpl53		
Mrpl54		
Mrpl57		
Mrpl58		
Mrps14		
Mrps16		
Mrps21		
Mrps24		
Mrps36		
Mrps7		
Mrto4		

Mvb12a		
Mybbp1a		
Mydgf		
Myl12a		
Myl6		
Naa38		
Nap1l1		
Ncl		
Ndufa10		
Ndufa11		
Ndufa12		
Ndufa3		
Ndufa5		
Ndufa8		
Ndufab1		
Ndufb2		
Ndufb3		
Ndufb6		
Ndufb7		
Ndufb8		
Ndufs3		
Ndufs5		
Ndufs6		
Ndufs7		
Ndufs8		
Ndufv2		
Ndufv3		
Nhp2		
Nifk		
Nme1		
Nol7		
Nolc1		
Nop10		
Nop56		
Nop58		
Npm3		
Nsa2		
Nudc		
Nudcd2		
Oaz1		
Pa2g4		
Pabpc1		
Park7		
Pcbp1		
Pdap1		
Pdcd5		
Pebp1		
Pet100		
Pfdn2		

Pfdn6		
Pfn1		
Pgam1		
Pgk1		
Pgls		
Phb2		
Phf5a		
Pin1		
Pkm		
Pole3		
Polr1d		
Polr2e		
Polr2f		
Polr2g		
Polr2j		
Polr2k		
Polr2l		
Pomp		
Pop5		
Pop7		
Ppa1		
Ppdpf		
Ppp1ca		
Ppp1r14b		
Prdx6		
Prelid1		
Prelid3b		
Prkar1a		
Prmt1		
Psenen		
Psma2		
Psma3		
Psma4		
Psma5		
Psma6		
Psma7		
Psmb1		
Psmb2		
Psmb3		
Psmb4		
Psmb5		
Psmb6		
Psmc2		
Psmc3		
Psmc4		
Psmc5		
Psmd12		
Psmd6		
Psmd7		

Psmd8		
Psmg4		
Ptges3		
Rab5if		
Rad23a		
Ran		
Ranbp1		
Rbis		
Rbm8a		
Rer1		
Rhoa		
Rhoc		
Rpl12		
Rpl23a		
Rpl31		
Rps17		
Rps19bp1		
Rps25		
Rps26		
Rsl1d1		
Ruvbl1		
Rwdd1		
S100a10		
Sap18		
Sdhb		
Sdhd		
Serbp1		
Set		
Sf3b5		
Sf3b6		
Sh3bgrl3		
Skp1a		
Slc25a39		
Slc25a5		
Slirp		
Smarca5		
Snrnp27		
Snrpb		
Snrpc		
Snrpd1		
Snrpd2		
Snrpd3		
Snrpf		
Snrpg		
Snu13		
Snx3		
Sparc		
Spcs1		
Sra1		

Srm		
Srp19		
Srsf3		
Ssb		
Ssr4		
Strap		
Sub1		
Suclg1		
Sumo2		
Svbp		
Swi5		
Taf10		
Taldo1		
Tbcb		
Timm10		
Timm10b		
Timm13		
Timm23		
Timm8a1		
Tmed9		
Tmem126a		
Tmem14c		
Tmem208		
Tmem258		
Tomm22		
Tomm5		
Tpi1		
Tpm3		
Tpm4		
Trappc2l		
Trir		
Trmt112		
Tspo		
Txn2		
Txndc17		
Txnl1		
Txnl4a		
U2af1		
Ube2m		
Ufc1		
Uqcc2		
Uqcr10		
Uqcrb		
Vdac1		
Vdac2		
Vdac3		
Wdr83os		
Xbp1		
Ybx3		

Ywhab		
Ywhaq		
Ywhaz		
Zc3h15		
Zmat2		
Znhit1		

Table S6: Patient T cell, BR1 and BR3 genes signatures

Wischnewski_2023 (BrM pTRT CD8)	VanderLeun_2020	Caushi_2021	Lowery_2022	Hanada_2022	Oliviera_2021
CXCL13	CXCL13	ZNF683	ATP10D	ENTPD1	KRT86
RGS1	ENTPD1	GEM	GZMB	CXCL13	RDH10
CCL4L2	ITGAE	TOX2	ENTPD1	HMOX1	TYMS
GZMB	PDCD1	BATF	KIR2DL4	PDCD1	HMOX1
DUSP4	HAVCR2	GBP5	LAYN	LAYN	GNG4
IFNG	LAG3	MIR4435-2HG	HTRA1	CD27	CXCL13
TRBV28	TNFRSF18	TNS3	CD70	HAVCR2	AFAP1L2
GAPDH	TNFRSF9	GNA15	CXCR6	TNFRSF9	ACP5
CTLA4		CXCL13	HMOX1	MIR155HG	MYO1E
CCL3		RBPJ	ADGRG1	BATF	LAYN
LAG3		ENTPD1	LRRN3	TIGIT	TNS3
CD7		LINC02195	ACP5	AD000671.2	TNFSF4
TIGIT		GPR25	CTSW	GZMH	AKAP5
CCL4		ITGAE	GALNT2	CD70	HAVCR2
ITGAE		GNLY	LINC01480	TMEM121	ENTPD1
		PDCD1	CARS	LRRN3	SLC2A8
		CTLA4	LAG3	NHS	AC243829.4
		PRDM1	TOX	TTN	ZBED2
		TNFRSF9	PTPRCAP	LINC01281	MCM5
		TIGIT	ASB2	ASB2	CAV1
		HAVCR2	ITGB7	SIRPG	GOLIM4
			PTMS	ANKS1B	TRAV21
			CD8A		VCAM1
			GPR68		PON2
			NSMCE1		MTSS1
			ABI3		CD38
			SLC1A4		TRBV11-2
			PLEKHF1		MS4A6A
			CD8B		TOX2
			LINC01871		CSF1
			CCL4		GALNT2
			NKG7		FXYD2
			CLIC3		PLPP1
			NDFIP2		LMCD1
			PLPP1		MYL6B
			PCED1B		LAG3
			CXCL13		HLA-DRA
			PDCD1		IGFLR1

			PRF1		CCDC50
			HLA-DMA		CD27
					KIAA1324
					CDKN2A
					CD70
					ABHD6
					CTLA4
					PDCD1
					GEM
					NUSAP1
					TOX
					CXCR6
					NMB
					HOPX
					CLIC3
					INPP5F
					SNAP47
					TSHZ2
					HLA-DMA
					SIT1
					HLA-DRB1
					TUBB
					PYCARD
					ADGRG1
					HLA-DQA1
					PRF1
					HLA-DPA1
					PTMS
					CKS1B
					HIPK2
					CHST12
					LSP1
					FAM3C
					SLC1A4
					NUDT1
					DNPH1

MP4	MP6	BR1 pro-inflammatory	T_CD8	BR1 chemokine L-R	BR3 Neuro
AIDA	C1orf21	HLA-DRB5	CD8A	CCL3	SEMA3A
ANKRD34A	ADAM12	HLA-DQA1	CD8B	CCL4	SEMA6A
APOL6	ADAMTS5	CD74	CD3E	CCL5	
APOL1	ADAMTS6	TAP1		CCR5	
APOL2	ADGRL3	HLA-DQB2		CXCR6	
APOL1	AFF3	HLA-DQB1		CXCR3	
APOL2	AGAP1	HLA-E		CXCL16	
ATP8B4	AGAP11	B2M		CXCL9	
AXL	AGAP5	ISG15			
B2M	AGAP7P	IFIT3			
BATF2	AGAP9	IFIT2			
BST2	AKAP12	IFI35			
C1R	ARAP2	IFI27L2			
CASP12	ASAP1	SPP1			
CCL13	ATRNL1	S100A6			
CCL2	B4GALT6	S100A4			
CFAP100	CD200	ITGAX			
CFB	CD9	LGALS1			
CLEC2D	CDH10	LGALS3			
CMPK2	CDK5RAP2	CD86			
CSF1	CHL1	CD28			
CSTA	COL23A1	ICAM1			
CXCL10	CSAD	CD74			
CXCL9	CTSH	MIF			
DDX60	CTTNBP2	LGALS9			
DHX58	DKK3				
DTX3L	DOCK3				
EIF2AK2	ENO3				
FLACC1	ERBB3				
GBP6	ETV1				
GBP1	FAM184B				
GBP2	FAP				
GBP4	FBXL7				
GBP7	FXYD1				
GBP6	GJC3				
GBP5	GPM6B				
GBP6	GULP1				
GBP7	HECW2				

GBP6	HPGDS				
GBP6	IKBKB				
GPR149	IL16				
GPR65	INPP5F				
GVINP1	IQGAP2				
HLA-A	ITGA2				
HLA-B	KLF12				
HLA-C	LGI4				
HLA-E	LIMA1				
HLA-F	LMO4				
HLA-G	MAP4K3				
HLA-H	MBP				
HLA-A	MECOM				
HLA-B	MEF2C				
HLA-C	MEGF9				
HLA-E	METRN				
HLA-F	MMD				
HLA-G	MPRIP				
HLA-A	MPZL1				
HLA-B	MTSS1				
HLA-C	MXRA8				
HLA-E	GCOM1				
HLA-F	MYZAP				
HLA-G	POLR2M				
HLA-A	NDRG2				
HLA-B	NRN1				
HLA-C	NTN4				
HLA-E	P3H2				
HLA-B	PDE1C				
HLA-C	PLAT				
HLA-E	PLPP1				
HLA-F	PPM1L				
HLA-G	PRICKLE2				
HLA-E	PRKCA				
HERC6	PRSS23				
IFI16	PSD3				
IFI16	PTPRM				
MNDA	RASAL2				
PYHIN1	RASGRP3				
IFI16	RBFOX2				
MNDA	RBM20				
PYHIN1	RNF152				
IFI16	SEMA3D				

IFI16	SERPINB1				
IFI16	SGCD				
MNDA	SLC12A2				
PYHIN1	SLC4A8				
IFI27	SNX25				
IFI27L1	SORT1				
IFI27L2	SOX5				
IFI35	SOX6				
IFI44	STARD13				
IFIH1	TCF7L1				
IFIT1	TGFB2				
IFIT1B	TNIK				
IFIT2	TOM1L2				
IFIT3	UNC5C				
IFIT3	ZBTB7C				
IFITM3	ZFHX4				
IRGM	ZNF608				
IRF1	ZNF704				
IRF7	Zfp704				
IRGM					
IRGM					
ISG15					
ISG20					
KY					
LGALS9					
LGALS9B					
LGALS9C					
LRFN1					
LY6E					
MAP3K19					
MLKL					
IFI16					
NLRC5					
NMI					
OAS1					
OAS1					
OAS2					
OAS3					
OASL					
OASL2P					
PARP10					
PARP11					
PARP12					

PARP14					
PARP9					
PHF11					
PHF11					
PHF11					
PML					
PSMB10					
PSMB8					
PSMB9					
PSME1					
PSME2					
RNF19B					
RNF213					
RSAD2					
RTP4					
SAMD9L					
SAMHD1					
SLC2A6					
SLFN11					
SLFN13					
SLFN11					
SLFN13					
SOCS1					
SP100					
SP110					
SP140					
SP140L					
STAT1					
STAT2					
STYK1					
TAP1					
TAP2					
TAPBP					
TAPBPL					
TNFSF10					
TOR3A					
TRAFD1					
TRIM5					
TRIM5					
TRIM21					
TRIM25					
TRIM5					
TRIM34					

TRIM6-TRIM34					
UBE2L6					
USP18					
USP41P					
WNT2B					
XAF1					
XDH					
YPEL4					
ZBP1					
ZNFX1					